Lodz University of Technology
Faculty of Electrical, Electronic, Computer and Control Engineering
DEPARTMENT OF MICROELECTRONICS AND COMPUTER SCIENCE

Doctor of Philosophy Dissertation

A Wall Current Transformer for Beam Intensity Measurements in the Large Hadron Collider

Michal Krupa

Dissertation written under supervision of:
Dr Marek Gasior, CERN, Geneva, Switzerland
Dr Wojciech Cichalewski, Lodz University of Technology, Lodz, Poland

Lodz, 2022

Politechnika Łódzka
Wydział Elektrotechniki, Elektroniki, Automatyki i Informatyki
KATEDRA MIKROELEKTRONIKI I TECHNIK INFORMATYCZNYCH

Rozprawa Doktorska

Transformator prądu obrazu do pomiaru intensywności wiązek Wielkiego Zderzacza Hadronów

Michał Krupa

Promotor przewodu doktorskiego:
dr inż. Marek Gąsior, CERN, Genewa, Szwajcaria

Promotor pomocniczy:
dr inż. Wojciech Cichalewski, Politechnika Łódzka

Łódź, 2022

“We are stuck with technology when what we really want is just stuff that works.”

Douglas Adams, *The Salmon of Doubt*

Pracę tę dedykuję moim Rodzicom.

Abstract

The Large Hadron Collider (LHC) collides two counter-rotating particle beams to recreate conditions that existed in the first moments after the universe began. Rather than forming a continuous stream, the beam particles are grouped into distinct nanosecond-long bunches. A suite of sophisticated instrumentation allows researchers to monitor the beam to assure an efficient and safe operation of the accelerator. One of the most fundamental measurements is quantifying the number of particles contained within each bunch, referred to as the bunch intensity.

Charged particles of bunches travelling in an accelerator constitute an electric current, the integral of which is proportional to the bunch intensity. During the first years of the LHC operation four Fast Beam Current Transformers (FBCTs) coupling to the beam current served as the primary bunch intensity monitors. However, their undesired sensitivity to the transverse beam position and their excessively long output pulses deteriorated the accuracy of the LHC bunch intensity measurements. This dissertation reports in detail on the author's research and development work on a new electromagnetic sensor overcoming the FBCT limitations.

The Wall Current Transformer (WCT) consists of eight small magnetic cores which are evenly distributed azimuthally around a dielectric insert embedded into the accelerator's vacuum chamber. A conductive screw traversing each core's centre carries a part of the wall current, equal but opposite to the beam current, which induces signals in wires wound ten times around the cores. Such an arrangement is equivalent to eight parallel 1:10 current transformers sensing the whole wall current. Thus, the sum of the secondary-side signals is proportional to the instantaneous bunch current and upon integrating and rescaling results in the bunch intensity. To control its measurement bandwidth, the monitor features large ferrite cores and an RF bypass. A set of analogue front-end electronics adapts the WCT output signals to the used acquisition systems. The WCT's mechanical design enables its assembly around a closed vacuum chamber. The monitor is also fully compatible with the existing infrastructure at the original FBCT location.

Prior to any particle beam measurements, the WCT's performance was quantified through extensive laboratory tests. The newly developed sensor demonstrated an excellent output pulse quality, adequate signal levels, sufficiently wide bandwidth, and a negligible longitudinal beam-coupling impedance. Such promising results motivated an installation of one WCT in the LHC to compare it with the FBCT as well as other sensors capable of measuring the bunch intensity. Besides a superior output pulse quality, the WCT was also the only tested monitor not showing any measurable sensitivity to the transverse beam position. Over the following years, additional WCTs replaced the remaining FBCTs and became the main LHC bunch intensity monitors.

Although the WCT was optimised for the LHC bunches, it can find application in other facilities as well. Notably, it has already replaced another sensor in the second-largest CERN accelerator. Beyond bunch intensity monitoring, the WCT's ability of measuring the transverse beam position and the longitudinal bunch shape remains to be quantified through further studies.

Keywords: bunch intensity measurements; beam current measurements; Large Hadron Collider beam instrumentation

Streszczenie

Zderzenia dwóch wiązek cząstek w Wielkim Zderzaczu Hadronów (ang. *Large Hadron Collider*, LHC) pozwalają na odtworzenie warunków panujących w pierwszych chwilach istnienia Wszechświata. Cząstki w owych wiązkach są zgrupowane w nanosekundowych paczkach (ang. *bunch*). Zaawansowane systemy instrumentacji pozwalają na monitorowanie właściwości wiązki, aby zagwarantować wydajną i bezpieczną pracę akceleratora. Jednym z najważniejszych mierzonych parametrów jest natężenie paczki definiowane jako liczba cząstek w niej zawartych.

Ruch paczek naładowanych cząstek prowadzi do powstania prądu elektrycznego, którego całka jest proporcjonalna do natężenia paczki (ang. *bunch intensity*). W pierwszych latach funkcjonowania LHC głównym czujnikiem natężenia paczek były cztery szybkie transformatory prądu wiązki (ang. *Fast Beam Current Transformer*, FBCT), których wskazania obarczone były błędem zależnym od poprzecznej pozycji wiązki. Do dalszego ograniczenia dokładności pomiarów przyczyniał się również zbyt długi sygnał wyjściowy FBCT. Niniejsza dysertacja opisuje przeprowadzone przez autora prace badawcze nad nowym sensorem eliminującym wady FBCT.

Transformator prądu obrazu (ang. *Wall Current Transformer*, WCT) zawiera osiem niewielkich rdzeni magnetycznych rozmieszczonych dookoła dielektrycznego segmentu zespolonego z komorą próżniową akceleratora. Metalowa śruba przechodząca przez środek każdego rdzenia przewodzi część prądu obrazu – równego co do wartości, lecz o przeciwnym znaku do prądu wiązki – który drogą indukcji magnetycznej generuje sygnały na przewodach owiniętych dziesięciokrotnie wokół rdzeni. Taka konfiguracja jest równoważna ośmiu równoległym transformatorom prądu o przełożeniu 1:10 mierzącym całkowity chwilowy prąd obrazu. Suma sygnałów po stronach wtórych jest zatem, po scałkowaniu i przeskalowaniu, równa natężeniu paczki. WCT zawiera również duże rdzenie ferytowe oraz bocznik wysokoczęstotliwościowy, które umożliwiają kontrolę pasma przepustowego sensora. Z kolei mechaniczna konstrukcja WCT pozwala na jego montaż dookoła zamkniętej komory próżniowej w pierwotnej lokalizacji FBCT.

Podczas szczegółowych pomiarów laboratoryjnych, służących ocenie osiągów sensora, WCT zademonstrowało wyśmienitą jakość impulsu wyjściowego, odpowiednie poziomy generowanych sygnałów, wystarczająco szerokie pasmo przepustowe oraz pomijalnie małą impedancję wzdłużną. Tak obiecujące wyniki doprowadziły do instalacji jednego WCT w LHC w celu porównania go do FBCT oraz innych sensorów mierzących natężenie paczki. WCT cechowało się nie tylko lepszą jakością sygnału wyjściowego, ale też było jedynym z przetestowanych sensorów, który nie wykazał żadnej zależności od poprzecznej pozycji wiązki. W następnych latach kolejne WCT zastąpiły pozostałe FBCT i stały się głównymi monitorami natężenia wiązki w LHC.

Zaprojektowane WCT zostało zoptymalizowane pod kątem LHC, niemniej jednak sensor ten może znaleźć również dalsze zastosowania. Dowodem tego jest jego instalacja także w drugim największym akceleratorze w CERN. Poza natężeniem paczki, WCT może potencjalnie służyć do obserwacji innych jej parametrów takich, jak poprzeczna pozycja czy wzdłużny kształt. Analiza ilościowa tych zdolności pozostaje tematem ewentualnych przyszłych badań.

Słowa kluczowe: pomiar natężenia paczki cząstek; pomiar prądu wiązki cząstek; instrumentacja wiązki cząstek w Wielkim Zderzaczu Hadronów

Acknowledgments

The work described in this thesis is a result of collaboration between the Department of Microelectronics and Computer Science of the Lodz University of Technology and the Beam Instrumentation Group of CERN. I am extremely grateful to both institutions for allowing me to pursue my scientific curiosity in a very professional and thought-provoking environment.

First and foremost I want to express my sincere gratitude to Prof. Andrzej Napieralski who advised me at the Lodz University of Technology throughout my Bachelor's, Master's and finally Doctoral Programme. His vast scientific and academic experience was invaluable to overcome many obstacles I faced during my endeavours. My work at CERN would not have been possible had it not been for Prof. Napieralski's outstanding commitment to aid students. I would also like to extend my deep gratitude to Dr. Wojciech Cichalewski of Lodz University of Technology whose support was indispensable for submitting this thesis.

Secondly, I want to thank Dr. Marek Gasior of CERN who originally proposed developing the Wall Current Transformer to measure bunch intensity in the Large Hadron Collider. I want to thank him for the extensive support and guidance he provided as my supervisor at CERN. Marek's willingness and patience to discuss the questions and issues that arose during the last years and his honest dedication to ensure that the development went ahead were what made my work and studies not only scholarly gratifying but also a truly enjoyable time.

I would also like to thank all the colleagues who helped me in various ways during the last years. Without them the work documented in this thesis would not have happened.

During commissioning of the monitor with beam Stephan Bart Pedersen and David Belohrad worked hard to assure proper functioning of the analogue acquisition system and Jiri Kral provided very useful data from the digital acquisition system. Stefano Mazzoni and Marcus Palm made the data from the Longitudinal Density Monitor available to me. Jeroen Belleman, Thibaut Lefevre, Patrick Odier and Lars Soby were always ready to provide advice and share their experience. I would also like to thank all other members of the QP, BP, PI and IQ sections of CERN Beam Instrumentation Group for sharing their professional environment with me as well as the members of CERN Operations Group who always go the extra mile to fulfil our request during the Machine Development periods.

Great thanks go to my fellow students and dear friends Silvia Aguilera, Michael Betz, Andrea Boccardi, Miguel Fernandes, Kacper Lasocha, Tom Levens, Jakub Olexa, Apostolos Sounas, and Jack Towler for many casual yet fruitful discussions as well as the many coffees we had together in CERN's R3 which kept me happy and sane through the last years.

Dziękuję również Agnieszce, której wsparcie i codzienna motywacja w niezaprzeczalny sposób przyczyniły się do ukończenia tekstu tej dysertacji.

Na koniec, pragnę podziękować moim Rodzicom, którym niniejsza praca jest zadedykowana. Dziękuję Wam za nieustające wsparcie podczas wszystkich lat mojej edukacji, za pomoc w spełnianiu moich celów i marzeń, oraz za zaszczepienie we mnie miłości do nauki i technologi. Ta rozprawa nigdy nie powstałaby bez Waszej pomocy.

Contents

List of Figures

List of Tables

Glossary

ACCT AC Current Transformer.
ADC Analogue-to-Digial Converter.

BCT Beam Current Transformer.
BI Beam Instrumentation.
BLM Beam Loss Monitor.
BPM Beam Position Monitor.
BPTX Beam Pickup for Timing the Experiments.
BQM Beam Quality Monitor.
BSRT Beam Synchrotron Radiation Telescope.

DCCT DC Current Transformer.

FBCT Fast Beam Current Transformer.
FWHM Full Width at Half Maximum.

HEP High Energy Physics.

ICT Integrating Current Transformer.

LDM Longitudinal Density Monitor.
LHC Large Hadron Collider.

PCB Printed Circuit Board.

RF Radio Frequency.
RIS Random Interleaved Sampling.
RMS Root Mean Square.

SNR Signal-to-Noise Ratio.
SPS Super Proton Synchrotron.

UHV Ultra-High Vacuum.
UTC Coordinated Universal Time.

VNA Vector Network Analyser.

WCM Wall Current Monitor.
WCT Wall Current Transformer.

Chapter 1

Introduction

The chapter provides a basic overview of the principle of operation of a modern scientific accelerator. The domains of beam instrumentation and diagnostics are formally defined and basic methods for measurements of beam parameters are introduced. Subsequently, a brief overview of CERN, the European Organization for Nuclear Research, and its accelerator complex is presented. Finally, a more detailed description is given for CERN's flagship accelerator - the Large Hadron Collider.

1.1 Particle accelerators

Over the last eight decades particle accelerators have evolved from centimetre-size experimental apparatus to industrial tools used in applications ranging from ion implantation in semiconductors to oncology. It is estimated that more than 24 thousand industrial and medical accelerators were being used worldwide in 2012 [1]. Nevertheless, they also remain sophisticated instruments with which scientists probe the laws of nature through High Energy Physics (HEP).

The collection of charged particles travelling in an accelerator is referred to as a beam. HEP beams are ultrarelativistic i.e. travelling approximately at the speed of light. During acceleration, their velocity gain can be only minuscule. It is the beam energy, momentum, and power that increase substantially instead.

An interaction of two particles results in either a particle loss due to a high-energy collision or a change of the particles' direction of motion. Minimising the probability of beam particles colliding with the environment requires substantial effort. In particular, HEP accelerators maintain an Ultra-High Vacuum (UHV) environment with pressure below 1×10^{-9} mbar in all volumes where the beam travels, typically referred to as the vacuum chambers or the beam pipe.

Most accelerators come in one of the two shapes: linear (also called linacs) or circular[1]. Linacs accelerate the beam in a single pass along a straight line. In circular accelerators the particles follow a curved closed trajectory and their energy gradually increases every time they complete the path. The time it takes a beam to travel around a circular accelerator is commonly referred to as the revolution period with its reciprocal being the revolution frequency.

Motion of an electrically charged particle can be altered through an electric field $\vec{E}$ or a magnetic field $\vec{B}$. The force these fields exert on a particle with a charge q and a velocity $\vec{v}$ is called the Lorentz force $\vec{F}_{\mathrm{L}}$ [2, p. 1-2]:

$$\vec{F}_{\mathrm{L}} = q \cdot \vec{E} + q \cdot \vec{v} \times \vec{B} \tag{1.1}$$

The force caused by an electric field is always parallel to the field. Conversely, the force

---

[1] In reality circular accelerators are not prefect circles but a series of straight and curved sections which result in a closed path.

created by a magnetic field is perpendicular to both the field and the particle's direction of motion. Hence, only the electric field can do work on a particle and contribute to a gain or loss of the charged particle's energy. The force created by a magnetic field, however, is amplified by a large v. Thus, a magnetic field is typically more applicable to affect the charged particle's direction of motion, i.e. its trajectory.

As a particle with a charge q gains energy, its momentum p increases. The bending radius ρ with which a magnetic field B deflects a particle is linked to its charge and momentum [3]:

$$B\rho = \frac{p}{q} \tag{1.2}$$

This relation imposes the predominant limit over the beam energy range for any circular accelerator with a set ρ. As the beam gains momentum through acceleration, the bending magnetic field must also increase. The maximum field generated by mass-produced bending magnets is currently fixed at around 10 T [4]. In order to reach higher beam energy, accelerators have grown in circumference, effectively increasing the bending radius ρ. Attaining high energy beams usually requires a chain of successively larger accelerators.

In low energy regimes, the particles can be accelerated using a moderate static electric field. However, due to the electrical breakdown limit of static fields, in order to achieve higher beam energies, techniques involving time-varying electric fields take precedence [5]. The frequency at which the field is applied is commonly referred to as Radio Frequency (RF) and RF cavities are the conventional equipment generating the field.

Colliders are a special class of accelerators in which one beam collides with another. The figure of merit for any collider is the luminosity $\mathscr{L}$. It is a measure of the average beam density in the collision point and is proportional to the number of particles colliding within some defined amount of time [6]. Formally, for a two-beam collider, the luminosity is defined as:

$$\mathscr{L} = \frac{N_1 N_2 f_{\mathrm{rev}}}{4\pi\sigma_{\mathrm{x}}\sigma_{\mathrm{y}}} \tag{1.3}$$

where N_1 and N_2 are the number of particles in the the respective beams, f_{rev} is the revolution frequency, and σ_{x} and σ_{y} are the width and height of the effective overlap region of the two beams in the transverse plane.

Since discoveries in particle physics are an outcome of a statistical analysis of a large number of particle interactions, the greater the luminosity, the higher the chances are of observing a rare phenomenon. This requires a large number of particles, crossing one another at a high rate in a very small region. Precise knowledge of the luminosity is extremely important to correctly interpret the collision outcomes, therefore great attention is paid to understanding and minimising the errors on measurements of the quantities used to calculate the luminosity.

As the two beams collide, the interacting particles vanish from the beam. Moreover, the overlap region of the two beams tends to grow over time [7]. As a consequence, the luminosity decreases during collisions and at a certain point it is more efficient to discard the beams and start collisions with a new set of particles. The rate of this decay is referred to as the luminosity lifetime and is an important parameter in modelling how to use an accelerator in the most efficient way. The long term performance of a collider is often expressed in terms of its integrated luminosity, typically over either one year or the accelerator lifetime.

1.2 Beam instrumentation and diagnostics

Ensuring optimal operation of an accelerator necessitates continuous monitoring of the beam and tuning its parameters. The most typical beam observables include its transverse position, the number of particles it is composed of, the particle density distributions in the transverse and longitudinal planes, and the rate at which particles are lost from the beam.

There are two closely related domains which deal with measurements of beam parameters: beam instrumentation and beam diagnostics. Formally, “instrumentation” refers to the design and construction of the instruments observing the beam, whilst “diagnostics” is the use of the data gathered by these instruments. A thorough overview of contemporary beam instrumentation and diagnostics techniques is available in [8].

Beam instruments can employ one of the two fundamental measurement methods:

- intercepting, in which a non-negligible part of the beam power is absorbed during the measurement;
- non-intercepting, in which the measurement process does not affect the beam power in a significant manner.

In modern HEP accelerators non-intercepting instruments are more desirable, whenever possible, due to the substantial beam power. Nevertheless, a large number of intercepting measurement methods exist for industrial and lower energy accelerators.

Most non-intercepting instruments are sensitive to either the electromagnetic field carried by the beam or to other forms of beam-generated radiation e.g. synchrotron radiation, both of which scale differently with varying beam energy. The electromagnetic field of an ultrarelativistic beam is proportional to its velocity, thus it does not strictly depend on the energy. Other forms of radiation, in general, are in some way correlated with the beam energy and some non-intercepting methods might be applicable only in particular accelerators or only over a certain beam energy range.

1.3 The CERN accelerator complex

CERN, the European Organization for Nuclear Research, is located at the outskirts of Geneva, Switzerland. It houses 11 active accelerators which provide beams to some 25 physics experiments and facilities. Accelerators at CERN, commonly referred to as machines, come in one of the two shapes: linear or circular. Figure 1.1 shows an overview of the complex as of 2018. Extensive details about CERN accelerators are available at the outreach website [9].

All protons used at CERN originate from a hydrogen bottle located in front of LINAC 2. The beam accelerates the energy of 50 MeV before being injected to the first circular machine in the chain, the Proton Synchrotron Booster (PSB) which further accelerates the particles to 1.4 GeV.

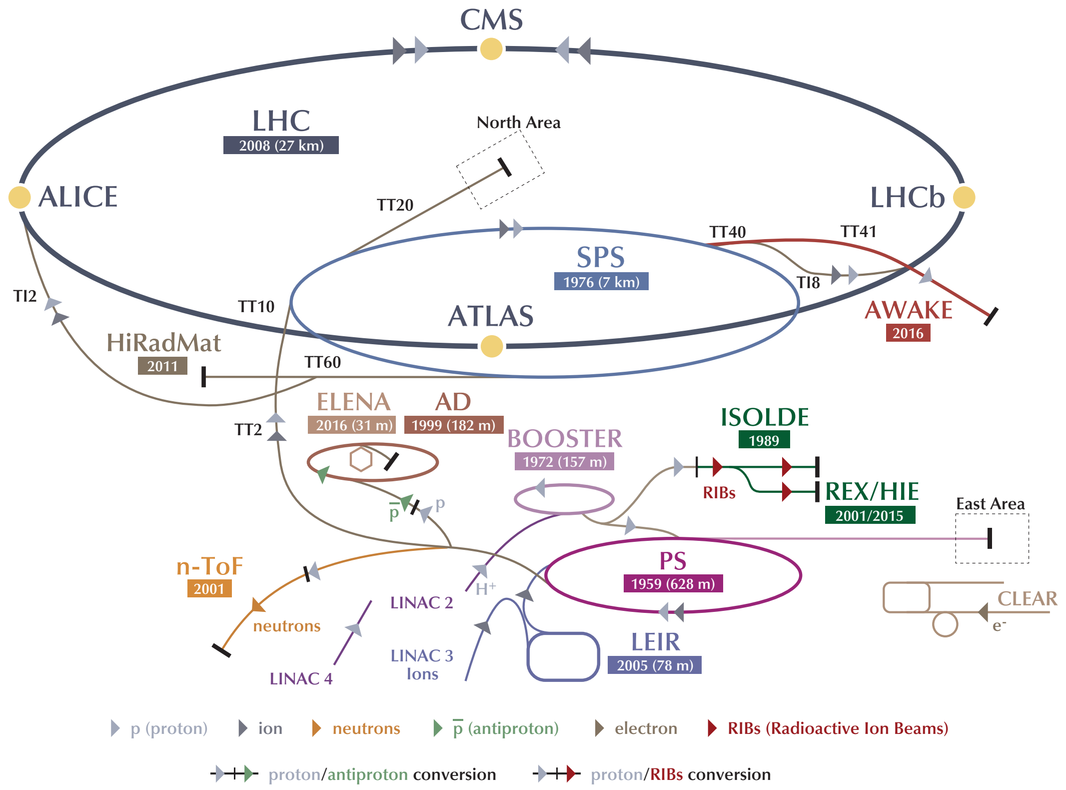

Figure 1.1: CERN accelerator complex. Adapted from [10].

The beam undergoes two more acceleration steps: 25 GeV in the Proton Synchrotron (PS), and 450 GeV in the Super Proton Synchrotron (SPS) before its injection into CERN's flagship accelerator, the Large Hadron Collider (LHC).

Not all of the protons leaving LINAC 2 end up in the LHC. Other facilities using proton beams at CERN include:

- The LINAC 4 accelerator being commissioned to replace the LINAC 2 in the near future;
- The ISOLDE and REX/HIE converting protons into low-energy beams of radioactive ions used for studies of nuclear reactions;
- The Antiproton Decelerator (AD) and Extra Low Energy Antiproton Ring (ELENA) decelerators studying the properties of antimatter at low energies;
- The East Area using the PS beams for irradiation tests and serving as a test zone for large experiments;
- The Neutron Time-Of-Flight (n-TOF) facility studying interaction between neutrons and nuclei over a wide range of energies;
- The HiRadMat performing irradiation studies of material samples, accelerator components and electronic modules;
- The North Area providing the SPS beams for a number of physic experiments;

- The Advanced Wakefield Experiment (AWAKE) facility for studies of novel acceleration techniques based on plasma-induced wakefields.

Protons are not the only particle species used at CERN. Heavy lead ions originate in LINAC 3 and are accelerated in the Low Energy Ion Ring (LEIR) before joining the accelerator chain in the PS. In the future, production of argon and xenon ions is also foreseen.

Some new additions to the CERN accelerator complex are the CERN Linear Electron Accelerator for Research (CLEAR) and AWAKE. They partially reuse the infrastructure developed for previous installations and currently are the only machines at CERN accelerating electrons.

1.4 The Large Hadron Collider

At twenty seven kilometres in circumference, CERN's LHC is the largest and highest-energy particle accelerator in the world and one of the largest scientific projects ever carried out. It collides two counter-rotating beams at the energy of 7 TeV per proton. A comprehensive overview of the LHC, its physics, and technological challenges is available in [11].

Following injection from the SPS at 450 GeV, the two beams travel in two physically separated rings. Once they reach the collision energy, their trajectories are intersected and the particles start colliding. By convention the LHC beams are referred to by numbers: "Beam 1" moves clockwise and "Beam 2" moves anticlockwise with the LHC viewed from above.

The LHC beams collide in four points where the two rings intersect each other in a common vacuum chamber. The collision points house experiments and are often referred to as Interaction Points (IPs). ATLAS and CMS are large general-purpose detectors used to study a wide range of physics phenomena. Physicists working at these two experiments jointly announced the discovery of the Higgs boson in 2013. ALICE specialises in heavy-ion collisions and studies of matter at extreme temperatures and densities. LHCb investigates the so-called beauty quark, shining light on the faint differences between the regular matter and antimatter.

The LHC layout consists of eight octants as shown in Fig. 1.2. Octants 1, 2, 5 and 8 accommodate the large experiments, respectively ATLAS, ALICE, CMS, and LHCb, with octants 2 and 8 also providing the injection lines for both rings. Octants 3 and 7 house protection equipment guaranteeing that the beams do not damage the accelerator. If the beams endanger the equipment or their quality limits an efficient LHC operation, they are safely removed from the machine in octant 6 through a process called beam dumping. Finally, octant 4 contains the accelerating Radio Frequency (RF) structures as well as a range of Beam Instrumentation (BI) equipment.

Magnetic field in excess of 8 T maintains a 7 TeV beam within the 27 km LHC rings. Presently, only superconducting electromagnets can generate a field with such magnitude and sufficient quality. The 1232 LHC bending magnets use a current of over 11 kA, operate at a temperature of 1.9 K, and store in total an immense 9 GJ of energy. Even a minuscule heat deposition into a magnet might lead to a quench, i.e. a sudden loss of superconductivity, and result in severe damage to the accelerator's components. Continuous monitoring of the LHC beams and the accelerator itself is essential for safe daily operation of the machine.

To minimise the probability of a collision between the beam and residual gas, the LHC vacuum chambers maintain pressure of 1×10^{-11} mbar, making it as empty as the interstellar space.

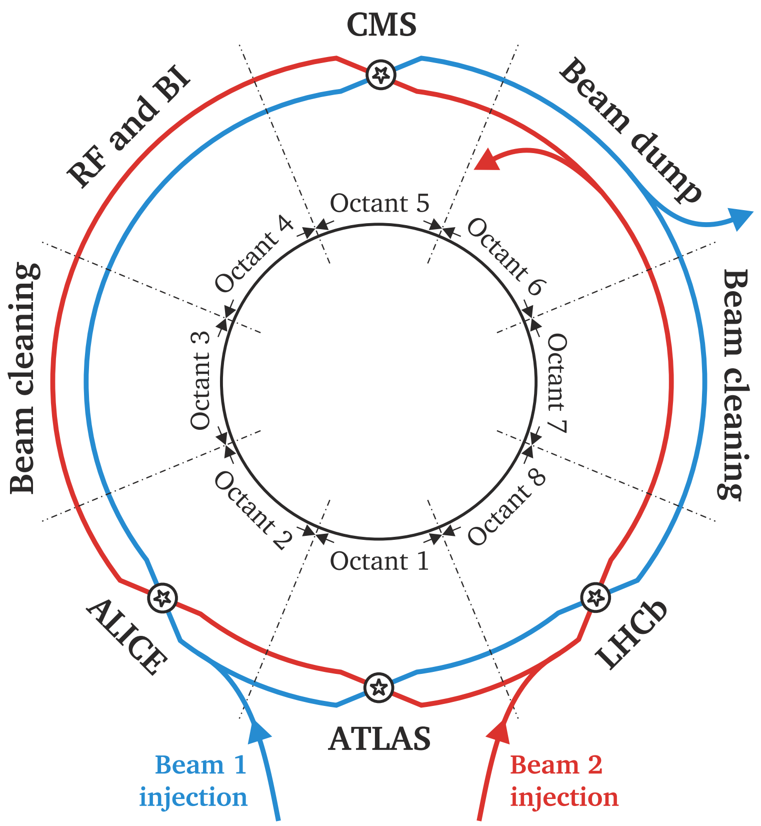

Figure 1.2: Layout of the LHC. Adapted from [12].

This is possible due to a sophisticated vacuum system. As the superconducting sections of the accelerator cool down, the residual gas condenses on the vacuum chamber walls by adsorption. On the other hand, the room-temperature sections of the LHC vacuum chambers are internally coated with a non-evaporable getter absorbing residual molecules when heated. Moreover, most non-cryogenic sections of the LHC regularly undergo a so-called bake-out in which the beam pipe is heated from outside up to approximately 300 °C to improved the vacuum quality.

The LHC superconducting magnets and its vacuum system operate at extremely low temperatures, just a few kelvins above the absolute zero. The LHC cryogenic system uses close to 130 tonnes of helium, 80 tonnes of which are in the superfluid state at 1.9 K, to cool down the accelerator making the LHC the largest cryogenic facility in the world. However, some regions of the machine operate at room temperature, in particular the straight sections joining the long strings of superconducting bending magnets.

A set of superconducting RF cavities operating at 400 MHz supply the electric field needed to accelerate the LHC beams. Each of the eight cavities installed per LHC ring can reach 2 MV yielding the maximum accelerating voltage of 16 MV. Moreover, the RF cavities and their control system play a critical role in defining and controlling the longitudinal beam structure.

Despite the state-of-the-art equipment and systems necessary to maintain and accelerate the beam in the LHC, a safe and efficient exploitation of the machine would not be possible without continuous monitoring of the beam. The diverse array of beam instrumentation installed in the LHC [13] gives the accelerator operators an insight into the beam parameters. These measurements are also extensively used by physicist who constantly develop improved modes of operation and tune the machine to reach its full potential.

More than 1000 Beam Position Monitors (BPMs) distributed around the LHC measure the transverse position of the beam within the vacuum chamber [14]. The BPMs serve as inputs to the beam orbit feedback system which continuously manipulates the LHC magnets to stabilise the beam around its design trajectory. The BPMs are also instrumental for studying the accelerator optics describing how magnets influence the particles' motion. To mitigate the risk of equipment damage due to the beam being too close to the vacuum chamber wall, the BPMs are also a part of the accelerator protection system.

Even more numerous than the BPMs are the Beam Loss Monitors (BLMs) with more than 4000 instruments installed in the LHC tunnel [15]. These devices monitor the rate and locations at which individual particles escape the vacuum chamber. The principle role of the BLMs is to provide input to the accelerator protection systems. When the detected beam loss exceeds a certain limit, the beam is safely removed from the accelerator to avoid any potential equipment damage. The BLM data also helps with improving the performance of the LHC by varying the accelerator parameters to minimise the beam loss.

Understanding how and why the transverse beam size changes during operation is essential to optimise the accelerator performance and maximise the luminosity. Due to the varying beam energy and the very high number of particles, precise beam size measurements in the LHC are difficult. The two main techniques used are measuring the synchrotron radiation produced when the beam trajectory is bent by a magnet and using a thin wire moving trough the beam at high speed [16]. Since the measurement accuracy of the beam size monitors contributes to the the absolute luminosity determination error, engineers and scientists invest a significant effort into cross-calibrating the monitors and analysing the data they provide.

The other observable critical for calculating the luminosity is the number of particles contained in the beam, normally referred to as beam intensity. The LHC features two types of intensity monitors - ones that measure the whole beam, and ones which measure the number of particles within a given time window [17]. These monitors, their various applications, and the intricacies of beam intensity measurements are discussed in detail in the following chapter.

Chapter 2

Beam intensity measurements

The chapter defines the terms related to beam and bunch intensity measurements used throughout this thesis. Several common beam intensity monitors are introduced with their main advantages and disadvantages compared. Next, the beam intensity monitoring systems deployed in the LHC are reviewed in detail with a particular focus on the motivation for developing a new bunch intensity monitor. The chapter concludes with the thesis statement.

2.1 Definitions

Beam intensity is defined as the number of particles making up a beam. It is one of the most fundamental yet crucial beam parameters for any type of accelerator. In particle colliders the beam intensity appears explicitly in the equation defining luminosity, a collider's figure of merit. In fact, as the LHC set its first beam intensity world record in 2011, Rolf Heuer – the CERN Director General at the time – said that "beam intensity is key to the success of the LHC" since "higher intensity means more data, and more data means greater discovery potential" [18].

Over the years many beam intensity measurements techniques have been developed and successfully applied in accelerators. They range from directly collecting the entire beam in a conductive cup, to using current transformers, to using extremely sensitive superconductive magnetometers [19]. Besides the varying sensitivity, some measurements technique are viable only for beams with a given temporal distribution of particles or with a given energy.

2.1.1 Beam temporal structure

One of the most basic characteristics of any particle beam is its longitudinal electric charge distribution. Besides the number of particles itself, this is probably the most crucial specification to consider when choosing or designing a beam intensity sensor. The following paragraphs formally define the terms commonly used to discuss the longitudinal beam composition.

DC beam

Possibly the simplest time structure for any beam is a continuous uniform flux of particles. Due to the lack of any modulation along the movement axis, such beams are often referred to as DC beams. Historically, they were used extensively in early accelerators but even nowadays they find industrial use when low beam energy is sufficient [20].

Such beams occasionally find application also in HEP for colliding particles with stationary targets [21]. However, they rarely appear in beam-beam colliders.

Bunched beam

In HEP, rather than forming a continuous stream, most beams consist of discrete packets of particles called bunches. The distribution of particles along the axis of motion gives a bunch its shape, often also called the longitudinal profile. Theoretical analyses typically consider bunches to follow the Gaussian distribution, with $\cos^2$-like functions being a close second. Real bunches, however, have more complex shapes [22]. Moreover, sometimes to optimise the accelerator performance, physicists deliberately modify the bunch shape to achieve a very specific profile [23].

To describe the evolution of the longitudinal bunch shape without depending on its formal mathematical description, a concept of bunch length becomes very helpful. Although its precise definition can vary between the accelerator laboratories, the bunch length is a generalised way to express that a given time period contains a given fraction of the total bunch intensity. For example, in the LHC the bunch length is defined as four standard deviation of a Gaussian function fitted over the measured longitudinal bunch profile [24]. Despite disregarding the accurate longitudinal bunch shape, this method is very robust for monitoring the accelerator operation.

A collection of bunches forms a train, also called a batch, with the interval between two consecutive bunches referred to as the bunch spacing. If the bunches making up a train are equidistant and they fill up the entire accelerator, they form a Continuous Wave (CW) beam. Both scientific and industrial accelerators use such beams to reach a high average beam power. The individual bunch parameters in a CW beam might vary a little from bunch to bunch, however, CW accelerators attempt to deliver beams as uniform as possible.

Even though CW beams present some attractive benefits, in many accelerators the beam structure is more intricate, especially when the beam must transfer between many accelerators in large HEP laboratories. To safely eject a high energy beam from a circular accelerator, extraction electromagnets require a time window without any particles present. In general, the higher the beam energy, the longer is the needed quiet interval. Four smaller machines pre-accelerate the proton bunches collided in the LHC, with each of them featuring its own required quiet time. The resulting structure, an example of which is shown in Fig. 2.1, can be rather complicated with bunches not occupying all of the available slots.

Some particles can escape their bunch due to accelerator imperfections. This phenomena is referred to as debunching and not only can it pose a significant risk to the machine but it might also compromise beam intensity measurements as some sensing methods are not sensitive to particles not contained within a bunch. Some accelerators feature two or more beam intensity monitors using different technologies with one capable of measuring the entire beam and other focusing only on individual bunches.

2.1.2 Beam and bunch current

By definition, a charged particle Q moving across space constitutes an electric current i equal to the rate of flow of electric charge through some reference region:

$$i = \frac{\mathrm{d}Q}{\mathrm{d}t} \tag{2.1}$$

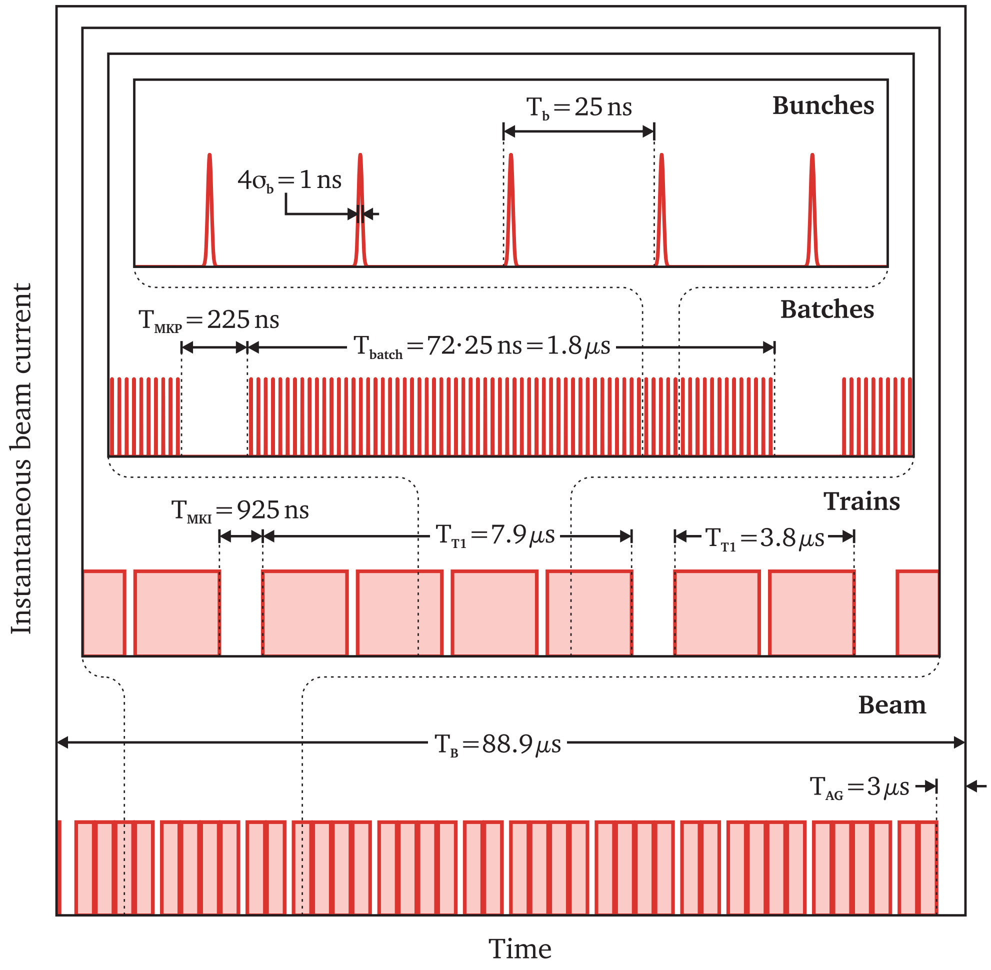

Figure 2.1: Example of a possible temporal structure of an LHC beam.

A beam made of N particles with a charge e_0 each, travelling in an accelerator of a length l with a speed v comprises a beam current i_B:

$$i_\mathrm{B} = N e_0 \frac{v}{l} \tag{2.2}$$

In circular accelerators the term l/v is the revolution period T_r, i.e. the interval a particle needs to complete a full circle around the accelerator. Hence, eq. 2.2 becomes:

$$i_\mathrm{B} = \frac{N e_0}{T_\mathrm{r}} \tag{2.3}$$

It is important to note that such a definition of beam current in entirely independent from the longitudinal distribution of charges within the beam and accounts for particles contained within bunches as well as any debunched charges.

The concept of bunch current i_b helps with obtaining an insight into the temporal distribution of the beam. A bunch made of N particles with a charge e_0 each, occupying a dedicated bunch spacing interval T_b constitutes an instantaneous current:

$$i_\mathrm{b}(t) = e_0 \frac{\mathrm{d}N}{\mathrm{d}t}\bigg|_{-\frac{1}{2}T_\mathrm{b}}^{+\frac{1}{2}T_\mathrm{b}} \tag{2.4}$$

The above definition directly implies that the shape of a bunch current pulse is the same as its longitudinal profile. For example, the instantaneous current of a gaussian-shaped bunch with a standard deviation σ is given by:

$$i_\mathrm{b}(t) = \frac{e_0 N}{\sqrt{2\pi}\sigma} \exp\left(\frac{-t^2}{2\sigma^2}\right)\bigg|_{-\frac{1}{2}T_\mathrm{b}}^{+\frac{1}{2}T_\mathrm{b}} \tag{2.5}$$

2.1.3 Image current

A stationary charged particle Q in vacuum with permittivity ϵ_0 is associated with its electric field $\vec{E}$ which at a distance r from the particle is given by [2, p. 4-9]:

$$\vec{E} = \frac{Q}{4\pi\epsilon_0 r^3}\vec{r} \tag{2.6}$$

As long as the studied particle is stationary in the chosen frame of reference, there is no magnetic field $\vec{H}$ which can be derived from it [2, p. 13-1]. For particles in motion, both $\vec{E}$ and $\vec{H}$ become non-zero and time-varying.

Following Lorentz transformation, the electric and magnetic fields produced by a charged particle moving at a constant velocity $|v| = \beta c$, with c being the speed of light in vacuum, can be expressed as [25]:

$$\vec{E} = \frac{Q}{4\pi\epsilon_0 r^3} \frac{1-\beta^2}{\left(1-\beta^2 \sin^2\theta\right)^{\frac{3}{2}}}\vec{r} \tag{2.7}$$

$$\vec{H} = \epsilon_0 \left(\vec{v} \times \vec{E}\right) \tag{2.8}$$

where θ is the angle between $\vec{r}$ and $\vec{v}$.

For a particle moving along the z axis in a three-dimensional coordinate system (x, y, z), eq. 2.7 can be split into its Cartesian components:

$$E_x = \frac{Q}{4\pi\epsilon_0} \frac{1}{\sqrt{1-\beta^2}} r_x \tag{2.9}$$

$$E_y = \frac{Q}{4\pi\epsilon_0} \frac{1}{\sqrt{1-\beta^2}} r_y \tag{2.10}$$

$$E_z = \frac{Q}{4\pi\epsilon_0} \left(1-\beta^2\right) r_z \tag{2.11}$$

At high particle velocities, i.e. high values of β, the transverse electric field components E_x and E_y increase, whilst the longitudinal components E_z decreases. For relativistic particles with $\beta \approx 1$ an assumption that the electromagnetic field is purely transverse is often justified.

In most particle accelerators the beam travels inside a grounded metal vacuum chamber which yields a well-defined boundary condition for eq. 2.7. A charged particle in an infinitely long round metal tube does not generate any electric field lines parallel to the tube's axis, meaning that all the field lines collapse on the tube walls [26]:

$$\vec{E}_{||} = 0 \tag{2.12}$$

Since there cannot be any electric field inside a perfect conductor, the Gauss's law dictates that an equal charge of the opposite sign induced on the tube's inner wall must balance any charge contained within an infinitely long conducting tube [2, p. 6-9]. In particle accelerators, such charge induced by the beam on the vacuum chamber walls is often referred to as the image or wall charge. A complete mathematical description of the image charge distribution is complicated and requires solving Bessel functions [27]. However, the Root Mean Square (RMS) value σ_w of this distribution has a simple form which depends only on the beam pipe radius r_BP and the particle velocity in relation to the speed of light in vacuum $v = \beta c$ [26]:

$$\sigma_\mathrm{w} = \left(1 - \beta^2\right) \frac{r_\mathrm{BP}}{\sqrt{2}} \tag{2.13}$$

As the particle's speed increases, σ_w decreases implying that the image charge focuses transversely to the particle. In the relativistic limit $\beta \to 1$ all image charge is contained on a plane perpendicular to the particle motion, as shown in Fig. 2.2.

For a beam charge Q_B made of multiple moving particles, the induced image charge Q_w is a superposition of the image charges due to the individual particles. As illustrated in Fig. 2.3, at a ultra-relativistic velocity with $\beta \approx 1$ the longitudinal densities of both charges along the motion axis z are the same:

$$Q_\mathrm{W}(z) = -Q_\mathrm{B}(z) \tag{2.14}$$

Based on eq. 2.4, this implies that for an ultra-relativistic beam made of N particles with a charge e_0 each, the electric current caused by the image charge is equal to the instantaneous beam current with the opposite sign:

$$i_\mathrm{w}(t) = -e_0 \frac{\mathrm{d}N}{\mathrm{d}t} = -i_\mathrm{b}(t) \tag{2.15}$$

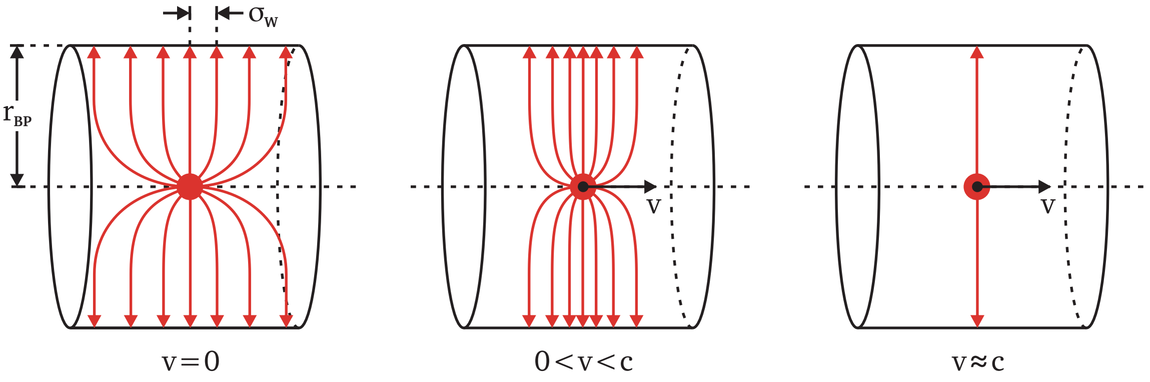

Figure 2.2: Lorentz contraction of the image field lines for a particle at rest (a), travelling below the speed of light (b), and travelling at approximately the speed of light in vacuum (c).

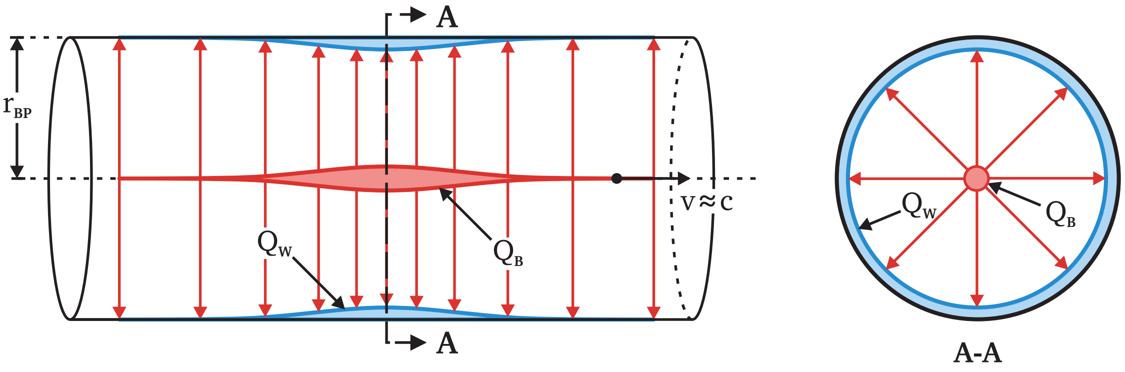

Figure 2.3: Image charge Q_W induced on the vacuum chamber by an ultrarelativistic beam Q_B.

This current is typically referred to as the image or wall current. Operation of many beam instrumentation systems, including beam current monitors described in detail further, often relies on the existence of the wall current. However, an important caveat to emphasise is that the wall current is a result of longitudinal beam charge density modulation. Therefore, DC beams do not induce it neither does it exist for the DC component of bunched beams.

The image charge induced by ultra-relativistic beams has the same longitudinal density as the the beam charge regardless of the transverse beam position. Its azimuthal distribution, on the other hand, strictly depends not only on the beam position but also on the shape of the vacuum chamber [28]. This effect must be taken into account during design of any beam instrumentation sensor intended to use the wall current as a proxy to beam charge measurements.

2.1.4 From current to charge, to intensity

The beam and image currents are manifestations of the respective charges and can as such become intermediaries for beam intensity measurements.

Let's consider an ideal sensor generating a signal which mirrors the instantaneous beam current i_B over some period $[t_0, t_1]$. By definition, electric current is the rate of flow of charge through some reference region. Integrating the measured current i_B over the period $[t_0, t_1]$ yields the beam charge Q_B which had traversed through the ideal sensor (constituting the reference region):

$$Q_B = \int_{t_0}^{t_1} i_B(t)\,\mathrm{d}t \tag{2.16}$$

In a vast majority of cases, beams used in scientific accelerators comprise a single particle type with a known charge. Hence, dividing the beam charge Q_B by the single particle charge e_0 gives the beam intensity, i.e. the number of particles making up the beam:

$$N_B = \frac{Q_B}{e_0} = \frac{1}{e_0}\int_{t_0}^{t_1} i_B(t)\,\mathrm{d}t \tag{2.17}$$

2.1.5 Integrals of low-pass filtered signals

Let's consider a particle beam going around a circular accelerator with a revolution period of 2π. Due to its inherent periodicity, the beam current i_{B} expands to a Fourier series:

$$i_{\mathrm{B}}(t) = a_0 + \sum_{n=1}^{\infty} a_n \cos(n\,t) + \sum_{n=1}^{\infty} b_n \sin(n\,t) \tag{2.18}$$

where a_0 is a frequency-independent term and a_n, b_n are coefficients of the nth harmonic component of the beam spectrum.

In order to obtain the total circulating beam charge Q_{B} one can integrate the beam current over the revolution period 2π:

$$Q_{\mathrm{B}} = \int_0^{2\pi} i_{\mathrm{B}}(t)\,\mathrm{d}t = \int_0^{2\pi} \left(a_0 + \sum_{n=1}^{\infty} a_n \cos(n\,t) + \sum_{n=1}^{\infty} b_n \sin(n\,t) \right) \mathrm{d}t \tag{2.19}$$

which, applying the linearity of integration principle, can be rewritten as:

$$Q_{\mathrm{B}} = 2\pi\,a_0 + \sum_{n=1}^{\infty} \left(a_n \int_0^{2\pi} \cos(n\,t)\,\mathrm{d}t \right) + \sum_{n=1}^{\infty} \left(b_n \int_0^{2\pi} \sin(n\,t)\,\mathrm{d}t \right) \tag{2.20}$$

Considering that integration of the cosine and sine functions over any multiple of the fundamental period 2π gives 0:

$$\int_0^{2\pi} \cos(n\,t)\,\mathrm{d}t = \int_0^{2\pi} \sin(n\,t)\,\mathrm{d}t = 0 \tag{2.21}$$

the two sum terms in equation 2.20 cancel out, finally yielding:

$$Q_{\mathrm{B}} = 2\pi\,a_0 \tag{2.22}$$

Since no assumptions about the signal temporal structure were made, the above reasoning proves that the information about the beam charge is contained in the 0 Hz component of the beam current provided that the integration period covers the entire signal.

One could argue that beam intensity measurements do not require the high frequency components of the beam current to be measured. However, without those components, the duration of the observed signal increases since any sharp rising and falling edges effectively stretch out. Consequently, the integration period required to contain the entire signal also increases.

Let's consider a signal $y(t)$ defined as:

$$y(t) = \frac{Q}{t_1} \cdot \begin{cases} 0 & t < 0 \\ 1 & 0 \le t \le t_1 \\ 0 & t > t_1 \end{cases} \tag{2.23}$$

An ideal first-order low-pass linear-phase filter with a cut-off frequency $f = (2\pi\tau)^{-1}$ with

$y(t)$ at the input, generates an output signal $y'(t)$ [29, pp. 53–55]:

$$y'(t) = \frac{Q}{t_1} \cdot \begin{cases} 0 & t < 0 \\ 1 - \exp\frac{-t}{\tau} & 0 \leq t \leq t_1 \\ \exp\frac{-(t-t_1)}{\tau} - \exp\frac{-t}{\tau} & t > t_1 \end{cases} \tag{2.24}$$

Figure 2.4, showing both $y(t)$ and $y'(t)$, clearly demonstrates the low-pass filter stretching effect. Following low-pass filtering also the signal amplitude decreases.

To study the importance of choosing an appropriate integration window for low-pass signals, let's integrate both $y(t)$ and $y'(t)$ over a period $[0, t_2]$ such that:

$$0 < t_1 < t_2 \tag{2.25}$$

Integration of the original signal yields:

$$\int_0^{t_2} y(t)\,\mathrm{d}t = \frac{Q}{t_1}\left(\int_0^{t_1} \mathrm{d}t + \int_{t_1}^{t_2} 0\,\mathrm{d}t\right) = Q \tag{2.26}$$

The integral of the low-passed signal has a more complicated form:

$$\int_0^{t_2} y'(t)\,\mathrm{d}t = \frac{Q}{t_1}\left(\int_0^{t_1} \mathrm{d}t - \int_0^{t_1} \exp\frac{-t}{\tau}\,\mathrm{d}t + \int_{t_1}^{t_2} \exp\frac{-(t-t_1)}{\tau}\,\mathrm{d}t - \int_{t_1}^{t_2} \exp\frac{-t}{\tau}\,\mathrm{d}t\right) \tag{2.27}$$

which reduces to:

$$\int_0^{t_2} y'(t)\,\mathrm{d}t = Q\left(1 - \frac{\tau}{t_1}\exp\frac{-t_2}{\tau}\left(\exp\frac{t_1}{\tau} - 1\right)\right) \tag{2.28}$$

The exact solution to eq. 2.28 depends on the relations between the input pulse duration t_1, the integration window t_2 and the low-pass filter time constant τ. The equation can be further analysed for a special case whereby the input pulse is much shorter than the integration window i.e. $t_1 \ll t_2$ or $t_1 \to 0$.

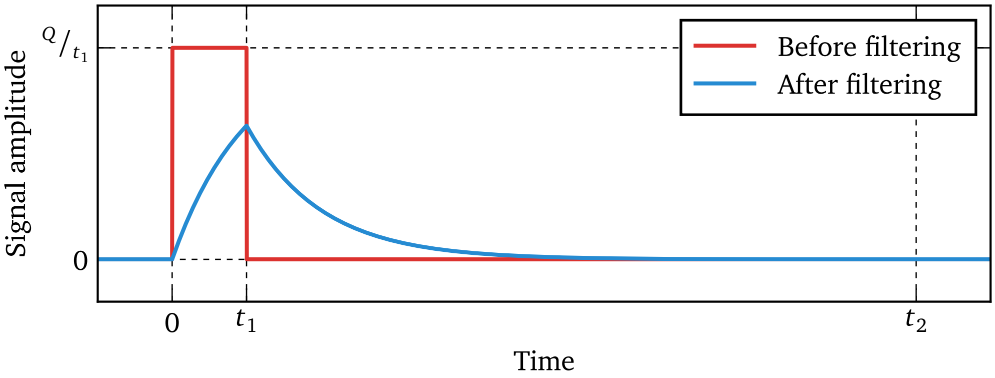

Figure 2.4: Generalised time response of a low-pass filter.

With L'Hospital's rule, one can prove that:

$$\lim_{t_1 \to 0} \frac{1}{t_1} \left(\exp \frac{t_1}{\tau} - 1 \right) = \frac{1}{\tau} \tag{2.29}$$

For the special case explained above, eq. 2.28 reduces to:

$$\lim_{t_1 \to 0} \int_0^{t_2} y'(t)\,\mathrm{d}t = Q \left(1 - \exp \frac{-t_2}{\tau} \right) \tag{2.30}$$

Let α be the ratio of the integrals of $y'(t)$ and $y(t)$ when $t_1 \to 0$. To chose an integration window t_2 which guarantees capturing a given ratio of the true signal integral when using a low-pass filter with a time constant τ, one can use the following inequality:

$$\int_0^{t_2} y'(t)\,\mathrm{d}t \geq \alpha Q \quad \Leftrightarrow \quad Q \left(1 - \exp \frac{-t_2}{\tau} \right) \geq \alpha Q \tag{2.31}$$

which can be solved for t_2:

$$t_2 \geq \tau \ln \left(\frac{1}{1-\alpha} \right) \tag{2.32}$$

It is then possible to calculate that to contain e.g. 99.99 % of the low-passed signal integral, the integration window t_2 must be at least 9.21 time longer than the filter's time constant τ.

Even though the above analysis assumed idealised signals and filters, its results can help with an early evaluation if it is likely that a given configuration will achieve the specified precision. Nevertheless, more accurate numerical simulations using realistic inputs and filters should be performed whenever low-pass signals are to be precisely integrated. Figures 2.5 and 2.6 show examples of such simulations for typical LHC bunch current signals.

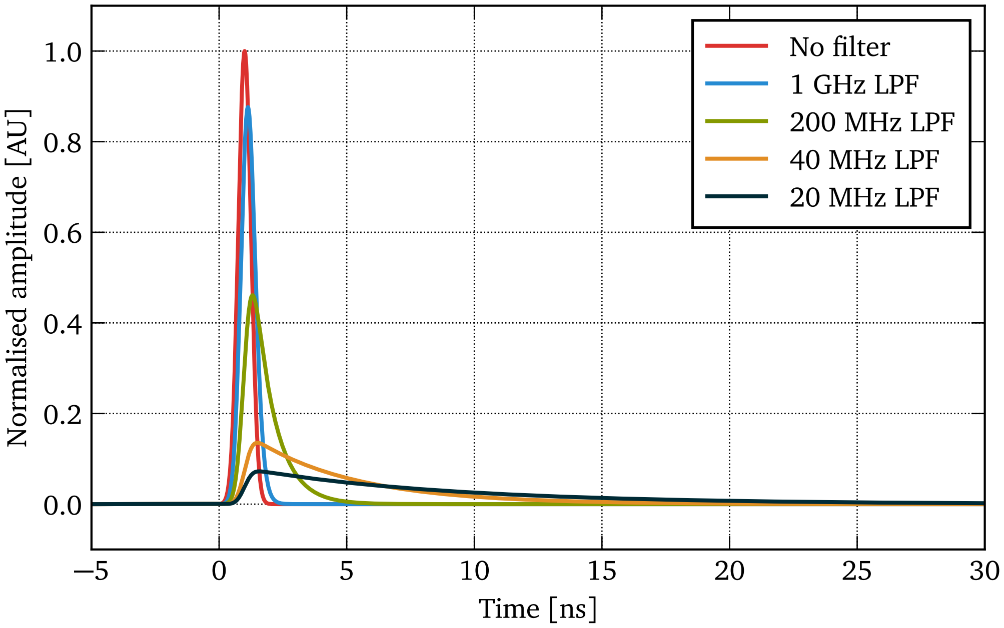

Figure 2.5: Time-domain effect of low-pass filtering on a typical LHC bunch.

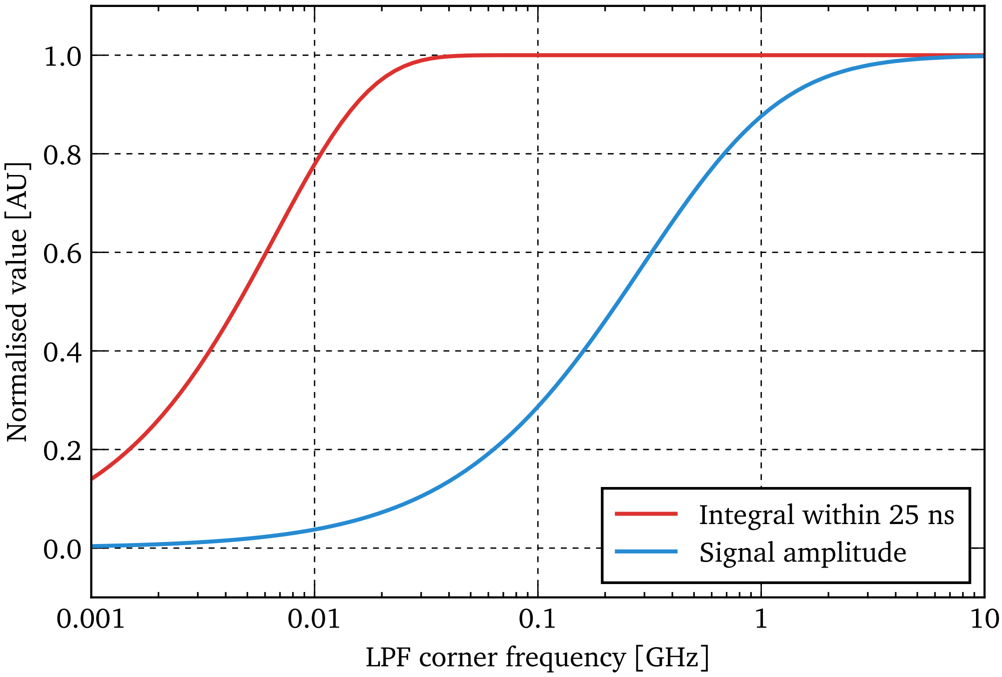

Figure 2.6: Effect of low-pass filter's corner frequency on a typical LHC bunch.

2.1.6 Bunch intensity measurements with no DC component

Some sensors used for beam instrumentation have reduced sensitivity at low frequencies and might even be incapable of measuring purely static DC signals. The previous section showed that the lack of the DC component would result in the signal integral equal to 0 for a very long integration period. However, this is not necessarily the case if shorter intervals are analysed.

Let's consider a signal $y(t)$ defined as in the previous section:

$$y(t) = \frac{Q}{t_1} \cdot \begin{cases} 0 & t < 0 \\ 1 & 0 \leq t \leq t_1 \\ 0 & t > t_1 \end{cases} \tag{2.33}$$

After passing through an ideal first-order high-pass linear-phase filter with a cut-off frequency $f = (2\pi\tau)^{-1}$, $y(t)$ becomes $y''(t)$ [29, pp. 53–55]:

$$y''(t) = \frac{Q}{t_1} \cdot \begin{cases} 0 & t < 0 \\ \exp\frac{-t}{\tau} & 0 \leq t \leq t_1 \\ \exp\frac{-t}{\tau} - \exp\frac{-(t-t_1)}{\tau} & t > t_1 \end{cases} \tag{2.34}$$

With a non-zero value for $t > t_1$, it is evident that high-pass filters also stretch their input signals. Contrary to low-pass filters, the output signal polarity changes at t_1 as demonstrated in Fig. 2.7.

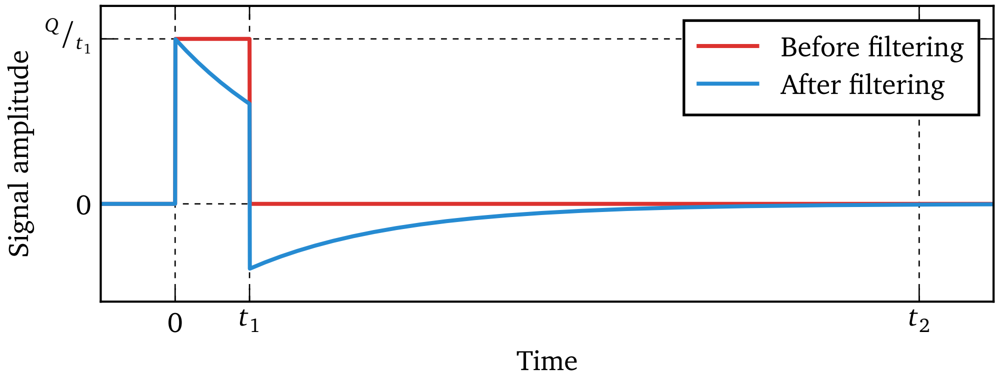

Figure 2.7: Generalised time response of a high-pass filter.

To evaluate the impact of the lack of the DC component, one can follow the analysis described in the previous section. Integration of both $y(t)$ and $y''(t)$ over a period $[0, t_2]$ $(0 < t_1 < t_2)$ yields:

$$\int_0^{t_2} y(t)\,\mathrm{d}t = \frac{Q}{t_1}\left(\int_0^{t_1} \mathrm{d}t + \int_{t_1}^{t_2} 0\,\mathrm{d}t\right) = Q \tag{2.35}$$

$$\int_0^{t_2} y''(t)\,\mathrm{d}t = \frac{Q\tau}{t_1} \exp\frac{-t_2}{\tau}\left(\exp\frac{t_1}{\tau} - 1\right) \tag{2.36}$$

For an input pulse much shorter than the integration window (i.e. $t_1 \to 0$), the second integral reduces to:

$$\lim_{t_1 \to 0} \int_0^{t_2} y''(t)\,\mathrm{d}t = Q \exp\frac{-t_2}{\tau} \tag{2.37}$$

Let β be the ratio of the integrals of $y''(t)$ and $y(t)$ when $t_1 \to 0$. To chose the time constant of a high pass filter τ which guarantees capturing a given ratio of the true integral of a high-passed signal over the integration interval t_2, one can use the following inequality:

$$\int_0^{t_2} y''(t)\,\mathrm{d}t \geq \beta Q \quad \Leftrightarrow \quad Q \exp\frac{-t_2}{\tau} \geq \beta Q \tag{2.38}$$

which after solving for τ yields:

$$\tau \geq \frac{-t_2}{\ln\beta} \tag{2.39}$$

The above inequality leads to the conclusion that to contain e.g. 99.99 % of the high-passed signal integral, the filter time constant τ must be at least 9999.5 times longer than the considered integration window t_2. Although the same integration precision was considered, the required ratio of t_2 to τ is over three orders of magnitude higher than in the case of low-passed signals.

Once again the analysis assumed idealised signals and filters. Nevertheless, its results clearly highlight the fact that without the low frequency components, using long integration windows leads to imprecise results. One can accurately estimate the measurement error due to high-pass filtering with numerical simulations using realistic signals and filters. Figures 2.8 and 2.9 exemplify this for typical LHC bunch current signals.

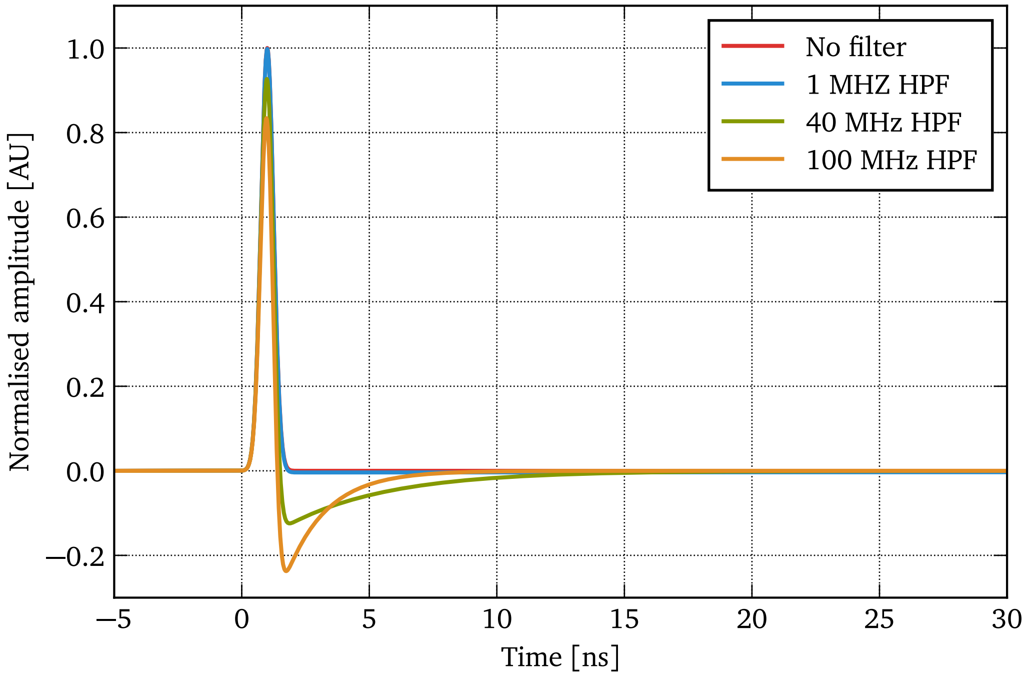

Figure 2.8: Time-domain effect of high-pass filtering on a typical LHC bunch.

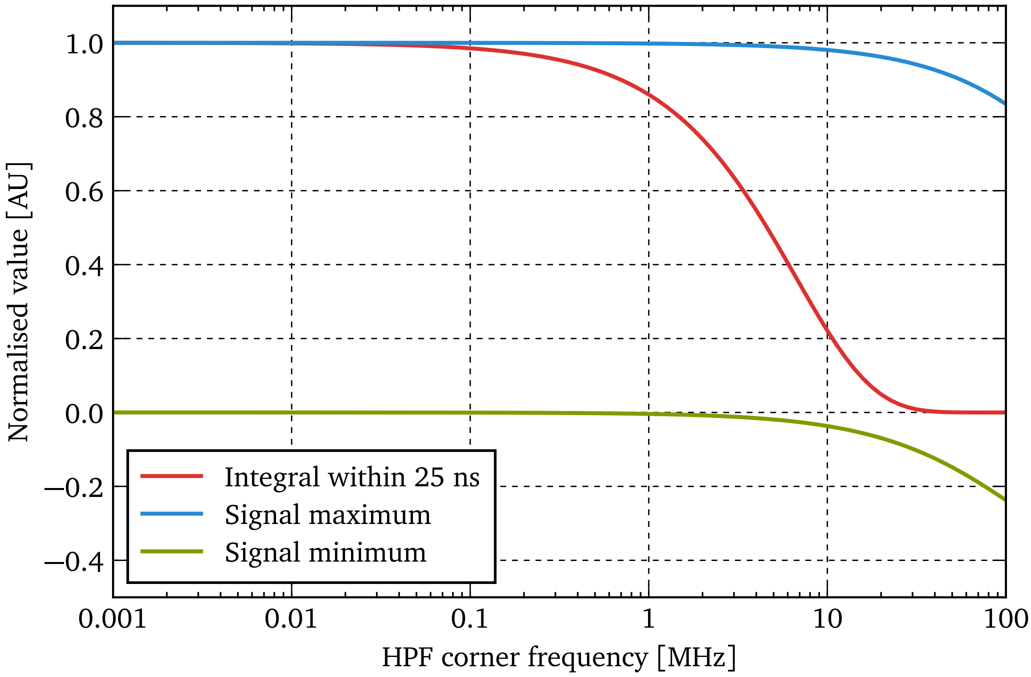

Figure 2.9: Effect of high-pass filter's corner frequency on a typical LHC bunch.

2.2 Common beam intensity monitors

Over the years, researchers developed several beam intensity monitoring techniques, most of which derive the beam intensity from measuring either the beam charge or the beam current, as explained in section 2.1.4. As no two HEP accelerators are exactly the same, there can be no universal beam intensity measurement system. This section describes the four most commonly used monitor types. Other solutions exist for more unusual types of beams, but, as they would not be applicable at the LHC, they are not discussed in detail.

2.2.1 Faraday cup

The most direct approach to measuring the beam current is to intercept the beam particles with a conductive target and measuring the resulting current. Such sensors, called Faraday cups [19, pp. 144–146], have been widely used since the very first accelerators were built.

When a particle beam hits a Faraday cup some of the charges backscatter, i.e. deflect backwards and escape the cup. Additionally, interactions of the beam particles with the cup atoms can lead to an emission of electrons from the cup surface due to multiple scattering. Both of these phenomena are sources of potential measurement errors and have to be taken into account when designing a Faraday cup. Two techniques commonly used to increase measurement accuracy are making the cup's opening as small as possible and applying a bias voltage or magnetic field at the cup's entrance. The former presents a physical barrier for the escaping charges while the latter creates an electromagnetic trap for low-energy particles. Figure 2.10 presents an idealised realisation of a Faraday cup using a perfect ammeter to measure the incident current.

Intercepting the entire beam becomes a major engineering challenge at higher beam energies. Extremely energetic particles can travel through significant distances in ordinary materials before they are absorbed. Moreover, dissipating the immense beam power converted into heat might require a sophisticated high-capacity cooling circuit.

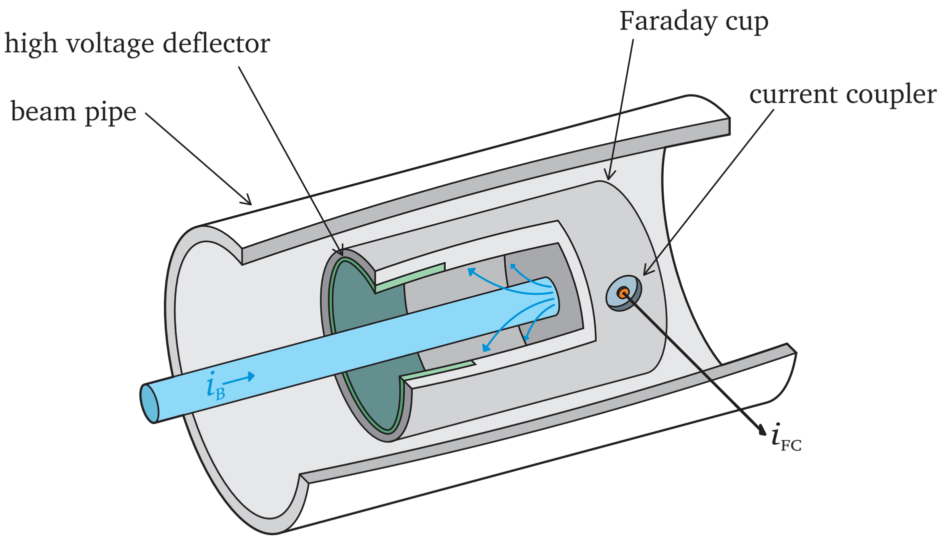

Figure 2.10: Principle of operation of a Faraday Cup.

Faraday cups are totally destructive sensors as they effectively remove the measured beam from the accelerator. Their use is limited to when it is possible to recreate a beam of the same parameters in a short period of time. Nevertheless, Faraday cups find broad application in low energy accelerators due to their simplicity and excellent sensitivity to low intensity beams.

2.2.2 Wall Current Monitor

Wall Current Monitors (WCMs) are non-intercepting sensors measuring the wall current defined in section 2.1.3. A simple WCM features a number of resistors installed over an insulating insert placed in the vacuum chamber [19, pp. 146–147].

The resistors electrically connect the beam pipe sections on either side of the insert. Since the insert breaks a conductive path for the image current, it forces the charges to flow through the resistors. Therefore, by measuring the voltage v_{WCM} across the resistors R_{WCM}, one can easily derive the beam current i_{B} following Ohm's law:

$$i_{\mathrm{B}} = -\frac{v_{\mathrm{WCM}}}{R_{\mathrm{WCM}}} \tag{2.40}$$

To avoid radiating the beam fields into the accelerator environment, a conductive shielding encloses the resistors. This introduces a competing path for the image current, part of which would not flow through the resistors, leading to a measurement error. To address this issue, the space between the resistors and the shielding can be expanded and filled with magnetic material such as ferrite. High permeability of the filler material effectively increases the shielding impedance forcing a higher fraction of the image current to flow through the WCM resistors. Moreover, due to their lossy characteristics, ferrites absorb the electromagnetic resonances which would otherwise be created in the hollow space inside the shielding.

The third possible path an image current can take is through the capacitance of the dielectric insert which typically limits the high-frequency performance of WCMs. Minimising the insert capacitance is a significant engineering challenge and some WCMs replace the insulating insert with a vacuum gap to lower the permittivity [30].

Figure 2.11 shows these three possible current paths together with an equivalent circuit of a simple WCM. The very low frequency components of the image current flow through the shielding whilst the high frequency components jump across the insert. The intermediate spectral components develop a voltage across the sensing resistance R.

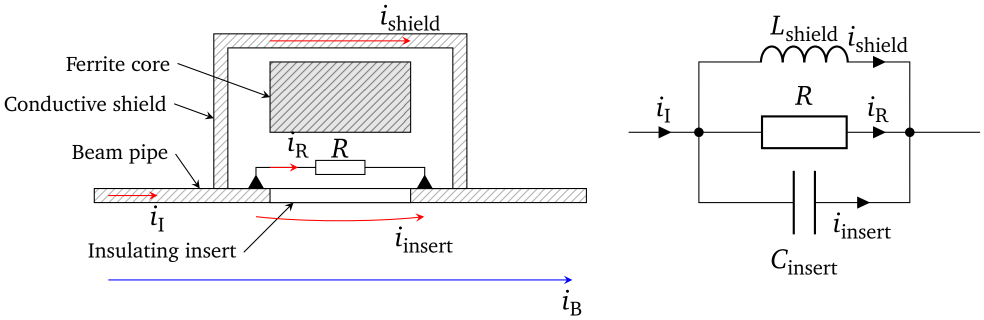

Figure 2.11: Principle of operation of a Wall Current Monitor.

As explained in section 2.1.3, the wall current does not carry any DC signal corresponding to the beam charge. Even an ideal WCM with infinitely high shielding inductance could not sense non-bunched beams. Moreover, due to the non-uniform azimuthal distribution of the image charge for off-centred beams, WCM are inherently prone to an unwanted sensitivity to the transverse beam position. A successful mitigation technique for this issues is using multiple resistors distributed around the beam pipe and carefully combining their individual signals.

2.2.3 Beam Current Transformer

The intensity of the magnetic field generated by a particle beam in motion is proportional to the beam charge [19, pp. 148–152]. A family of sensors collectively referred to as Beam Current Transformers (BCTs) exploit this phenomena. Their principle of operation is very similar to a classical current transformer, however, their primary winding is replaced by a particle beam traversing a magnetic core wound with the secondary winding. There are many variations of BCTs optimised for different temporal structures of particles beams. The three most commonly used BCT types are described below.

AC Current Transformer

The AC Current Transformer (ACCT), also interchangeably referred to as the Fast Beam Current Transformer (FBCT), consists of a single high-permeability magnetic core installed over a dielectric insert placed in the vacuum chamber. The core is wound with a wire the ends of which are connected through a sensing resistor R_{BCT} as shown in Fig. 2.12.

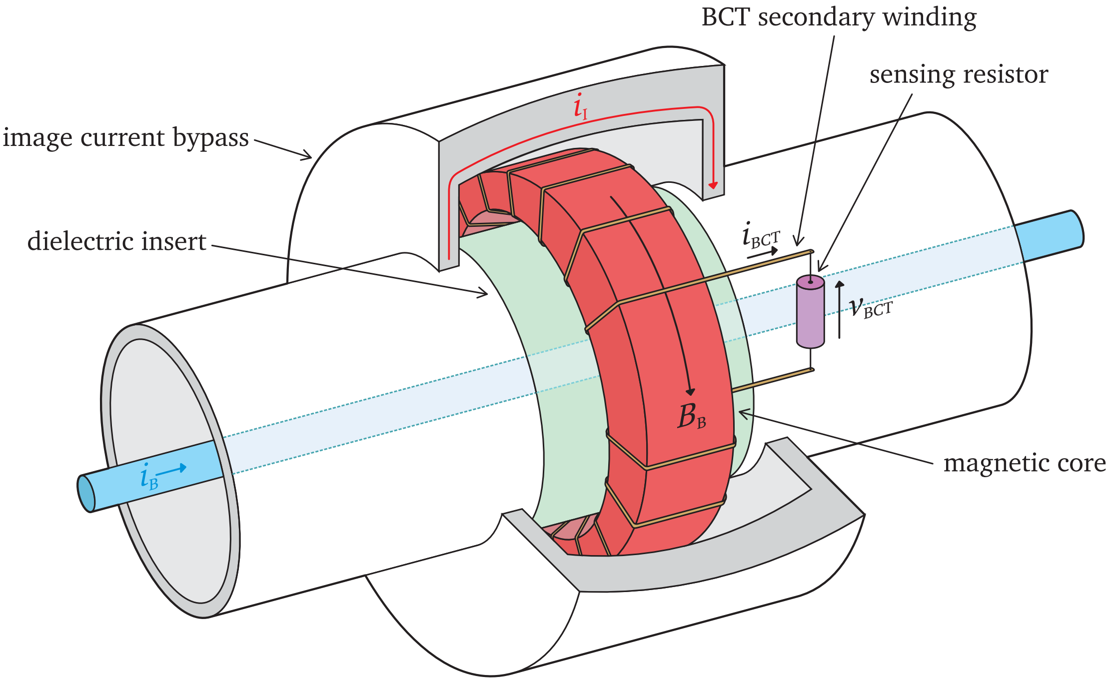

Figure 2.12: Principle of operation of an AC Current Transformer.

A beam current i_B induces a magnetic field B_B in the core [2, pp. 36.6–36.9]:

$$B_\mathrm{B} = \mu_\mathrm{r}\mu_0 \frac{1}{2\pi r} i_\mathrm{B} \tag{2.41}$$

where μ_r is the relative permeability of the core, μ_0 is the vacuum permeability and r is the average radius of the core. Equation 2.41 assumes that the beam current is low enough not to magnetically saturate the core, which is usually the case for ACCTs.

The time-varying field B_B then induces a current i_BCT in the wire wound N times around the core which is proportional to the beam current [2, pp. 36.6–36.9]:

$$i_\mathrm{BCT} = \frac{1}{N}\frac{2\pi r B_\mathrm{B}}{\mu_\mathrm{r}\mu_0} = \frac{1}{N} i_\mathrm{B} \tag{2.42}$$

Using Ohm's law, one can derive the beam current from the voltage measured across the sensing resistor R_BCT:

$$i_\mathrm{B} = N \frac{v_\mathrm{BCT}}{R_\mathrm{BCT}} \tag{2.43}$$

The above equation is valid for intermediate and high frequencies. However, ACCTs are inherently limited at low frequencies. The winding around the ACCT core constitutes an inductance L_BCT [2, p. 36.9]:

$$L_\mathrm{BCT} = \mu_\mathrm{r}\mu_0 \frac{A}{r} N^2 \tag{2.44}$$

where A is the cross-sectional area of the core. This inductance and the sensing resistor create a high-pass filter with a cut-off frequency of [29, pp. 112–113]:

$$f_\mathrm{BCT} = 2\pi \frac{R_\mathrm{BCT}}{L_\mathrm{BCT}} \tag{2.45}$$

As described in section 2.1.6, the lack of low-frequency components in the ACCT signal limits the beam charge measurement accuracy for long integration windows. When necessary, very high permeability magnetic cores and a reduced reducing value of the sensing resistance can decrease the inherent ACCT low cut-off frequency.

Much like for the WCM, the dielectric insert breaks the conductive path for the image current. To avoid any electromagnetic field of the beam leaking into the accelerator environment, a conductive housing forming an image current bypass typically surrounds the ACCT magnetic core. The empty volume inside the housing should be minimised not to create a resonant cavity trapping some components of the beam field.

Since ACCTs couple directly to the electromagnetic field of a particle beam, the sensor can be calibrated by running a known current or charge through a conductor installed in the core centre. In practice, an additional wire wound around the core serves as the primary winding during calibration. To minimise measurement error, care needs to be paid to avoid any capacitive coupling between the calibration and the measurement windings as well as to reduce coupling between the beam and the calibration winding.

DC Current Transformer

Due to their inherent sensitivity to time-varying magnetic fields, the aforementioned ACCTs can measure only the part of the beam current which is caused by a longitudinal variation in the charge density. In some circular accelerators, physicists monitor also the total circulating charge including any potentially unbunched particles. A common solution for this task are the DC Current Transformers (DCCTs) which resemble fluxgate magnetometers and exploit non-linear nature of the magnetic hysteresis loop [31].

A typical DCCT consists of two identical cores made of a soft ferromagnetic material featuring their individual windings and an additional common winding installed around both cores. Periodic modulation signals sent to the independent windings drive the cores into magnetic saturation in anti-phase for each core. The common winding acts as the monitor's output. Without a particle beam present, the anti-symmetric modulation cancels out any signal induced on the sensing winding by the external excitation. Adding a beam current changes the magnetic working point of each core effectively breaking the modulation's anti-symmetry leading to some signal appearing on the monitor's output.

Some DCCTs operate in a feedback mode whereby yet another common winding adds an external quasi-DC signal. In such configuration, when the quasi-DC signal is equal to the beam current but has the opposite polarity, the modulation anti-symmetry between the two cores is restored and no signal appears on the monitor's output. It is then sufficient to measure the current set automatically by a feedback loop designed to maintain the DCCT output at 0 rather than to directly measure the monitor's output.

Optimised DCCTs are very sensitive and accurate monitors reaching a measurement resolution of 1 µA [31]. Such performance requires two nearly identical magnetic cores which, in practice, is extremely difficult to achieve.

DCCTs can be precisely calibrated using static signals and in some accelerator facilities they are the reference beam current monitors used to cross-calibrate other sensors. Nevertheless, DCCTs cannot sense any temporal variation in the beam current and are typically accompanied by another kind of faster monitor.

Integrating Current Transformer

The Integrating Current Transformers (ICTs) exploit the phenomenon explained in section 2.1.5 whereby the signal integral is carried by only its low-frequency components for sufficiently long integration windows. The ICT intentionally "stretches" its output signal by pre-integrating the measured bunch current which leads to a permanent loss of any information about precise longitudinal distribution of the bunch charge.

Most of the ICTs installed in accelerator laboratories around the world are commercial devices with proprietary non-published design. Some facilities tried to developed their own ICTs by enclosing a magnetic core in a conductive shell with a capacitive gap [32]. The shell forms a low-pass filter for the electromagnetic field carried by a particle beam which is equivalent to pre-integrating the signal.

ICTs are a good solution to measure low-duty-cycle beams in which the bunches are much shorter than the bunch spacing or a train of bunches is followed by a relatively long empty period. In such conditions, the sensor works similar to an envelope detector and, provided sufficiently large bunch spacing, the ICT can measure intensity on a bunch-by-bunch basis.

Calibrating ICTs is possible following the ACCT approach by introducing an extra winding for a known current or charge. Monitors operating as envelope detectors might require the calibration signal's shape to resemble that of the particle beam.

2.2.4 Beam Position Monitor

As the electromagnetic field magnitude is proportional to the current causing it, most detectors used in beam instrumentation are inherently sensitive to the beam current. Sensors optimised to measure another observable can often act as beam intensity monitors. A prime example of this are Beam Position Monitors (BPMs) which in some cases reach better beam charge measurement resolution than dedicated beam intensity monitors [33].

An ordinary BPM consists of two or four antennas installed inside the vacuum chamber coupling to the electromagnetic field carried by a particle beam [34]. Typically, the BPM antenna distribution is azimuthally symmetric around the ideal beam motion axis. For a perfectly centred beam, the signals of all antennas are equal and proportional to the beam intensity. As the beam moves closer to one antenna, its signal increases while those of the remaining antennas decrease. Small differences between those signals infer the transverse beam position.

For such a BPM the sum of all antenna signals is proportional to the beam intensity regardless of its transverse position [34]. This makes BPMs an attractive candidate for beam intensity monitoring especially in accelerators where the space is sparse and installing dedicated instrumentation for measuring the beam charge might not be possible.

2.3 Beam intensity measurements in the LHC

2.3.1 Beams in the LHC

In general, beam instrumentation sensors are optimised for a given accelerator and the type of beam it uses. Table 2.1 and the following paragraphs summarise those parameters of the LHC beams which are most important for beam and bunch intensity measurements. An exhaustive list of other parameters is available in the LHC Design Report [35].

Each of the LHC rings has a circumference of 26.659 km. A particle beam travelling virtually at the speed of light takes 88.925 µs to complete one turn around the accelerator which yields a revolution frequency of 11.245 kHz.

Superconducting RF cavities operating at 400.8 MHz accelerate the LHC beams. This RF frequency defines the fundamental limit for the minimum distance between two consecutive bunches of 2.495 ns with the maximum number of slots, called the RF buckets, available for bunches being 35 640. In practice, a vast majority of them remains empty and the number of circulating bunches in each ring does not exceed 2808.

During regular LHC operation, only one in every ten buckets can potentially contain a bunch

Table 2.1: Parameters of common LHC bunches.

	Pilot	Nominal	Future	Ion
Intensity [charges]	5×10^9	1.2×10^{11}	2.2×10^{11}	5×10^9
Charge [nC]	0.8	19.23	35.25	0.8
Peak current [A]	1.28	30.68	56.25	1.28
Bunch spacing [ns]	multiple of 24.95			
Bunch length [ns]	1.0 to 1.2			

increasing the effective bunch spacing tenfold to 24.95 ns[1]. A rare exception to this is when the accelerator runs in the so-called doublet mode in which each bunch is split into two separate parts spaced by 4.99 ns followed by a 19.96 ns long empty gap. Furthermore, some of the 24.95 ns slots must remain empty due to the manner in which the beam travels through successive parts of the accelerator complex. Most notably, the LHC beam must imperatively contain a particle-free window of at least 3 µs, referred to as the abort gap, to accommodate the time it takes to reconfigure the accelerator to safely dispose of the beam.

The longitudinal charge distribution within a typical LHC bunch is approximately Gaussian. The bunch length, defined as four standard deviations of a fitted gaussian curve (σ_b), varies between 1.0 and 1.6 ns with bunches as short as 0.6 ns used for dedicated physics studies [24].

Beams circulating in the LHC predominantly consist of protons which are the most fundamental charged hadron. Occasionally, one or both LHC rings accelerate bunches made of heavy ions with fully-stripped lead nuclei being used the most commonly.

A nominal LHC bunch used for high-energy proton collisions contains around 1.2×10^{11} particles yielding a charge of 19.23 nC and a peak current of 30.68 A. Before injecting any such high-intensity bunch into the accelerator, physicists validate the machine configuration with a single low-intensity bunch, typically referred to as a pilot bunch, made of around 5×10^9 particles (charge of 0.8 nC, peak current of 1.28 A). Pilot bunches are instrumental also during study periods to minimise any risk when the accelerator uses non-standard setting. In the future, after a series of planned major upgrades, the nominal bunch intensity might increase up to 2.2×10^{11} protons per bunch (charge of 35.25 nC, peak current of 56.25 A). The ion bunches typically have intensity close to that of a proton pilot, i.e. 5×10^9 charges per bunch.

Intensity of the entire LHC beam can vary from a single pilot bunch to a set of 2808 nominal bunches spanning almost 5 orders of magnitude between 5×10^9 and 3.37×10^{14}. The equivalent DC beam current ranges from 9 µA to 607 mA.

2.3.2 LHC Fast Beam Current Transformers and DC Current Transformers

The substantial difference between the peak bunch current and the DC beam current warrants using a dedicated type of beam instrumentation sensor to measure each one of them. Moreover, like in most HEP accelerators, the LHC requires constant monitoring of the number of unbunched

---

[1] For the sake of simplicity this number is commonly rounded up to 25 ns in publications. Operational systems derive the exact bunch spacing time from a precise RF signal distributed around the accelerator. The same convention will be followed in the remainder of this thesis.

particles constituting DC current to ensure safety of the machine.

Two DCCTs installed on each LHC ring measure the total circulating beam intensity. They were designed at CERN and feature three magnetic cores made of a high-permeability nanocrystaline alloy [36]. Two cores, carefully paired to be nearly identical, perform DC measurements as described in section 2.2.3 whilst the third one forms a simple ACCT to extend the sensor's bandwidth. A specially designed magnetic shielding isolates the DCCTs from any external interference which could potentially impair the measurement.

In the first years of the LHC operation, intensities of individual bunches were measured with ACCTs which at CERN are commonly referred to as Fast Beam Current Transformers (FBCTs). There are two such sensors, based on a commercial 1 : 40 transformer developed by Bergoz Instrumentation, on each LHC ring [37]. The FBCTs and their front-end electronics work over a wide frequency range from around 200 Hz up to 200 MHz and provide continuous bunch intensity measurements in 25 ns intervals. Each sensor features an additional independent winding to inject calibration signals. Some fundamental shortcomings of the FBCTs, discussed in detail at the end of the chapter, led to development of new bunch intensity sensors, one of which is the subject of this dissertation.

2.3.3 Signal acquisition with analogue integrators

The FBCT produces a time-varying signal which is proportional to the instantaneous beam current within the device's bandwidth. To derive the bunch intensity, this signal must be integrated as explained in section 2.1.4. During the first years of LHC operation, this was achieved with analogue integrators designed by the LHCb collaboration for a system discriminating the kind of particle produced during a high-energy collision [38].

As bunch intensity measurements must be continuous, and analogue integrators require some dead time before taking new input, the FBCT front-end electronics uses two separate integrators interleaving between odd and even 25 ns bunch slots [39]. Unavoidable asymmetries of both integrators caused a clear discrepancy in measurements of bunches in consecutive slots [40]. Moreover, the effective integration window of each device was different but always shorter than the 25 ns required to capture all available data. To maximise the amount of signal visible to the integrators, the FBCTs had to be manually phased against the reference clock and recalibrated with the DCCTs. The very time-consuming nature of such a procedure had a negative impact on the LHC operation since during that period the accelerator could not serve its primary function of colliding high-energy beams.

Due to the lack of a DC component in the FBCT output, the signal baseline constantly drifts as explained in section 2.1.6. Two components are integrated simultaneously: the beam signal and a quasi-static offset. The latter must be compensated for to minimise the measurement error. The front-end electronics using analogue integrators measured the signal baseline in the abort gap, i.e. over a 3 µs period without any particles every 89 µs, and subtracted the measured value from the FBCT output as a static offset. However, even though the signal baseline is constant over each 25 ns bunch slot due to the 200 Hz low cut-off frequency of the FBCT, this is not true for the entire 89 µs window. By applying the same offset to each bunch, the algorithm could not reliably correct the data.

Even if the FBCTs were to be replaced by a more accurate sensor, the above issues with analogue integrators would continue to limit the LHC bunch intensity measurement system performance. Therefore, parallel to the development of a new beam sensor described in this thesis, another team worked on a separate project to upgrade the acquisition electronics.

2.3.4 Migration to digital signal acquisition

The thesis' author did not take an active part in the development presented in this section. However, this work had important implications on the thesis' results and is thus briefly discussed.

Recent progress in fast-sampling Analogue-to-Digial Converters (ADCs) has made them an interesting candidate for an upgraded LHC bunch intensity measurement acquisition system. Direct digital processing of FBCT signals would overcome the major limitations of analogue integrators at the cost of a large amount of data to be processed at high throughput. Studies confirmed that accurate LHC bunch intensity measurement are possible using a commercially-available module featuring a 14-bit ADC with the maximum sampling rate of 1.25 GSPS [41].

Some conditioning of the analogue signal produced by a bunch intensity sensor is necessary to increase the efficiency of an ADC-based acquisition system. Firstly, a low-pass filter should stretch the signal to fill up the available 25 ns window. However, it might be desirable to have a few baseline samples available at the end of the bunch slot and a pulse length of approximately 22 ns is a good compromise. Secondly, the signal produced by a nominal LHC bunch should cover around 80 % of the ADC input range. Dedicated analogue front-end electronics can satisfy both of these functions.

Once the ADC digitises the analogue signals, it becomes possible to exploit many digital signal processing techniques. Automatic data-driven detection of bunches can replace manual phasing against a reference clock. The signal baseline can be accurately corrected for each individual bunch. Moreover, since the ADC can continuously sample its input, any discrepancies between odd and even bunches disappear. Due to the clear advantages, soon after a prototype validation with beam, the digital signal acquisition system quickly replaced the analogue integrators for bunch intensity measurements in the LHC. This migration took place at the same time as the sensor development presented in this thesis.

2.3.5 Other instruments measuring bunch intensity in the LHC

Due to the FBCT limitations discovered in the first years of the LHC operation, physicists looked also at other sensors already installed in the accelerator. Although the instruments described below measure primarily other beam properties, it was possible to successfully exploit their inherent sensitivity to the bunch current.

Wall Current Monitor

Monitoring of the longitudinal distribution of electric charge within the LHC bunches is crucial for understanding how the beam evolves over time and how it reacts to changes in the accelerator configuration. Three WCMs installed on each LHC ring provide such measurements. The sensors display an excellent high-frequency performance and reproduce the instantaneous bunch current as accurately as possible [30].

A straight-forward way to exploit a WCM for bunch intensity measurements is to integrate its output signal. However, in the case of the LHC monitors, their low-cut off frequency of 80 kHz leads to non-negligible baseline drifts and, consequently, integration errors. In some cases such limited measurement accuracy could be acceptable and the LHC WCM signals are sufficient to analyse the relative differences in intensities of different bunches.

Experiment timing pick-up

To ensure a good quality of their data, the four large LHC experiments must be precisely synchronised with the clock signals used to accelerate the beam. Optical links deliver accurate timing pulses to each experiment but, due to phase drifts, the signal phase has to be independently established. This is achieved with a set of special BPMs referred to as the BPTXs [42]. Each side of each experiment hosts one such sensor to monitor the incoming beam. With a pair of BPTXs installed symmetrically around the collision point, the experiments can use their signals to correct the relative phase between the accelerator clock and the internal experiment timing.

The BPTX features four beam-coupling antennas producing signals which could be used to reconstruct the transverse beam position. Adding up these four signals together with an external power combiner generates a signal which is independent of the beam position but proportional to the instantaneous bunch current within the monitor's bandwidth as explained in section 2.2.4. Unfortunately, due to the low cut-off frequency of the BPTX in the order of 100 MHz, integration of this signal over a 25 ns window would yield 0 as it was proven in section 2.1.6. Nevertheless, assuming that each bunch has the same longitudinal charge distribution, the BPTX signal amplitude is proportional to the relative intensity of each bunch. The experiments have exploited this BPTX feature as an FBCT-independent way of measuring the LHC bunch intensity.

Longitudinal Density Monitor

Due to accelerator chain imperfections, the main bunches are often surrounded by much less intense packets of particles, often referred to as satellite and ghosts bunches, which are virtually undetectable for classical instruments. Nevertheless, with the high energy carried by each beam particle, even such low intensity bunches pose a significant risk to the accelerator components and machine safety considerations warrant their constant monitoring.

To fulfil this function, the LHC features the Longitudinal Density Monitor (LDM) capable of detecting single photons of synchrotron radiation produced when a high-energy beam follows a curved trajectory [43]. As the photon flux is directly proportional to the number of particles in motion, the LDM is an extremely sensitive bunch intensity monitor with a temporal resolution of 50 ps and dynamic range exceeding five orders of magnitude. However, to achieve such stellar performance, the LDM must acquire synchrotron radiation over several minutes. Since the LHC requires bunch intensity measurements at a much higher rate, the LDM cannot serve as the main bunch intensity monitor.

2.3.6 Motivation for development of a new monitor

The 2010 LHC commissioning revealed several issues limiting the performance of the DCCTs and FBCTs [17]. The former were erroneously sensitive to the filling pattern, i.e. which 25 ns slots contain bunches and which ones are empty, resulting in an inaccuracy of several percent. The underlying problem was solved already in 2011 [44] and the DCCTs have very reliably served as the reference DC beam current sensors ever since.

Significant imperfections of the FBCTs also became apparent. Most notably the sensors displayed an unwanted sensitivity to the transverse beam position and bunch length. In the former case, the bunch intensity reported by the monitor would change when the beam moved transversely inside the vacuum chamber even though the number of particles remained constant. The same behaviour occurred when bunches shortened or lengthened. Both effects yielded a measurement error up to a few percent exceeding the original specification of ±1 % [45]. In 2011 the FBCTs were equipped with analogue 70 MHz low-pass filters which decreased their sensitivity to the beam position and bunch length [46]. Nevertheless, the effects remained measurable and were deemed as a significant limitation of the monitor's performance.

Another problem arose due to the mismatch in the DCCT and FBCT measurements. In principle, provided that there are no unbunched particles, the sum of intensities of individual bunches measured by the FBCT should be equal to the DCCT data. Discrepancies of up to several percent were common and a detailed study attributed them to the aforementioned FBCT sensitivities to more than just the bunch intensity. The only identified solution was to periodically cross-calibrate the two sensors using the DCCT as a reference [47].

The above FBCT shortcomings were regarded as inherent to the monitor and impractical to effectively mitigate. Therefore, a competitive development of two alternative sensors started in 2013 with the goal of installing a prototype device in the LHC by early 2015. Bergoz Instrumentation, who supplied the original FBCT sensor, designed an ICT in collaboration with CERN [32]. As a fully in-house alternative, the author developed a new kind of bunch intensity sensor, the Wall Current Transformer (WCT) which is the subject of this thesis. The remaining thesis' chapters describe the sensor in great detail.

The thesis statement of this dissertation can hence be stated as:

It is possible to design an electromagnetic sensor based on observation of the image current induced on the vacuum chamber wall for continuous, precise, and non-intercepting measurements of the LHC bunch intensity within a 25 ns window. The developed sensor can be compatible with the mechanical and operational constraints imposed by the LHC environment. It can also generate adequate signals for front-end electronics based on analogue integrators as well as an upgraded digital sampling acquisition system.

Chapter 3

Wall Current Transformer for the LHC

The chapter opens with a brief specification drafted for the Wall Current Transformer (WCT). The proposed sensor's principle of operation is then derived from a detailed electrical model leading to a discussion of engineering choices made for the LHC sensor. Subsequently, the main aspects of the WCT's mechanical design are presented, in particular the monitor's compatibility with the LHC environment. The chapter concludes with an overview of the developed analogue front-end electronics which adapt the WCT's signals to the various signal acquisition systems.

3.1 Desired characteristics of the new monitor

To successfully replace the LHC FBCTs, any new bunch intensity monitor must address the shortcomings of the original detector. In particular, unwanted sensitivity to the transverse beam position and bunch length must be minimised. Moreover, a possibility of calibration independent of the DCCTs should be envisaged already at the design stage.

Given the short development and installation time available, any potential FBCT replacement should reuse as much of the existing infrastructure as possible. Specifically, the new detector should be mechanically compatible with the already installed vacuum chamber with its support and the dielectric insert. This imposes the envelope dimensions of:

- minimum internal diameter: 84 mm
- maximum external diameter: 300 mm
- minimum length: 40 mm
- maximum length: 290 mm

A detector which can be installed and removed from the beam pipe without venting the vacuum should be preferred. The non-cryogenic sections of the LHC vacuum chambers routinely undergo a so-called bakeout during which the beam pipe is heated to around 300 °C to improve the vacuum quality. The LHC equipment installed directly on the beam pipe must either sustain such high temperatures or be temporarily displaced whenever bakeout takes places. The LHC FBCTs sit on sliders which allow them to be manually moved over to a specially-designed water-cooling station. Should the new monitor not require in-situ cooling, the complex water supply circuit could be decommissioned.

The waveforms generated by the new monitor must be adapted to all signal acquisition systems used for bunch intensity measurements in the LHC. As discussed previously in section 2.3.4, the new detector development coincided with a migration from analogue-integrator-based electronics to modern fast-sampling ADCs. Both systems were foreseen to run in parallel until the digital system is demonstrated to outperform the analogue integrators. The amplitude and length of the new detector's output pulse must suit both systems. The analogue integrators input signal must be limited to ±1.2 V and should not be longer than approximately 22 ns whilst the ADC-based system acquires a samples every 1.54 ns and its input cannot exceed ±420 mV. Moreover, the new monitor's low cut-off frequency should be minimised to reduce the error due to signal baseline reconstruction, as explained in section 2.3.3.

Equations 2.39 and 2.32 impose the required cut-off frequencies of a bunch intensity monitor integrating signals within a 25 ns window. With the maximum permissible total measurement error of 0.1 % it seems justified to limit the inaccuracy of the the signal leaking outside of the integration window to not more than 0.01 % which gives the maximum low cut-off frequency and the minimum high-cut off frequency, respectively, as follows:

$$f_{\mathrm{L}} < 640\,\mathrm{Hz} \tag{3.1}$$

$$f_{\mathrm{H}} > 59\,\mathrm{MHz} \tag{3.2}$$

Finally, the detector's beam-coupling impedance, quantifying how much energy the beam loses due to the monitor's presence, should be minimised. Excessive impedance can not only locally increase the temperature above to monitor's damage level but also introduce instabilities to the beam motion. The two main strategies to achieve low beam-coupling impedance are avoiding any discontinuities on the beam-facing surface of the vacuum chamber, and minimising volumes which can be filled by the beam's electromagnetic field.

3.2 Principle of operation

Sections 2.2.2 and 2.2.3 demonstrated that both Wall Current Monitors (WCMs) and Beam Current Transformers (BCTs) present some attractive advantages as bunch intensity monitors. The former is well-suited to measure short pulses and senses the image current with small components installed outside of the vacuum chamber. The latter can be calibrated with a known current pulse and its low cut-off frequency can be reduced with high-permeability magnetic cores. The features of both monitor types can be combined to create a new detector, the Wall Current Transformer (WCT), which is the subject of this dissertation.

3.2.1 Overview

The WCT substitutes current-sensing resistors found in a typical WCM with small magnetic cores made of a high-permeability nanocrystalline material commonly used to produce large toroids for BCTs. The cores, mounted on a Printed Circuit Board (PCB), uniformly surround a dielectric insert embedded into the vacuum chamber. The image current, for which the insert presents a high-impedance gap, flows through conductive screws traversing the centre of each core. In such a configuration the cores form RF transformers with the screw being the primary winding and an additional thin wire wound to form the secondary winding. Moreover, a separate piece of wire acts as a calibration winding, much like in a typical BCT.

Figure 3.1 presents a simplified model of the WCT. Upon arriving at the dielectric insert, most of the image current flows through the conductive screws and couples to the small RF transformers. To avoid radiating the beam's electromagnetic field into the accelerator environment, the detector must be enclosed in a conductive housing which constitutes an image

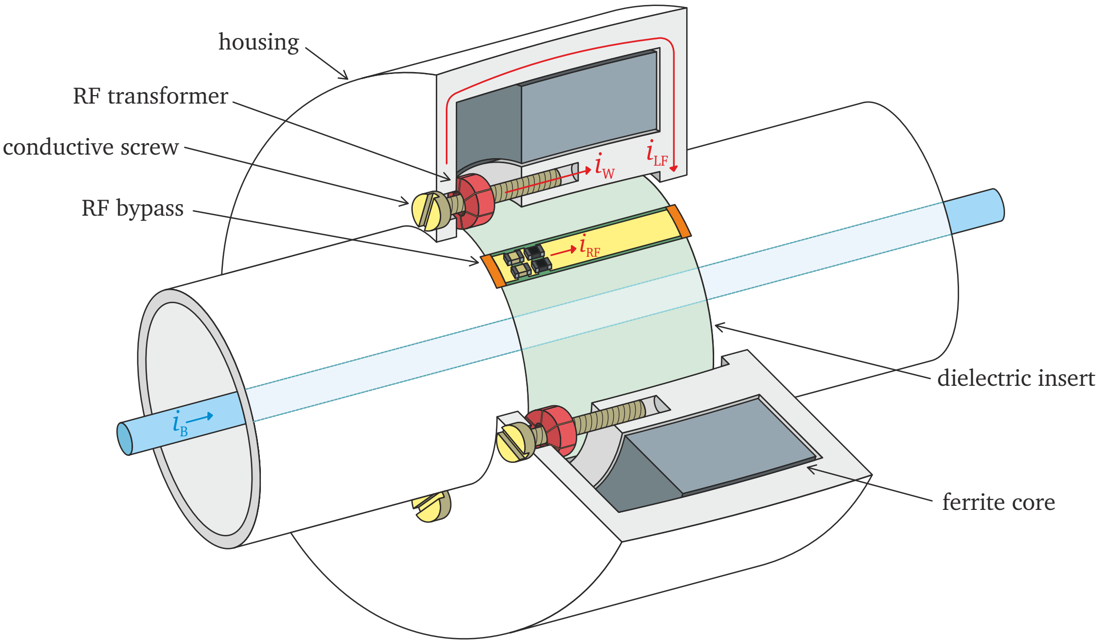

Figure 3.1: Principle of operation of the Wall Current Transformer.

current bypass at low frequencies. A high-permeability ferrite material fills the WCT's housing to increase its inductance and to effectively lower the frequency at which the image current flows predominantly through the screws. An RF bypass consisting of series capacitors and resistors connects both sides of the dielectric insert to control the high-frequency behaviour of the detector. A small part of the image current at high frequencies also "jumps" across the dielectric insert. Disregarding this path in analysis will not lead to a significant error as all bunch charge information is contained at much lower frequencies.

It is possible to analyse the WCT as an electric circuit following the model shown in Fig. 3.2. The beam current i_B induces an image current i_I of equal magnitude but opposite polarity. In the WCT, i_I splits into three parts:

- the low-frequency component i_{LF} flows through the housing with inductance L_{LF} the value of which depends primarily on the housing geometry and the ferrite permeability;
- the very-high-frequency component i_{RF} flows through the RF bypass with capacitance C_{RF}, resistance R_{RF} (both set with discrete components), and some parasitic inductance L_{RF};
- the intermediate-frequency component i_W flows through the screws with inductance L_W and resistance R_W the values of which depend mostly on the RF transformer configuration.

The last component induces a current i_{WCT} on the RF transformer's secondary winding with inductance L_{WCT} which results in a voltage v_{WCT} developing across the load resistor R_{WCT}. To allow high-frequency signal transmission without reflection, the WCT also features back-matching resistors R_{BM} which set the monitor's output impedance to 50 Ω. An acquisition system, schematically represented as a complex load Z_L, can then measure the WCT output signal.

Even though devices applying similar ideas were developed in the past [48, 49, 50], they were intended to measure the transverse beam position at relatively low frequencies. The WCT, on the other hand, is optimised for precise intensity measurements of short LHC bunches.

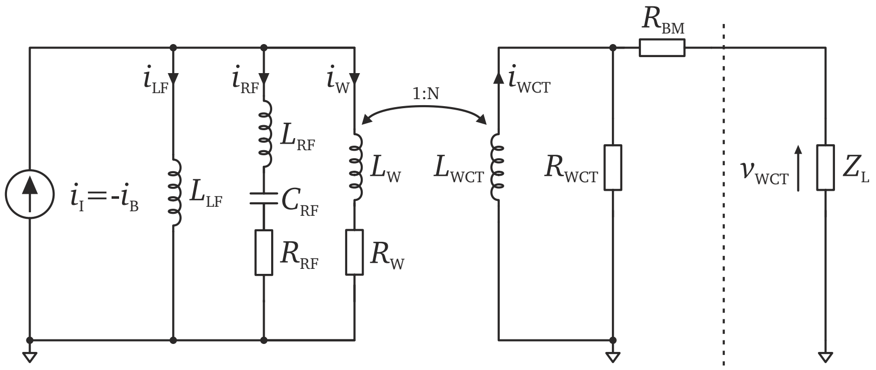

Figure 3.2: Electrical model of the WCT.

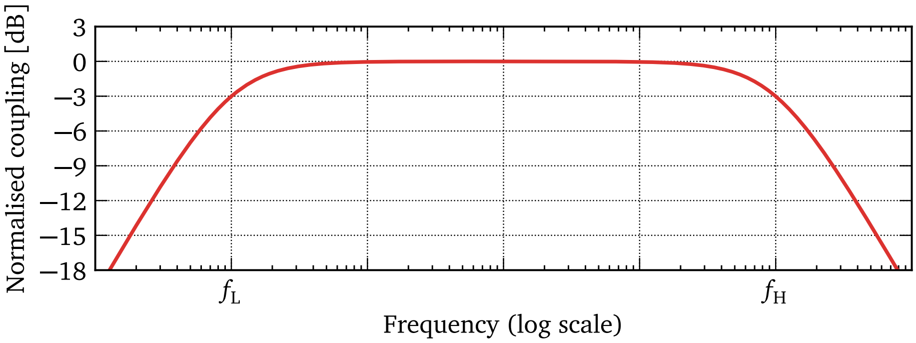

Figure 3.3: Frequency response of a generic bandpass system such as the WCT.

3.2.2 Detailed analysis

A time-varying current i_W flowing through one of the WCT conductive screws induces a magnetic field B_W in the core surrounding the screw [2, pp. 36.6–36.9]:

$$B_W = \mu_r \mu_0 \frac{1}{2\pi r} i_B \tag{3.3}$$

where μ_r and μ_0 are the permeabilities of the core and vacuum, and r is the core's mean radius. This field induces a current i_{WCT} in the N-turn secondary winding [2, pp. 36.6–36.9]:

$$i_{WCT} = \frac{1}{N} \frac{2\pi r B_W}{\mu_r \mu_0} = \frac{1}{N} i_W \tag{3.4}$$

The above generalisation is valid when the current i_W is low enough not to magnetically saturate the small RF core. The WCT achieves this by using nanocrystalline materials whose permeability tails off with increasing frequencies leading to extremely high saturation currents.

The WCT measures only the part of the image current which flows through the screws. It is therefore important to establish the frequency range for which one can assume that $i_w \approx i_I$. The electric model from Fig. 3.2 can serve to qualitatively analyse the monitor's low and high cut-off frequencies. As the WCT measures only the current flowing through its conductive screws, it is helpful to examine the primary side of the transformer, shown on the left hand side of Fig. 3.2, as a bandpass filter with its generalised bandwidth shown in Fig. 3.3.

Due to its capacitance C_{RF}, the RF bypass does not conduct current at low frequencies and only the housing with inductance L_{LF} presents an alternative current path. The only two possible paths for the low-frequency image current are the housing and the screws. Following the Fig. 3.2 model, their respective impedances are:

$$Z_{\mathrm{LF}} = 2\pi f\, L_{\mathrm{LF}} \tag{3.5}$$

$$Z_{\mathrm{W}} = \sqrt{R_{\mathrm{W}}^2 + (2\pi f\, L_{\mathrm{W}})^2} \tag{3.6}$$

Frequency f_{L}' at which $Z_{\mathrm{LF}} = Z_{\mathrm{W}}$ is the WCT primary-side low cut-off frequency:

$$f_{\mathrm{L}}' = \frac{R_{\mathrm{W}}}{2\pi\sqrt{L_{\mathrm{LF}}^2 - L_{\mathrm{W}}^2}} \tag{3.7}$$

In practice, L_{LF} is significantly higher than L_{W} due to the large dimensions of the housing which, in addition, is filled with high-permeability ferrite, further increasing its inductance. Hence, f_{L}' becomes simply:

$$f_{\mathrm{L}}' \approx \frac{R_{\mathrm{W}}}{2\pi L_{\mathrm{LF}}} \tag{3.8}$$

Besides the physical resistance of the screw itself, R_{W} also consists of the impedance transformed from the secondary side of the small RF transformer. The latter dominates the value of R_{W} in virtually all cases. As an example, a 10 mm-long copper screw of 4 mm diameter presents a resistance of only 13 µΩ.

It will be shown later that in the LHC WCT $R_{\mathrm{WCT}} \lll R_{\mathrm{BM}} + Z_{\mathrm{L}}$ resulting in R_{WCT} as an accurate approximation of the secondary-side resistance. Assuming that the RF transformers are lossless, this leads to a simple formula for the primary-side resistance [51, p. 1124]:

$$\boxed{R_{\mathrm{W}} \approx \frac{R_{\mathrm{WCT}}}{N^2}} \tag{3.9}$$

Combining eqs. 3.8 and 3.9 yields the WCT primary-side low cut-off frequency:

$$f_{\mathrm{L}}' \approx \frac{R_{\mathrm{WCT}}}{2\pi N^2 L_{\mathrm{LF}}} \tag{3.10}$$

Since only the DC component of the bunch current carries the information about its charge (see section 2.1.5), minimising the WCT low cut-off frequency reduces the measurement error. As it will be shown later, the WCT signal is approximately proportional to the value of R_{WCT}. Thus, the required sensitivity of the monitor dictates the minimum R_{WCT} value. The housing inductance L_{LF}, however, can be controlled over a few orders of magnitude.

Given the WCT geometry with the vacuum chamber and housing being concentric cylinders, inductance of a theoretical coaxial structure is a good approximation of L_{LF} [52]:

$$L_{\mathrm{LF}} \approx \frac{\mu_{\mathrm{r}}\mu_0}{2\pi} \ln\left(\frac{D_{\mathrm{LF}}}{d_{\mathrm{LF}}}\right) l_{\mathrm{LF}} \tag{3.11}$$

where μ_r is the relative permeability of the material filling the coaxial line, μ_0 is the vacuum permeability, D_LF and d_LF are the diameters of the outer and inner conductor, respectively, and l_LF is the structure's length. Although magnetic materials with very high permeabilities exist (e.g. iron-based nanocrystalline alloys reaching $\mu_\mathrm{r} > 10^5$), ferrites are a better choice for the WCT due to their good microwave radiation absorption up to several gigahertz which reduces any electromagnetic resonances induced in an otherwise hollow housing.

Also the secondary-side of the electric model from Fig. 3.2 forms a simple high-pass LR filter with the low cut-off frequency of:

$$f_\mathrm{L}'' = \frac{1}{2\pi L_\mathrm{WCT}} \frac{R_\mathrm{WCT}\,(R_\mathrm{BM}+Z_\mathrm{L})}{R_\mathrm{WCT}+R_\mathrm{BM}+Z_\mathrm{L}} \tag{3.12}$$

which for $R_\mathrm{WCT} \ll R_\mathrm{BM}+Z_\mathrm{L}$ reduces to:

$$f_\mathrm{L}'' = \frac{R_\mathrm{WCT}}{2\pi L_\mathrm{WCT}} \tag{3.13}$$

The inductance L_WCT is a manifestation of a wire wound around a toroidal core [53]:

$$L_\mathrm{WCT} = A_\mathrm{L} N^2 \tag{3.14}$$

where A_L is the single-turn inductance of a given small magnetic core. This parameter is set during the core's manufacturing process and is a function of the core's material and its geometry.

To assure that the WCT measures all current flowing through the screw, the secondary side low cut-off frequency must be much lower than that of the primary side $f_\mathrm{L}'' \ll f_\mathrm{L}'$:

$$\frac{R_\mathrm{WCT}}{2\pi L_\mathrm{WCT}} \ll \frac{R_\mathrm{W}}{2\pi L_\mathrm{LF}} \tag{3.15}$$

A simple condition arises from eqs. 3.9 and 3.14:

$$A_\mathrm{L} \gg L_\mathrm{LF} \tag{3.16}$$

As for some housing geometries this condition might be difficult to satisfy with the magnetic cores available on the market, let's consider a WCT with f_L' and f_L'' being of the same order of magnitude. The s-domain low-frequency transfer functions $H'(s)$ and $H''(s)$ of the primary and secondary sides, respectively, are simply those of a first-order high-pass filter [54]:

$$H'(s) = A' \frac{s}{2\pi f_\mathrm{L}' + s} \qquad H''(s) = A'' \frac{s}{2\pi f_\mathrm{L}'' + s} \tag{3.17}$$

With the primary side output being the secondary side input, multiplication of the two individual transfer functions results in the transfer function $H(s)$ of the whole system:

$$H(s) = H'(s)\,H''(s) = A'A'' \frac{s}{2\pi f_\mathrm{L}' + s} \frac{s}{2\pi f_\mathrm{L}'' + s} \tag{3.18}$$

The cut-off frequency f_L at which the system transmits half of the incident power can be found by solving a simple equation $H(2\pi f_\mathrm{L}) = 0.5$:

$$f_\mathrm{L} = \frac{1}{2}\left(f'_\mathrm{L} + f''_\mathrm{L} + \sqrt{(f'_\mathrm{L} + f''_\mathrm{L})^2 + 4f'_\mathrm{L}f''_\mathrm{L}}\right) \tag{3.19}$$

Omitting the term $4f'_\mathrm{L}f''_\mathrm{L}$ significantly simplifies the formula but leads to a maximum error of 21 % when $f'_\mathrm{L} = f''_\mathrm{L}$. As permeabilities of magnetic materials, which are necessary for calculating both cut-off frequencies, are typically specified with an uncertainty of around 20 % it seems acceptable to use a simplified formula:

$$f_\mathrm{L} \approx f'_\mathrm{L} + f''_\mathrm{L} \tag{3.20}$$

With eq. 3.10, 3.13, and 3.14, the WCT's low cut-off frequency becomes:

$$\boxed{f_\mathrm{L} \approx \frac{R_\mathrm{WCT}}{2\pi N^2}\left(\frac{1}{L_\mathrm{LF}} + \frac{1}{A_\mathrm{L}}\right)} \tag{3.21}$$

Determining the WCT's high cut-off frequency f_H is more complicated but possible with a few assumptions. On the primary side of the Fig. 3.2 circuit, one can ignore the housing which due to its large inductance constitutes an open circuit at high frequencies. Thus, f_H is the frequency at which the RF bypass impedance is equal to that of the screw:

$$\sqrt{R_\mathrm{RF}^2 + \left(2\pi f_\mathrm{H} L_\mathrm{RF} - \frac{1}{2\pi f_\mathrm{H} C_\mathrm{RF}}\right)^2} = \sqrt{R_\mathrm{W}^2 + (2\pi f_\mathrm{H} L_\mathrm{W})^2} \tag{3.22}$$

Even though it is possible to directly solve the above equation for f_H, the resulting formula is complicated and impractical. Taking into account the expected values of each component leads to a simpler approximate expression. The following paragraphs will prove that R_W is in the order of tens of milliohms which makes it insignificant compared to the screw's reactance at high frequencies. On the other hand, one can deliberately choose C_RF high enough to only be relevant at low frequencies where it is important to force as much of the image current as possible to flow through the screws. For relatively small values of the parasitic inductance L_RF, the WCT high cut-off frequency is then:

$$\boxed{f_\mathrm{H} \approx \frac{R_\mathrm{RF}}{2\pi\sqrt{L_\mathrm{W}^2 - L_\mathrm{RF}^2}}} \tag{3.23}$$

Minimising L_RF is critical and one must reduce the stray inductance of electrical contacts between the RF bypass and the rest of the monitor. Gaskets guaranteeing several points of large-area contact are commercially available and recommended for this purpose.

For frequencies higher than f_L and lower than f_H virtually all image current flows through the WCT screws yielding:

$$i_\mathrm{w} \approx i_\mathrm{I} \tag{3.24}$$

Applying the above to eq. 3.4 gives an elegant formula for the current induced on the secondary side of the RF transformer within the monitor's bandwidth:

$$i_{\mathrm{WCT}} = \frac{1}{N} i_{\mathrm{I}} \tag{3.25}$$

This current can be conveniently measured using the subsequent resistor network. The output voltage v_{WCT} with a purely resistive load impedance (a typical assumption for analysing RF measurement systems) is:

$$v_{\mathrm{WCT}} = \frac{R_{\mathrm{WCT}} Z_{\mathrm{L}}}{R_{\mathrm{WCT}} + R_{\mathrm{BM}} + Z_{\mathrm{L}}} i_{\mathrm{WCT}} \tag{3.26}$$

If the resistor values are such that $R_{\mathrm{WCT}} + R_{\mathrm{BM}} = Z_{\mathrm{L}}$, making the source and load impedances equal, the above equation simplifies to:

$$v_{\mathrm{WCT}} = \frac{1}{2} R_{\mathrm{WCT}} i_{\mathrm{WCT}} \tag{3.27}$$

Combining this result with eq. 3.25 gives the WCT output voltage:

$$\boxed{v_{\mathrm{WCT}} = \frac{R_{\mathrm{WCT}}}{2N} i_{\mathrm{I}} = Z_{\mathrm{WCT}} i_{\mathrm{I}}} \tag{3.28}$$

It is apparent that v_{WCT} is proportional to the beam image current. The proportionality factor Z_{WCT} is traditionally referred to as the transfer impedance and is helpful for comparing the WCT sensitivity with those of other bunch intensity monitors.

3.2.3 Using multiple RF transformers

The analysis has so far focused only on a theoretical WCT featuring a single RF transformer. Building such a monitor in real life might lead to several issues, e.g. an unwanted sensitivity to the transverse beam position, due to the inherent azimuthal asymmetry. A WCT with multiple RF transformers uniformly distributed around the vacuum chamber should be preferred instead. For the LHC monitor, eight cores provide a good compromise between the single-transformer azimuthal coverage of 45° and minimising the electric network required to combine the individual signals. Moreover, outputs of two adjacent cores can be summed up already on the internal WCT PCBs reducing the number of intermediate monitor's outputs to four.

Generally, either active or passive components can combine the four intermediate signals into a single WCT output. The former approach can increase the signal levels at the cost of introducing additional noise while the latter leads to some signal loss but relies on fewer components. The following three paragraphs quantitatively compare both methods and justify the choice made for the LHC WCT.

A 50 Ω resistor, traditionally used as the characteristic impedance in high-frequency circuits, generates thermal noise with spectral density of $1\,\mathrm{nV}/\sqrt{\mathrm{Hz}}$ at room temperature [51, p. 475]. In a 50 Ω-matched network, each resistive combiner input contributes noise equivalent to that of a 50 Ω resistor. As such noise is uncorrelated for the combiner's individual branches, the resulting spectral noise density increases by the square root of the number of the input signals. A passive four-way 50 Ω combiner needed for the LHC WCT contributes $2\,\mathrm{nV}/\sqrt{\mathrm{Hz}}$ of noise.

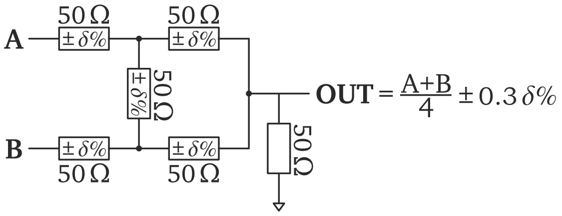

Figure 3.4: Model for analysing the WCT output error due to component tolerances.

On the other hand, a high-bandwidth current-feedback operational amplifier, e.g. Texas Instruments THS3201 [55], working in a non-inverting configuration exhibits a total input-referred noise spectral density of around $5\,\mathrm{nV}/\sqrt{\mathrm{Hz}}$ [51, p. 520]. Since this noise is uncorrelated for the four input stages needed to combine the LHC WCT intermediate outputs, an active signal combiner would introduce noise with spectral density in the order of $10\,\mathrm{nV}/\sqrt{\mathrm{Hz}}$.

The noise added by a passive combiner is about five times lower than that of an active circuit. However, due to the signal loss exhibited by the former, it is more accurate to compare Signal-to-Noise Ratios (SNRs). The output of an N-way resistive combiner is in practice the average of its inputs, i.e. each input is attenuated by a factor of N. A 4-way resistive combiner needed for the LHC WCT reduces the signal fourfold. Since the noise introduced by such a combiner is lower by roughly the same factor, both approaches result in similar SNR. With no obvious noise benefit either way, the LHC WCT uses passive combiners due to their simplicity.

The combiner's noise constrains the required WCT sensitivity. In a 550 MHz bandwidth of a typical LHC bunch a passive combiner introduces a noise of 47 µV. After digital 25 ns integration with an ADC sampling at 650 MHz and averaging for 1 s (i.e. over 11 thousand measurements) the effective noise becomes 111 nV. Since a 25 ns integral of a typical LHC bunch equals to approximately 3 % of the peak signal, to introduce an error of less than 0.01 % to the integrated signal of a pilot bunch with 1.28 A peak current, the WCT's transimpedance must at least:

$$Z_{\mathrm{wct}} \geq 111\,\mathrm{nV} \cdot 3\,\%^{-1} \cdot 0.01\,\%^{-1} \cdot 1.28\,\mathrm{A}^{-1} = 29\,\mathrm{m}\Omega \tag{3.29}$$

Beside noise, signal combiners can also be an error source due to components' inaccuracies. Figure 3.4 shows a simplified model of two WCT intermediate outputs combined using a 2-way resistive combiner used to study this effect. The first resistors in series with the inputs A and B represent the monitor's source impedance, followed by a classical delta combiner, with the last resistor being the load impedance over which the output signal is measured. Besides the load, each resistor was assigned a tolerance $\delta\%$. Simulations of ten thousand circuits, with the component values chosen at random within the allowed tolerance were then simulated, revealed that the output error was lower by a factor of around 3.3 than the tolerance $\delta\%$ assigned to the individual resistors. Since electronic component tolerances are typically specified as a power of ten, one can draw a simple rule of thumb: the WCT and combiner network resistor tolerance should be an order of magnitude lower than the required output signal accuracy.

Calculations of the effective values of some WCT components also must consider the number of RF transformers. Specifically, R_{WCT} (thus R_{W}), L_{WCT} (thus A_{L}), and L_{W} act as K components installed in parallel, where K is the number of RF transformers. One can obtain their effective values by scaling the values of components serving a single transformer by a factor of $\frac{1}{K}$.

3.2.4 Calibration input

Besides the multi-turn winding coupling to the beam-induced image current, the small RF cores can feature an additional winding for calibrating the monitor using an external signal. To mimic the WCT response to a particle beam, such a calibration winding should ideally consist of a single turn. Nevertheless, the parasitic capacitance between both windings is non-negligible and the calibration winding is most reliable at relatively low frequencies.

Calibration of bunch intensity monitors requires using a precisely known charge, voltage or current. As generating an accurate charge is challenging and voltage signals are prone to transmission losses, the WCT relies on current-based calibration. Due to the monitor's insensitivity to DC signals, the calibration current must be pulsed, with the pulse being long enough to safely disregard the extra intra-winding parasitic capacitance described in the previous paragraph. In practice, one can derive a reasonable duration of the calibration pulse from the WCT low cut-off frequency f_{L} defined in eq. 3.21:

$$T_{\mathrm{CAL}} = \frac{1}{2\pi f_{\mathrm{L}}} \tag{3.30}$$

Attaining a precisely calibrated monitor certainly requires correcting the apparent signal decay caused by the lack of DC response. This is simple to achieve with modern electronics using digitisers and by fitting the measured signal to exponential decay.

The monitor's single calibration input branches off into several windings with one installed on each RF core. The only way for the calibration signal to reach the circuit ground (i.e. to close the loop) is through one of the windings. In such configuration, the sum of currents in the individual calibration windings is equal to current injected into the WCT calibration input.

Since WCT calibration relies on only slow current pulses, the input resistance can be relatively low to minimise the power dissipated in the monitor. Practically, to equalise the currents sent to each core this resistance should be distributed among the individual windings. Unlike for the beam-sensing winding side, the values of the resistors used on the calibration side do not have to be neither precisely known nor the same for all resistors. Regardless of the resistor values, the total calibration current spreads among all the WCT cores. Any asymmetries in the calibration windings can be thought of as signals induced by an off-centred beam which the WCT can precisely measure by design.

Finally, lossy ferrite beads installed in series to the calibration winding can protect the pulsed current source from the high-amplitude signals that a passing beam would induce on the winding. At low frequencies (present in the calibration signals) such beads add only very little extra resistance, whereas at high frequencies (induced by the beam) correctly chosen beads can increase the winding impedance by several orders of magnitude effectively blocking all signal from being transmitted towards the electronics.

3.2.5 LHC WCT

With the values of almost all components presented in Fig 3.2 being virtually independent of the WCT mechanical design, it is possible to first consider the monitor as a pure electronic circuit and optimise its performance by applying classical circuit analysis techniques.

The number of screws, and consequently the RF transformers, used to construct the LHC WCT was one of the very first decisions taken during the design stage of the new monitor. Eight screws seemed to provide a good azimuthal coverage of the WCT vacuum chamber. An external circumference of 264 mm led to a distance between two adjacent screws in the order of 35 mm. Moreover, 8 being a power of 2 enabled a straightforward design of a signal combining network for the outputs of the individual transformers. With its direct impact on the measurement error as per eq. 3.1, optimisation of the monitor's low cut-off frequency was the next design step.

The mechanical design of the LHC WCT will be discussed in detail in the next section, however, the envelope dimensions bound by the existing LHC infrastructure (described in section 3.1) impacted the achievable low cut-off frequency. Specifically, a full control over the housing inductance L_{LF}, defined in eq. 3.11, was not possible by varying dimensions of the ferrite core since the values of D_{LF}, d_{LF}, and l_{LF} can change only over a small range. On the other hand, a magnetic material with a high relative permeability can lead to a large L_{LF}. For the LHC WCT, the choice fell on Ceramic Magnetics CMD5005 nickel-zinc ferrite cores with $\mu_{\mathrm{r}} = 2100$ up to 600 kHz [56]. Besides the high μ_{r}, this material also features a volume resistivity $\rho = 1 \times 10^{8}\,\Omega\,\mathrm{m}$ making it great at absorbing resonance which could be otherwise excited at high frequencies when $\mu_{\mathrm{r}} = 1$ and the housing becomes hollow for the electromagnetic field.

Given the bound housing dimensions, the largest ferrite core fitting into the LHC WCT is a 60 mm long toroid with inner and outer diameters of 117.2 mm and 176.8 mm. To make the monitor's assembly easier, the LHC WCT uses two cores of square 30 mm × 30 mm sections.

One can use eq. 3.11 to calculate the housing inductance L_{LF}. The aforementioned parameters of $\mu = 2100$, $D_{\mathrm{LF}} = 176.8\,\mathrm{mm}$, $d_{\mathrm{LF}} = 117.2\,\mathrm{mm}$, and $l_{\mathrm{LF}} = 60\,\mathrm{mm}$ give $L_{\mathrm{LF}} = 10.36\,\mu\mathrm{H}$. As the equation only coarsely approximates the WCT geometry as a coaxial structure, the author decided to nevertheless scrutinize the calculated value of L_{LF} with electromagnetic simulations.

Figure 3.5 shows the model used for simulating the housing inductance of a WCT filled with a ferrite material. The grey shell models the WCT housing and is made of a perfect electrical conductor. The orange and green rings are the ferrite cores. Both have identical parameters but are depicted in different colours for clarity. Eight blue arrows mark the position of discrete resistors replacing the conductive screws. To minimise the required simulation time, resistor values were set to 80 Ω, much higher than the real value of R_{W}. As all eight resistors are in parallel to each other, the effective simulated resistance is therefore $R_{\mathrm{W,sim}} = 10\,\Omega$.

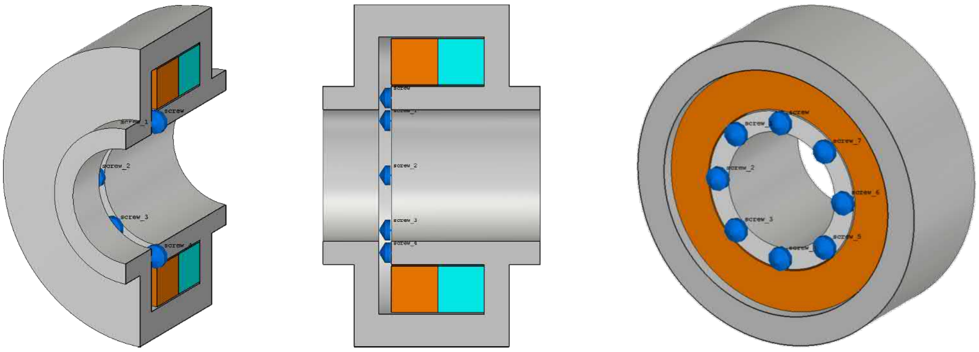

Figure 3.5: Electromagnetic model used for simulating ferrite-loaded housing inductance.

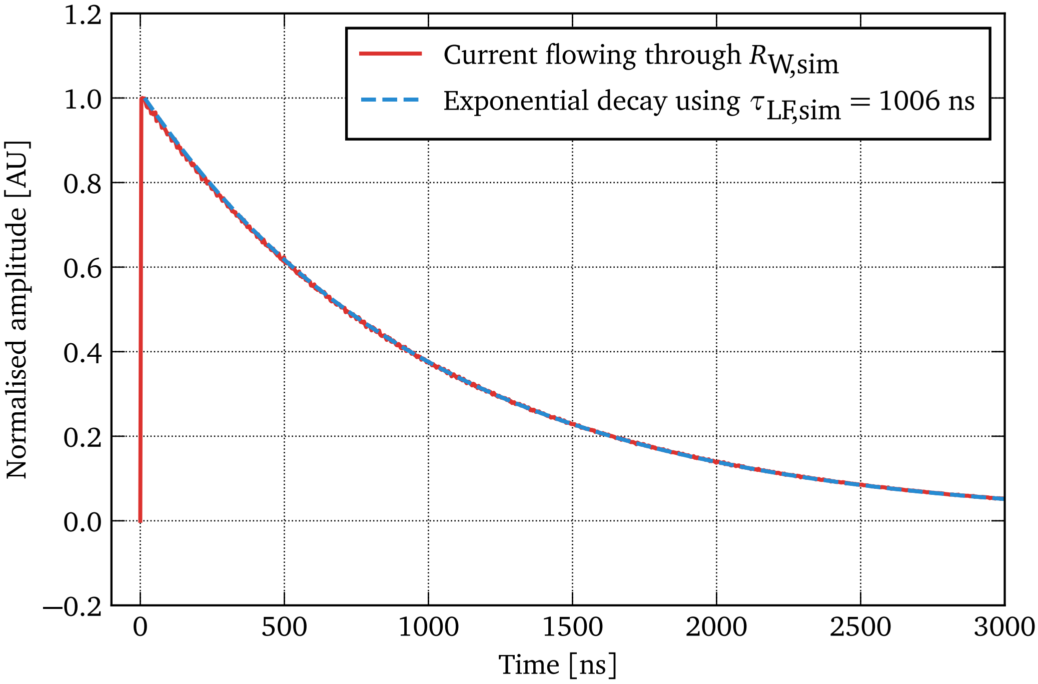

Figure 3.6: Current flowing through the $R_{W,sim}$ (representing the conductive screws) decaying exponentially due to the housing inductance.

Since the housing inductance is in parallel to the resistance $R_{W,sim}$, together they form a simple first-order low-pass filter. The current flowing through each of the eight resistors decays exponentially with a time constant given by [29, p. 112]:

$$\tau_{LF,sim} = \frac{L_{LF}}{R_{W,sim}} \tag{3.31}$$

To measure $\tau_{LF,sim}$, a long step-like current pulse was sent along the model's longitudinal axis. Figure 3.6 demonstrates the current flowing through $R_{W,sim}$ together with a fitted exponential function using $\tau_{LF,sim} = 1006\,\text{ns}$. The simulated response and the fitted function are identical and the obtained value of $\tau_{LF,sim}$ can be used to calculate the housing inductance L_{LF}:

$$L_{LF} = \tau_{LF,sim} R_{W,sim} = 10.06\,\mu\text{H} \tag{3.32}$$

Remarkably, the values of L_{LF} obtained analytically and through electromagnetic simulations are within 3 % of each other. As the uncertainty on the ferrite permeability is in the order of 10 %, the housing inductance can be rounded to $L_{LF} = 10\,\mu\text{H}$.

For the internal LHC WCT RF transformers, there were only a few magnetic cores with an appropriate size and high A_L available on the market. Finally, the choice fell on Vacuumschmelze T60006-L2009-W914 made of nanocrystaline iron-based VITROPERM 500 F material with a single-turn inductance of 25.5 µH at 10 kHz [57]. Eight transformers installed in parallel yield an effective $A_L = 3.2\,\mu\text{H}$. The cores, including their protective plastic casing, are supplied with the nominal dimensions of 5.1 mm (inner diameter) by 11.2 mm (outer diameter) by 5.8 mm (height). For the LHC WCT the author manually stripped each core of its casing to increase the available space for the current-carrying screws and to reduce the wire length required to make the necessary number of turns. The final obtained core dimensions were 6.5 mm (inner diameter) by 9.9 mm (outer diameter) by 4.8 mm (height).

Since the suppliers specify the ferrite permeability μ_r and single-turn inductance A_L with an uncertainty of 10 % to 20 %, it seemed justified to assume an additional engineering margin of 30 % on the maximum allowed low cut-off frequency defined in eq. 3.1, decreasing the target value to 450 Hz. To achieve this, eq. 3.21 dictates that $\frac{R_{WCT}}{N^2} < 6.84\,\mathrm{m\Omega}$. As such a small value of resistance might be difficult to implement, a large number of turns wound on the secondary side of the RF transformers N is desired. However, with the small core size installing more than 10 turns becomes impractical. Moreover, winding the wire tightly could lead to an increase in the undesired intra-turn parasitic capacitance limiting the WCT performance at high frequencies. Choosing the maximum practical value of $N = 10$ results in $R_{WCT} < 684\,\mathrm{m\Omega}$. As there are 8 parallel transformers , the resistance loading each of them cannot exceed 5.4 Ω. To satisfy this condition, the LHC WCT uses two parallel 10 Ω resistors installed on the secondary side of each RF transformer setting the values of $R_{WCT} = 625\,\mathrm{m\Omega}$ and $f_L = 410\,\mathrm{Hz}$.

Both N and R_{WCT} used in eq. 3.28 define the WCT output signal level. One must verify if the chosen values allow the sensor to achieve the desired sensitivity. The same equation gives a transimpedance $Z_{WCT} = 31.25\,\mathrm{m\Omega}$ meaning that before any signal conditioning the LHC WCT outputs 31.25 mV for each 1 A of bunch current it sees flowing through the conductive screws. With the typical LHC bunch parameters reported in Tab. 2.1, the sensor's output would peak at 40 mV for a low-intensity pilot bunch and at 960 mV for a high-intensity nominal bunch. Such signal levels are perfectly appropriate for typical front-end signal conditioning electronics, thus the values of N and R_{WCT} require no further adjustment.

To produce one common output, the signals picked up by the eight RF transformers must be summed up. As explained in section 3.2.3, this is done with a ladder of passive signal combiners. Firstly, the voltages of two adjacent transformers are averaged. A 95 Ω back-matching resistor follows the 5 Ω resistors loading the secondary winding of each transformer resulting in a source impedance of 100 Ω. Short 100 Ω transmission lines merge pairs of transformer outputs into four intermediate WCT output connectors which act as 50 Ω sources. Three external resistive signal combiners subsequently average these four signals producing a single common WCT output. To minimise any undesired transverse beam position sensitivity, the resistors used on the internal WCT PCBs were specified with a tolerance of 0.01 %.

Next to the signal winding, each RF transformer features an additional single-turn winding for calibrating the sensor. As explained in section 3.2.4, the WCT relies on calibration with long current pulses. The resistance loading the calibration winding cannot be excessive to minimise the dissipated power and to avoid any voltage-compliance issues in the calibration current source. The LHC WCT has a 10 Ω calibration input resistance to allow a 1 A current pulse without generating voltage of more than 10 V. This value has little influence on bunch current measurements and it can be freely optimised to match the output characteristics of any current source. Since the resistance is distributed among the eight RF transformers, each calibration winding connects to 33 Ω and 47 Ω series resistors to result in a total resistance of 10 Ω.

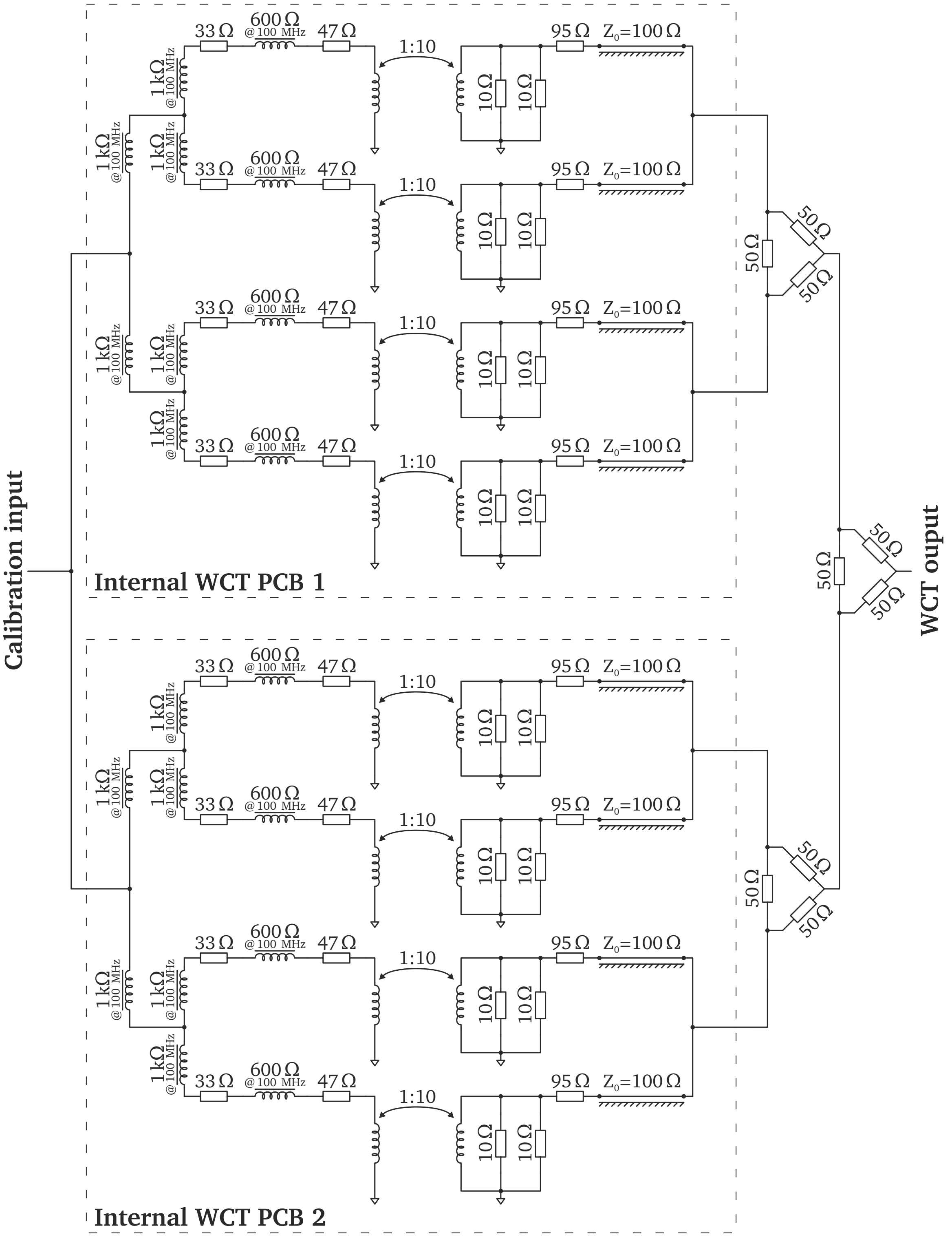

Figure 3.7: Schematic of the internal LHC WCT PCBs. The two calibration inputs are fed through a 0 Ω splitter. The four outputs are summed with a ladder of 50 Ω combiners.

Ferrite beads on the calibration-winding side increase the high-frequency impedance to avoid inducing any signals in the winding by the image current flowing through the conductive screws. The LHC WCT features two kinds of beads: Taiyo Yuden FBMH1608HM601-T and Murata BLM21AG102SN1D with 600 Ω and 1 kΩ resistance at 100 MHz, respectively. The beads' DC resistance is in the order of 0.25 Ω making them suitable for use with high current pulses.

Figure. 3.7 shows the resulting LHC WCT PCB schematics, with a detailed design and PCB layouts documented in [58]. The schematic does not depict the conductive screws constituting primary windings for bunch current measurements. Figures 3.8 and 3.9 present photographs of assembled PCBs and some details of RF transformers.

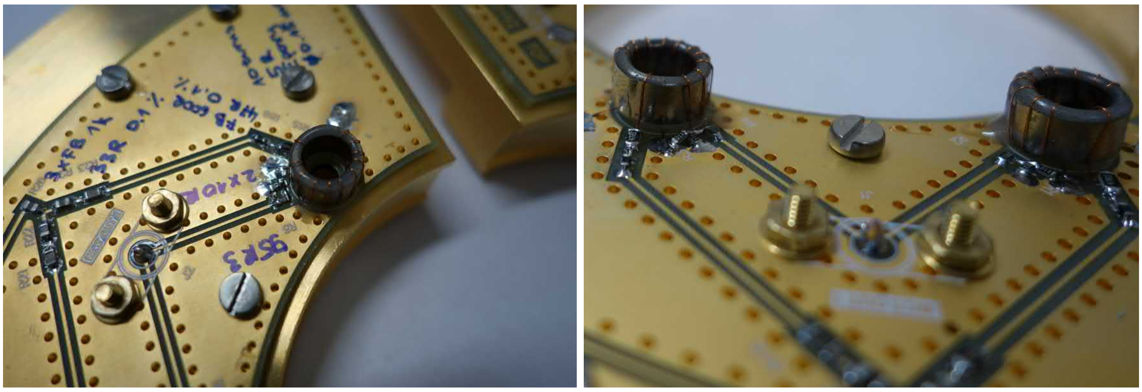

Figure 3.8: RF transformers installed on the internal WCT PCBs. For reference, the silver screw head seen between the cores is 5.5 mm across.

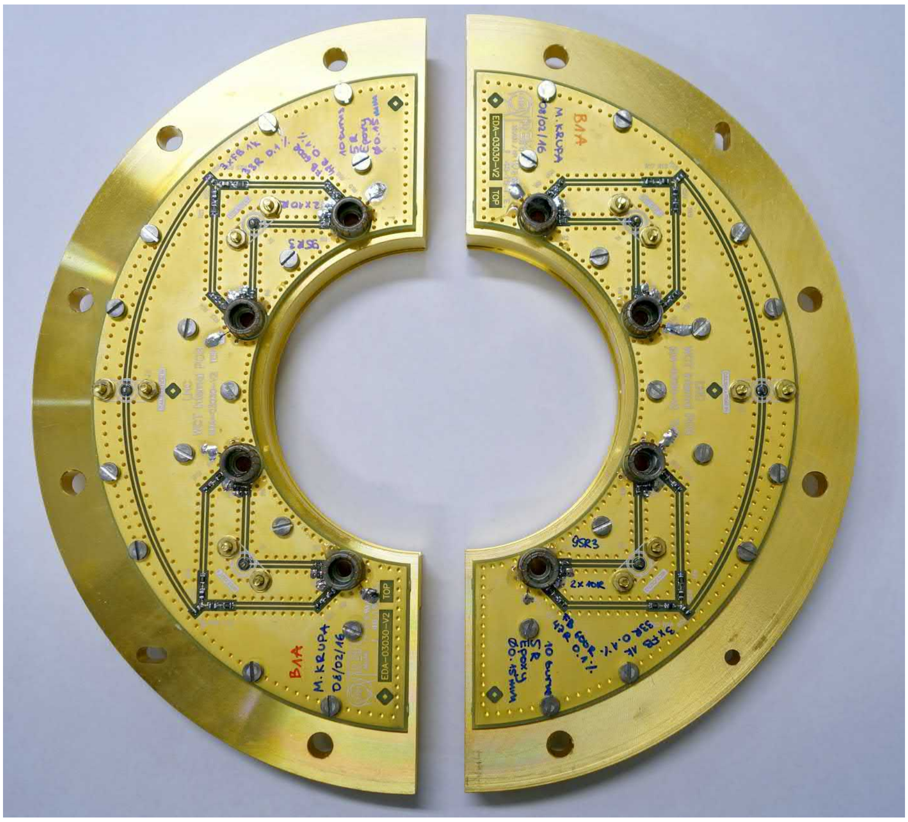

Figure 3.9: Internal WCT PCBs with four RF transformers each.

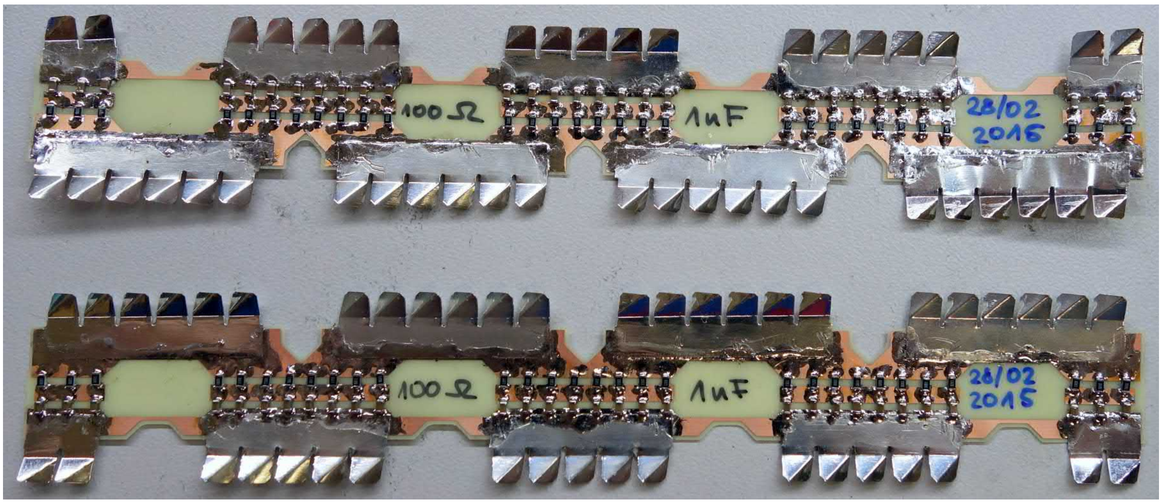

Figure 3.10: Two RF bypasses made of flexible PCBs.

To control its high-frequency behaviour, the LHC WCT uses an RF bypass consisting of series capacitors and resistors which is installed in parallel to the conductive screws. Two flexible PCBs, each covering approximately half of the vacuum chamber circumference, contain 60 parallel 100 Ω resistors installed in series with 60 parallel 1 nF capacitors as shown if Fig. 3.10. The effective values of the RF bypass components are therefore $R_{\mathrm{RF}} = 1.67\,\Omega$ and $C_{\mathrm{RF}} = 60\,\mathrm{nF}$.

The capacitance C_{RF} blocks any current flowing through the RF bypass at low frequencies forcing it to pass through the conductive screws instead. Its value is high enough for R_{RF}, forming a low-pass filter with the primary-side inductance L_{W}, to dominate the bypass impedance above 2 MHz. At high frequencies the relative permeability of the magnetic material making the small RF transformers decreases to unity. In such conditions, the screw's geometry solely determines the inductance L_{W}. Self-inductance of the exposed 8 mm part of each M4 screw, assuming a smooth solid cylinder, is approximately 2 nH [59]. Eight parallel screws result in $L_{\mathrm{W}} = 250\,\mathrm{pH}$. On the other hand, it is nearly impossible to accurately estimate the RF bypass parasitic inductance L_{RF}. For the LHC WCT, flexible gaskets with 36 large area contact points on either side of the bypass reduce L_{RF}. Assuming a very conservative 1 nH inductance per point of contact, one can estimate $L_{\mathrm{RF}} < 50\,\mathrm{pH}$.

With known values of R_{RF}, L_{W}, and L_{RF}, it becomes possible to calculate the high cut-off frequency of LHC WCT from eq. 3.23 as $f_{\mathrm{h}} = 1.1\,\mathrm{GHz}$ which is almost 20 times higher than the limit defined in eq. 3.2. This leaves a very comfortable margin to adjust the final signal bandwidth with external low-pass filters.

Table 3.1 summarises all electrical parameters of the LHC WCT. These values, together with the electrical model presented earlier in Fig. 3.2, can be used to conveniently study the WCT performance across a wide frequency range in any analogue circuit simulator such as SPICE. The methodology described in this section can also be applied to optimise the WCT to measure bunches of much different parameters than those present in the LHC.

Table 3.1: Electrical parameters of the designed LHC WCT. The effective values of A_L, R_{WCT}, and L_W are calculated as the discrete components' values scaled by the number of parallel RF transformers. The effective values of R_{RF} and C_{RF} are calculated as the discrete components' values scaled by the number of parallel RF bypass components.

Parameter	Symbol	Equation	Value
Number of RF transformers	K	-	8
Number of secondary winding turns	N	-	10
Single-turn inductance of RF transformers	A_L	$\frac{1}{K} \cdot 25.5\,\mu\text{H}$	$3.2\,\mu\text{H}$
Secondary-side resistance	R_{WCT}	$\frac{1}{K} \cdot 5\,\Omega$	$625\,\text{m}\Omega$
Secondary-side inductance	L_{WCT}	eq. 3.14	$320\,\mu\text{H}$
Primary-side inductance (low frequency)	L_W	A_L	$3.2\,\mu\text{H}$
Screw inductance (high frequency)	L_W	$\frac{1}{K} \cdot 2\,\text{nH}$	$250\,\text{pH}$
Primary-side resistance	R_W	eq. 3.9	$6.25\,\text{m}\Omega$
RF bypass resistance	R_{RF}	$\frac{1}{60} \cdot 100\,\Omega$	$1.67\,\Omega$
RF bypass capacitance	C_{RF}	$60 \cdot 1\,\text{nF}$	$60\,\text{nF}$
RF bypass inductance	L_{RF}	-	$< 50\,\text{pH}$
Housing inductance	L_{LF}	simulated	$10\,\mu\text{H}$
Low cut-off frequency	f_L	eq. 3.21	$410\,\text{Hz}$
High cut-off frequency	f_H	eq. 3.23	$1.1\,\text{GHz}$
Transimpedance	Z_{WCT}	eq. 3.28	$31.25\,\text{m}\Omega$

3.3 Mechanical design

There were two major constrains on the mechanical design of the LHC WCT. Firstly, the sensor had to be compatible with the existing vacuum chamber and dielectric insert at the location where the FBCTs had been originally installed. Secondly, the first WCT could be installed only if it did not require any section of the vacuum chamber to be even temporarily removed. Opening the LHC vacuum chambers requires lengthy pump-down and bake-out procedures which the LHC schedule could not be accommodate at the foreseen WCT installation window.

To meet the second objective, all cylindrical WCT parts which surround the vacuum chamber are cut in half along their longitudinal axis allowing the sensor to be assembled around the chamber. Such a design also presents another interesting advantage when the vacuum chambers are heated up to around 300 °C during the so-called bake-out procedure which improves the vacuum quality. Sensors such as the FBCT had to feature a complicated water-cooling circuit to protect the monitor from any heat-induced damage. The WCT, on the other hand, can be removed from the vacuum chamber and safely stored for the bake-out duration.

Detailed technical drawings of the LHC WCT mechanical assembly and all its parts are documented in [60]. Figure. 3.11 shows a 3D model of an assembled WCT. The sensors consists of the following parts, as indicated in the exploded view in Fig. 3.12:

- Eight conductive copper screws constituting a primary winding of the RF transformers.
- Two aluminium front brackets providing mechanical support to the other parts.
- Two copper front plates on which the internal PCBs are mounted.

- Four ferrite half-rings forming two full cores.
- Aluminium housing, split in two halves, creating a path for the low-frequency components of the image current.
- Two copper back plates with tapped holes to fix the eight conductive screws.
- Two aluminium back brackets providing mechanical support to the other parts.

All parts which carry the beam-induced image current within the WCT measurement bandwidth are made of oxygen-free copper which was additionally plated with a few micrometres of gold to prevent formation of a high-resistivity oxide layer. The components which are less critical for the sensor's electrical performance are made of standard-grade aluminium to reduce their weight and the cost of manufacturing.

Five Bal Seal BG15 M5 beryllium copper spring gaskets guarantee a good electrical contact between the vacuum chamber and the front and back plates. The gaskets, with a nominal thickness of 2 mm, compress during the monitor's assembly to tightly fill the 0.5 mm radial gap between the vacuum chamber the the WCT parts.

Besides the eight conductive screws, the other mechanical fasteners used to fix the WCT components to each other are standard off-the-shelf steel bolts and screws.

The ferrite cores diameters leave a 1.1 mm radial gap to the back plate and the housing. The bottom half of the housing and the top half the back plate feature two longitudinal pins which elevate the ferrite cores to be concentric with the vacuum chamber. Four springs attached to the top part of the housing fix the cores' position.

With all its cylindrical components cut in half, the WCT can be assembled around the LHC vacuum chamber in the following sequence with some crucial steps pictured in Fig. 3.13:

1. RF bypass made of flexible PCBs and five beryllium copper gaskets are fixed to the vacuum chamber on both sides of the dielectric insert (Fig. 3.13a).
2. Back plates and housing are installed downstream from the dielectric insert (Fig. 3.13b).
3. Space between the housing and the back plate is filled with the ferrite cores (Fig. 3.13c).
4. Front plates with the internal PCBs are mounted on the housing (Fig. 3.13d).
5. Conductive screws are inserted through the RF cores to connect the front and back plates.
6. Front and back plates are secured with the aluminium brackets.
7. External output signal combiners and calibration input splitters are installed (Fig. 3.13e).

With their low profile and widespread use in carrying electrical signals in the considered frequency range, standard panel-mount SMA connectors serve as an interface to the internal WCT PCBs. The connectors are also rated for carrying millisecond-long currents pulses with amplitudes in the order of a few amperes which are foreseen for calibrating the WCT.

Figure 3.14 presents technical drawings of the WCT cross-section as installed on the LHC vacuum chamber. Although the sensor can be installed in either orientation around the dielectric insert, the small RF transformers are wound such that a positively charged particle beam travelling from the front to the back plate results in a positive voltage at the monitor's output. Each WCT installed in the LHC features the transformers on its upstream side.

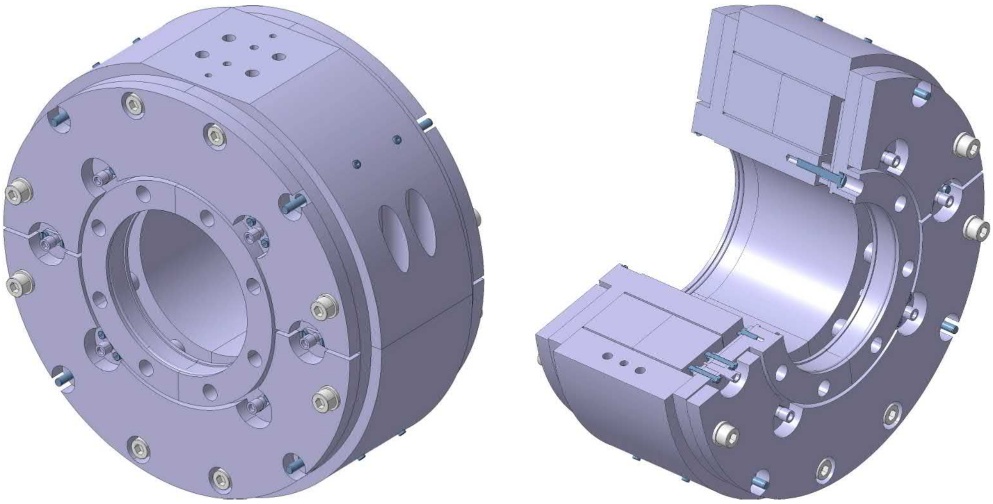

Figure 3.11: 3D model of an assembled WCT.

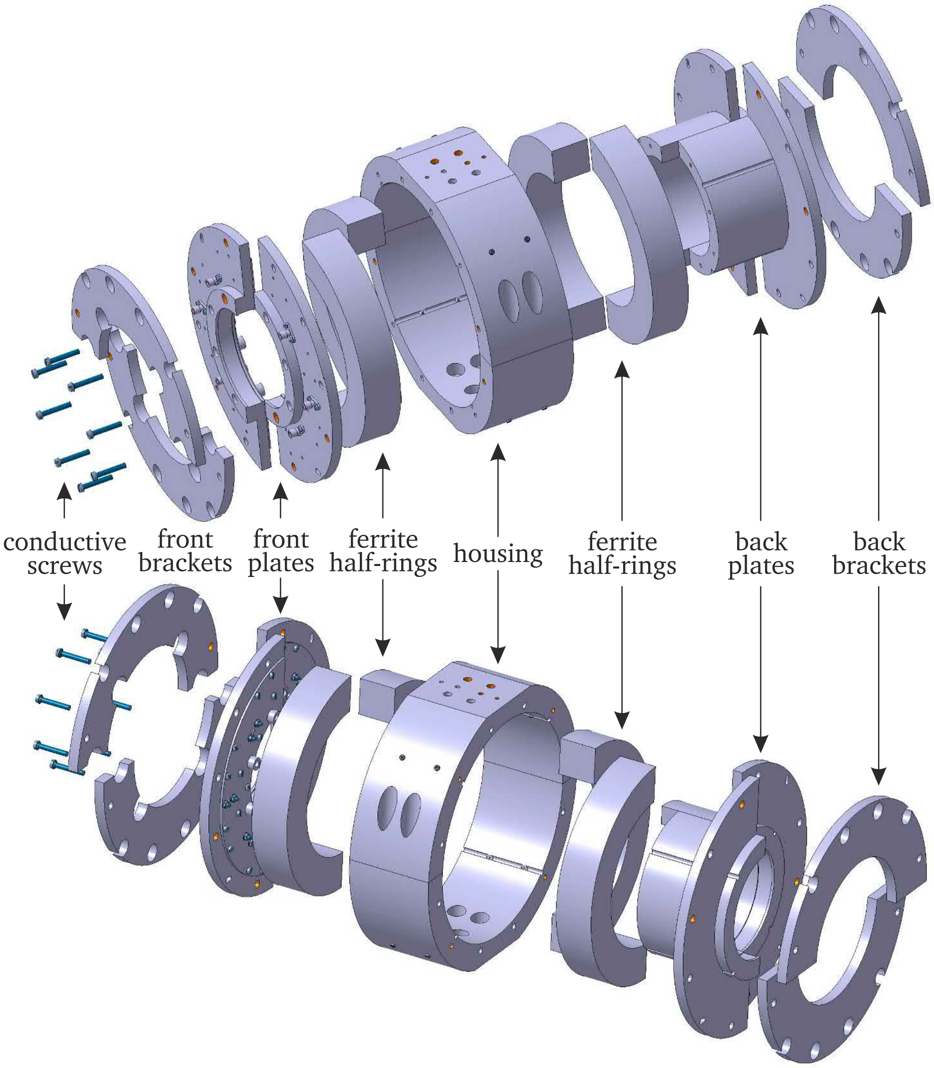

Figure 3.12: Exploded view of the WCT indicating its various subcomponents.

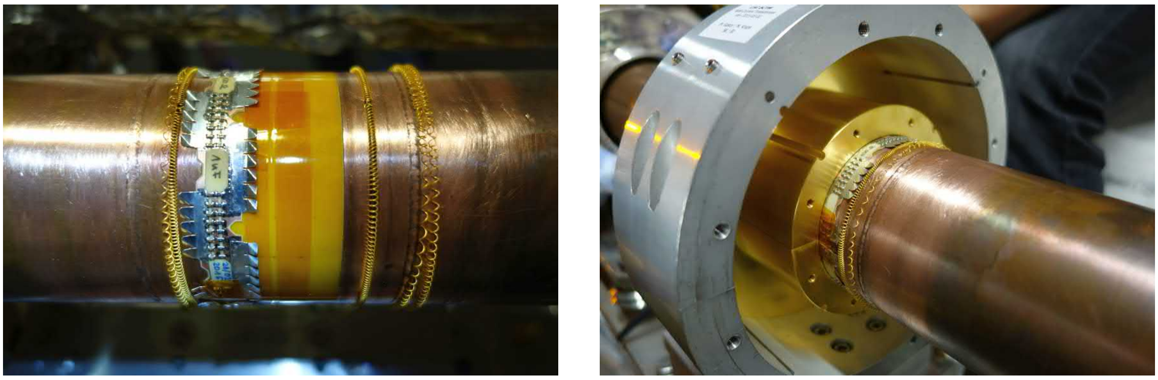

(a) RF bypass and gaskets. **(b)** Downstream part of the housing.

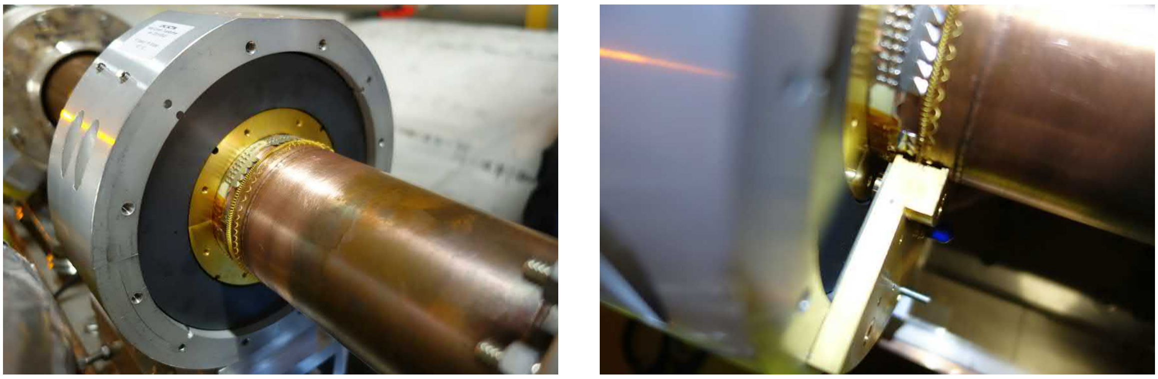

(c) Ferrite cores. **(d)** Bottom PCB.

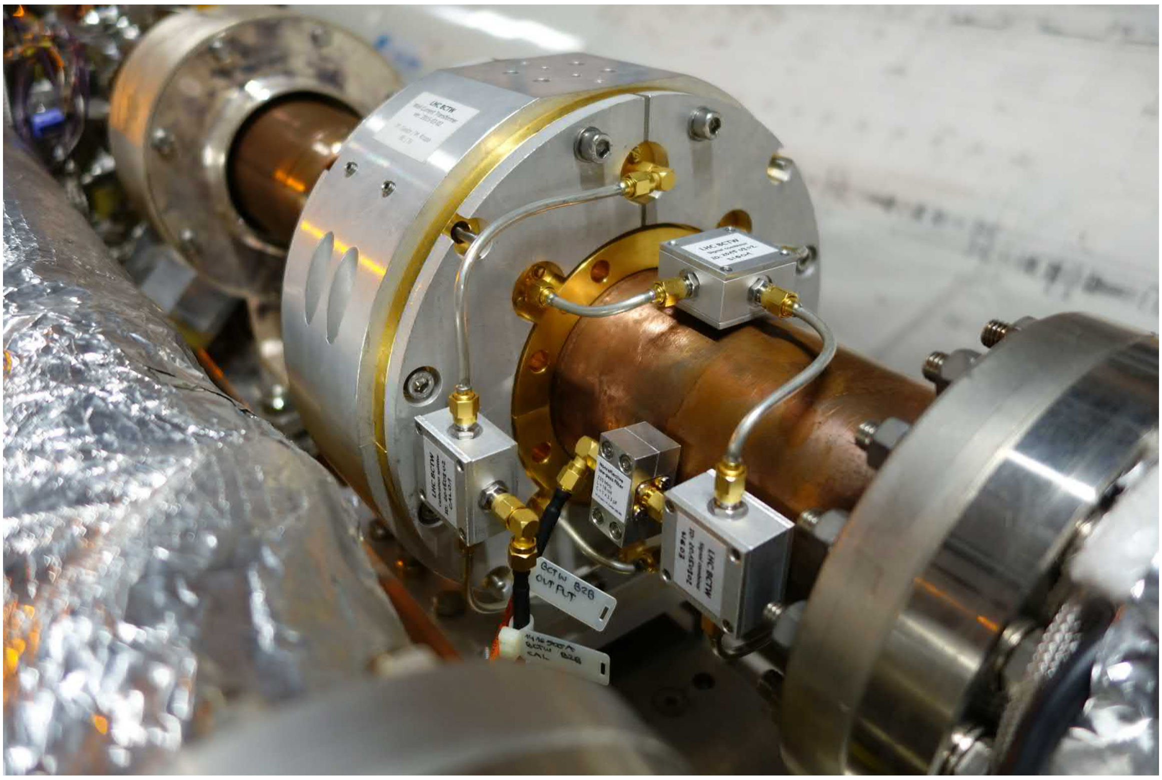

(e) Fully assembled WCT.

Figure 3.13: WCT assembly sequence on the LHC beam line.

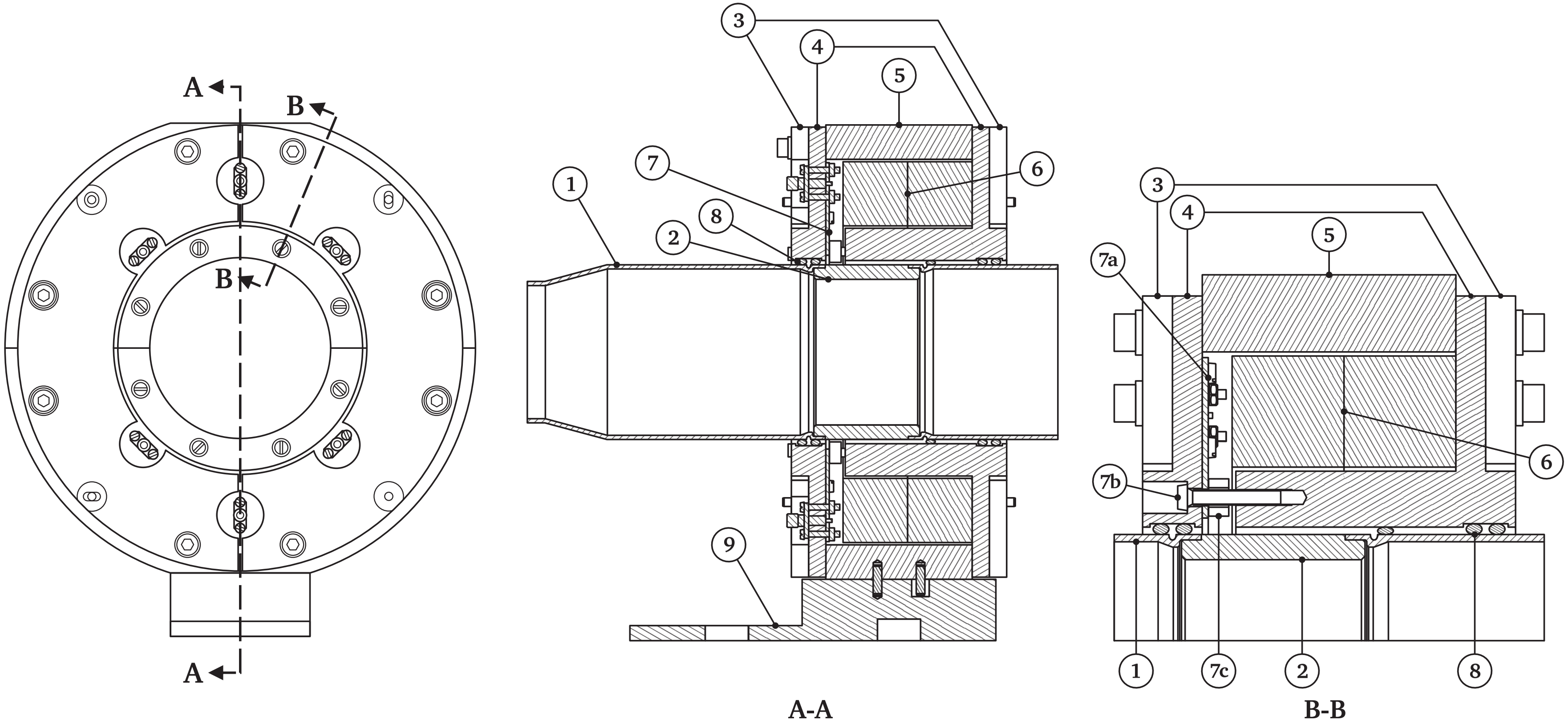

Figure 3.14: Cross-section of the WCT installed on the LHC vacuum chamber at the vertical plane (A-A) and at the plane of an RF transformer (B-B). 1 - LHC vacuum chamber; 2 - Ceramic insert; 3 - Aluminium brackets; 4 - Copper front-plate; 5 - Aluminium housing; 6 - Ferrite cores; 7 - PCB with RF transformers; 7a - PCB; 7b - Copper screw; 7c - RF transformer; 8 - Support.

3.4 Front-end electronics

Dedicated front-end electronics adapt the amplitude and length of the pulses at the output of the LHC WCT to optimally fit the input requirements of various signal acquisition electronics. With a pilot bunch being over 20 times less intense than a nominal bunch, the electronics features two independent sensitivity ranges for each of the installed monitors.

To avoid controlling the channel's sensitivity with switching circuits, the WCT's output feeds into two channels of different gains that drive two independent acquisition systems. Even though such a solution leads to some cost increase due to duplication of many components, it significantly reduces the operational complexity as it does not require any active gain switching. Software selects the most appropriate one of the two acquired signals.

Due to the presence of ionising radiation in the LHC tunnel, complex electronic circuits are, whenever possible, installed in radiation-shielded service galleries located some 10 m away from the beam line. Thus, relatively long coaxial cables connect the WCT to its acquisition systems.

As such cables can pick up interference polluting the beam-generated signal, amplifying the WCT output, as close to the sensor as possible, is crucial. A circuit designed for this purpose is the head amplifier which also divides the signal between two sensitivity ranges referred to as "low gain" (to measure high-intensity beams), and "high gain" (to measure low-intensity beams).

At the far end of the cable, the signals need to reach several different acquisition and monitoring systems. To minimise the number of long coaxial cables pulled between the head amplifier and the service gallery, another active electronic circuit, referred to as the distribution amplifier, produces multiple copies of each signal. Due to different input dynamic ranges of the various acquisition systems, discrete attenuators adapt the signal amplitude to its final value.

The WCT high cut-off frequency is in the order of 1 GHz, almost 20 times above the minimum value required to contain 99.99 % of the signal integral within a 25 ns window (see eq. 3.2). Low-pass filters can stretch the signal to improve the usage of the available time window. Both the head and distribution amplifiers filter their input signals but also additional external circuits adapt the signal length for each acquisition system.

With a relatively long distance between the LHC tunnel and service galleries, the electrical grounds at each location can inevitably be at slightly different potentials. Additionally, the long cables' grounding shield can create large-area loops with other grounded elements (such as racks, power cables etc.). Background magnetic field, commonly present in accelerator tunnels due to high-field magnets, can induce interference currents leading to generation of additional unwanted signals. One of the most effective ways of "splitting" such loops are common-mode chokes which pass only differential currents sent onto coaxial cables by the WCT and its front-end electronics while blocking any common-mode currents induced on the ground loops.

The WCT front-end electronics operate in an air-conditioned environment therefore they will not experience significant variations of neither temperature nor humidity over time-scales relevant for measurements. The WCT calibration input allows the entire electronics chain to be calibrated on-demand to minimise any errors caused by long-term drifts.

The following sections describe the WCT front-end electronics components – designed, built, and characterised by the author – and provide their most important performance characteristics.

3.4.1 Non-reflective low-pass filters

Rather than reflecting signals above the cut-off frequency back to the source, non-reflective low-pass filters internally dissipate the filtered power. Such a behaviour presents a major advantage for the WCT as no power returns to the sensor installed on the beam pipe where it could disturb the subsequent measurements or even interfere with the passing particle beam.

Non-reflective filters are also often referred to as constant-impedance filters since they look to the signal source like a wideband matched-impedance load. A figure of merit for such filters is their reflection coefficient or any other quantity which can be directly derived for it, e.g. Standing Wave Ratio (SWR) or input reflection scattering parameter S11.

The non-reflective low-pass filters developed for the WCT are based on a circuit known from literature [61] adapted to linearise its phase response for smoother time-domain signal stretching effect. Figure 3.15 shows the circuit topology. For a given high cut-off frequency f_H, the component values are:

$$\sqrt{\frac{L}{4C}} = 50\,\Omega \qquad\qquad f_\mathrm{H} = 0.04\sqrt{\frac{1}{LC}} \tag{3.33}$$

Doubling the capacitors leads to a convenient numerical relation of $L = 10^4 \cdot C$ which increases the probability of the required component values being available. Despite of the number of reactive components, the filter is of third order with a 60 dB per decade roll-off.

The LHC WCT required developing filters with five different cut-off frequencies, ranging from 80 MHz to 400 MHz. Figure 3.16 shows frequency-domain measurements of their transmission (S21) and reflection coefficient (S11). For reference, the same figure also includes reflection coefficient measurements of a commercially available 50 Ω RF load.

Reflection coefficient of all developed filters remains below −30 dB up to 1 GHz implying that only less than 0.1 % of the input power returns to the source regardless of the signal frequency. Such performance was completely satisfactory as typically filters are referred to as non-reflective once their out-of-band reflection coefficient does not exceed −20 dB.

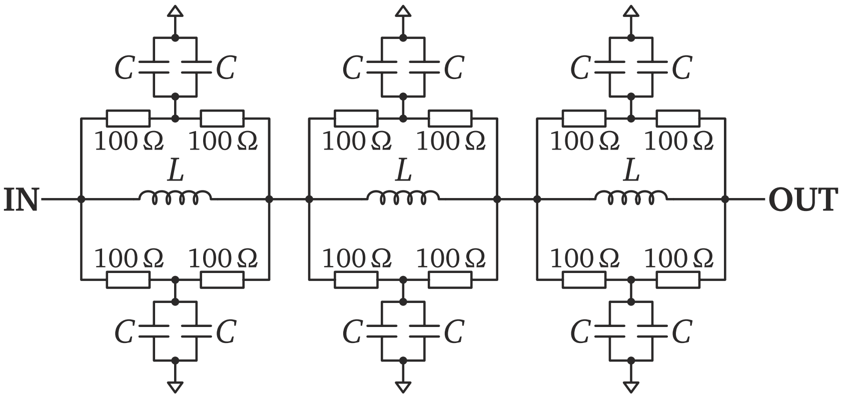

Figure 3.15: Generalised schematic of the developed non-reflective low-pass filters.

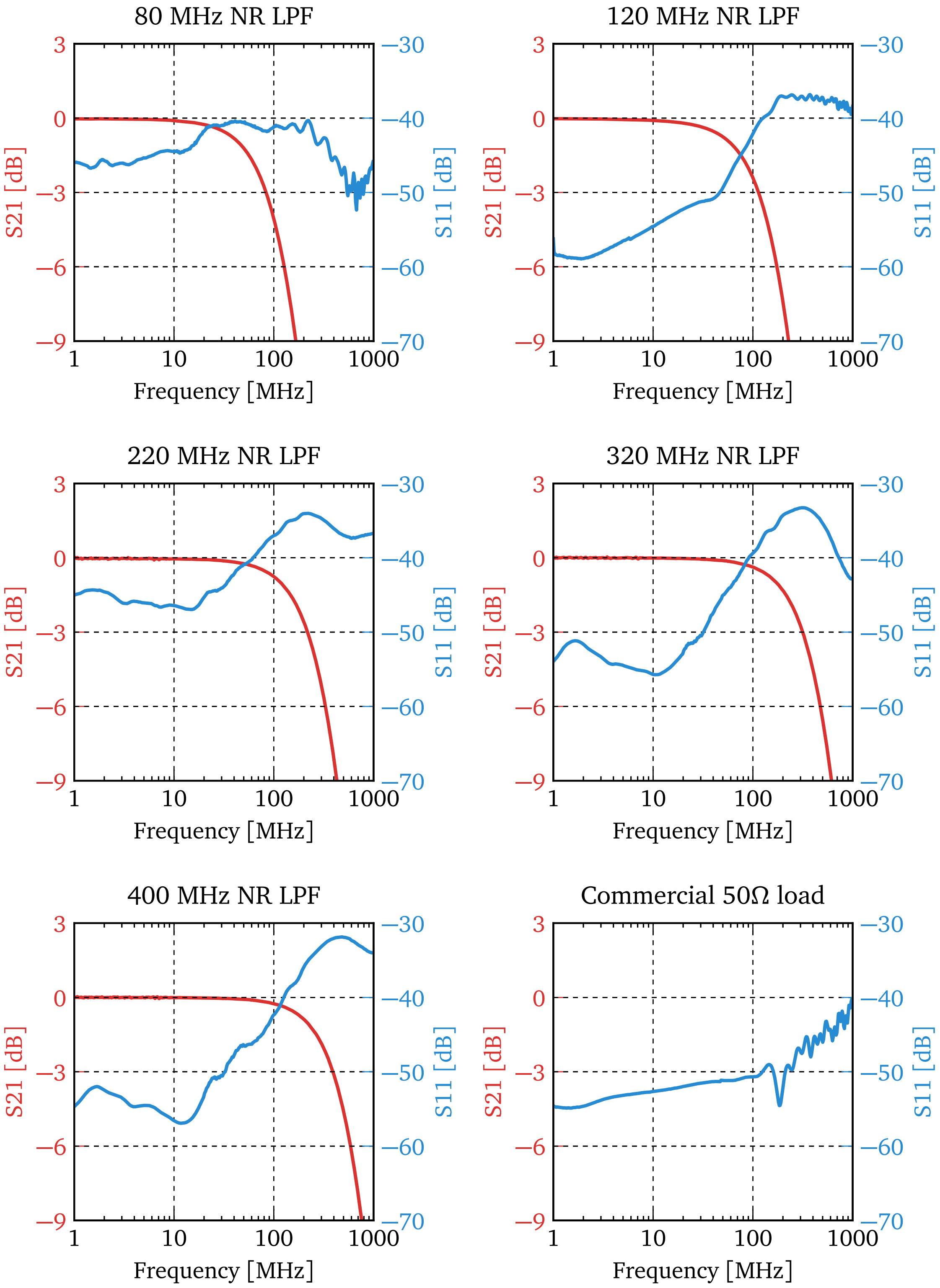

Figure 3.16: Scattering parameters of the different non-reflective low-pass filters developed for the WCT. For comparison, reflection coefficient of a commercial RF 50 Ω load is also plotted.

3.4.2 Head amplifier

Figure 3.17 shows a simplified circuit diagram of the developed head amplifier, while the detailed schematics and PCB layout are documented on CERN's Engineering Data Management Service [62]. A 400 MHz non-reflective low-pass filter, of the same topology as outlined in the preceding section, stretches the input signal. After the first common 12 dB gain stage, the signal splits between the "high gain" and "low gain" channels, the former boosting the signal by additional 20 dB. The last stage of each channel compensates the 6 dB voltage drop which would otherwise occur due to 50 Ω back-matching of each output. To block propagation of any DC offset, series 10 µF capacitors connect all stages. The circuit uses Texas Instruments THS 3201 which at the time of the LHC WCT development was the fastest low-distortion wideband current-feedback operational amplifier with 1.8 GHz unity-gain bandwidth, and 5 nV/$\sqrt{\text{Hz}}$ total input-referred noise spectral density for a non-inverting configuration [55].

Figure 3.19 demonstrates frequency domain measurements taken prior to the installation of the first head amplifier in the LHC tunnel. S21 curves show the transmission through each of the channels while S11 is the input reflection coefficient. The high cut-off frequencies of the "low" and "high gain" channels are 300 MHz and 200 MHz, respectively. The difference originates in a much higher gain of the latter which limits the operational amplifier's bandwidth.

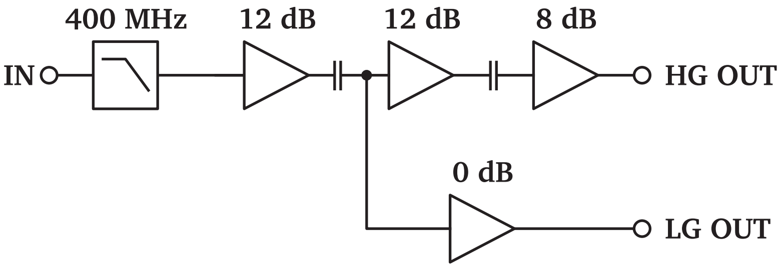

Figure 3.17: Diagram of the LHC WCT head amplifier.

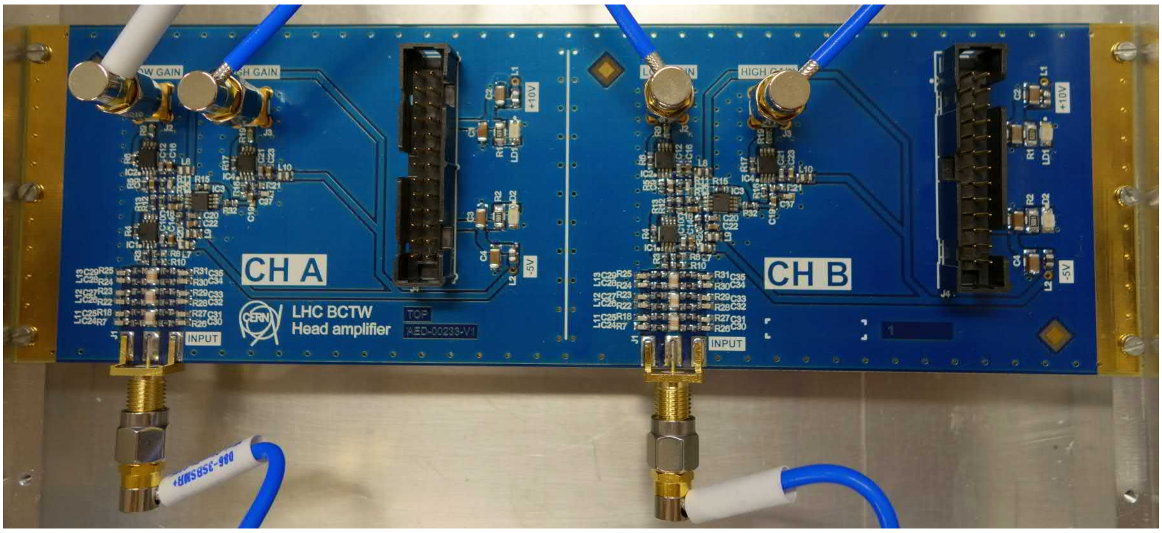

Figure 3.18: An assembled head amplifier PCB installed in an enclosure.

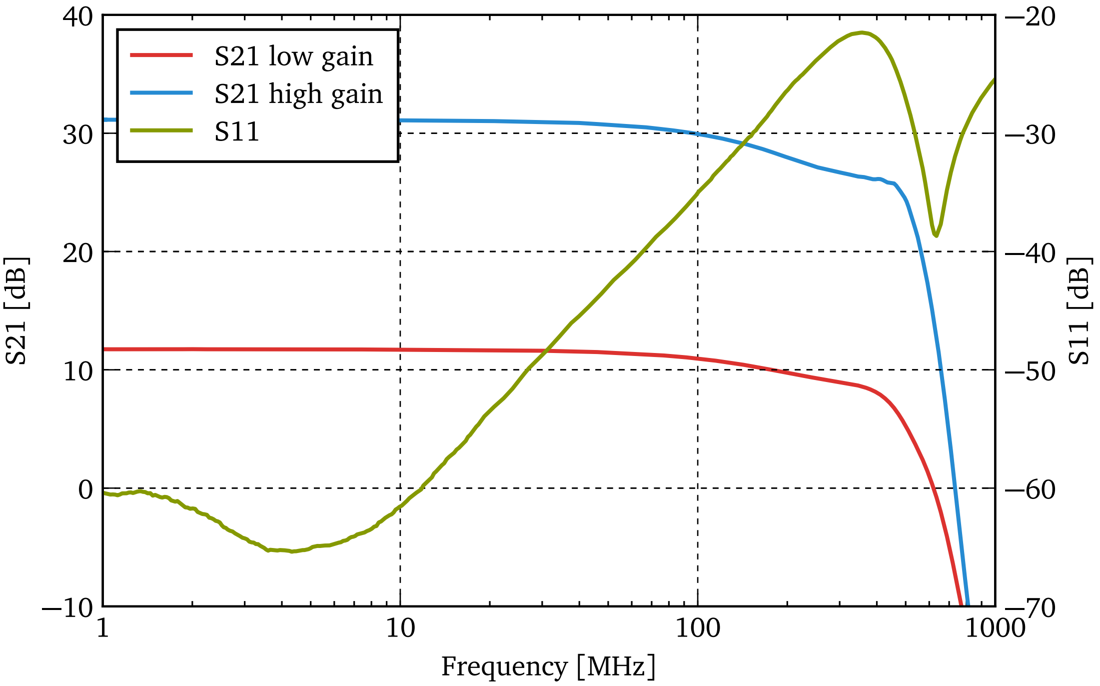

Figure 3.19: Scattering parameters of the head amplifier.

The amplifier's input is well matched to the 50 Ω characteristic impedance for high-frequency applications. Figure 3.19 confirms that the reflection coefficient S11 remains below −20 dB up to 1 GHz meaning that less than 1 % of incident power is reflected back to the source.

The output RMS noise in the "low" and "high gain" channels is 3.5 mV and 28 mV, respectively. With the transimpedance calculated in section 3.2.5, it is possible to simulate the head amplifier's output levels to typical LHC bunches. A pilot bunch of 5×10^9 particles results in 0.6 V peak voltage on the "high gain" output, while a nominal bunch of 1.2×10^{11} particles results in 1.4 V peak voltage on the "low gain" channel. For those typical bunches, the respective SNR is 26 dB and 52 dB.

3.4.3 Distribution amplifier

As for the head amplifier, full documentation of the distribution amplifier, including detailed schematics and PCB layout is available on CERN's Engineering Data Management Service [63]. Figure 3.20 shows a simplified diagram of the developed circuit. There is a 400 MHz non-reflective low-pass filter stretching the amplifier's input signal and a common 6 dB gain stage after which the signal splits into four branches to provide independent outputs for up to four acquisition systems.

During the distribution amplifier development phase the signal levels and bandwidth required by each of the acquisition systems were unknown. The circuit design enables its adjustment to boost the signal by at least an order of magnitude, if needed. Two gain stages precede each of the outputs, the second one of which compensates a 6 dB signal drop due to 50 Ω back-matching. Once the acquisition systems' requirement were specified, it became clear that a

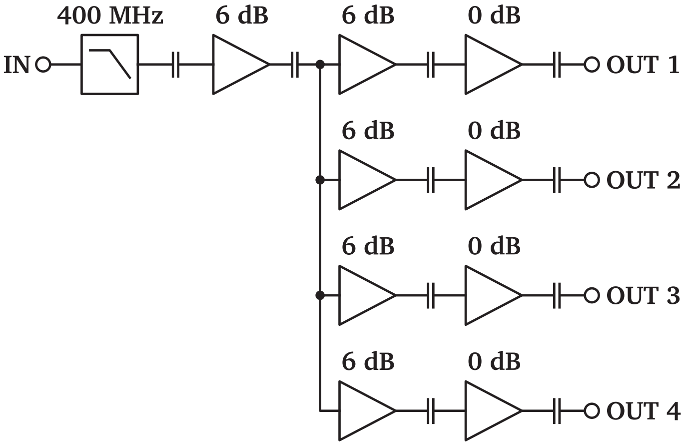

Figure 3.20: Diagram of the LHC WCT distribution amplifier.

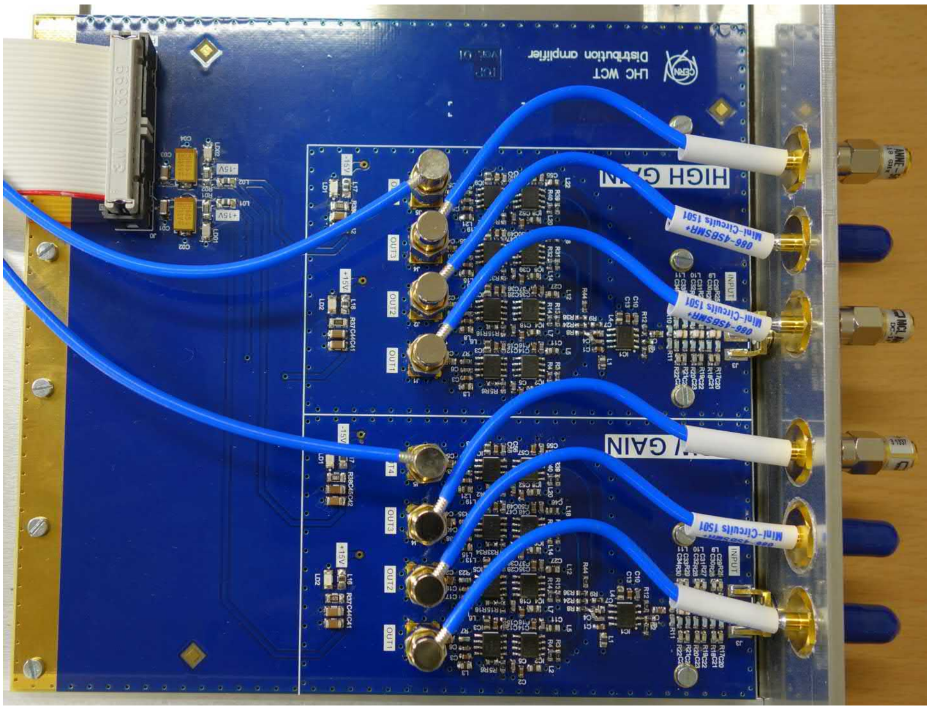

Figure 3.21: An assembled distribution amplifier PCB installed in an enclosure.

6 dB gain in the middle stage is sufficient for all foreseen users. Even though the last two gain stages for each output could be combined, the effort needed to redesign the circuit and produce new PCBs did not justify the potential benefits. Since the head amplifier dominates the total noise performance of the WCT front-end electronics, reducing the number of gain stages in the distribution amplifier would not significantly improve the system's SNR.

Figure 3.22 shows the distribution amplifier's frequency domain measurements in which S21 is the transmission through the amplifier while S11 is the input reflection coefficient. The circuit reaches a high cut-off frequency of 250 MHz and its input is well-matched up to 1 GHz with S11 remaining below −20 dB.

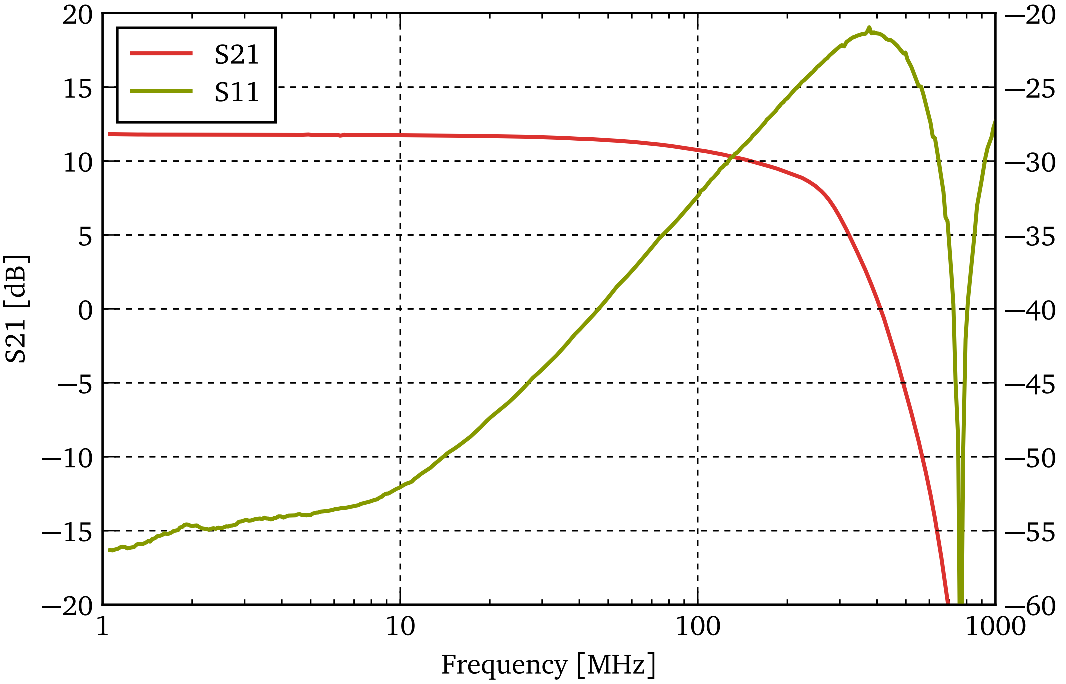

Figure 3.22: Scattering parameters of the distribution amplifier.

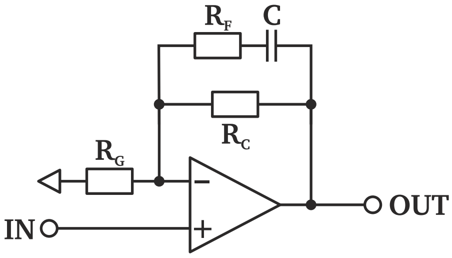

Figure 3.23: Low-cut frequency extension circuit.

An interesting feature implemented on selected outputs of the WCT distribution amplifier is a circuit extending the low-frequency performance of the monitor. Figure 3.23 shows the modification applied to the last gain stage, which is normally in a classical two-resistor non-inverting configuration.

The gain of such an amplifier is frequency-dependant:

$$G = 1 + \frac{R_C \parallel \sqrt{R_F^2 + \left(\frac{1}{2\pi f C}\right)^2}}{R_G} \tag{3.34}$$

For $R_F = R_G$ and $R_C \gg R_F$ the above equation simplifies at high frequencies, where the capacitor's impedance is close to 0:

$$G_{HF} \approx 1 + \frac{R_C}{R_C + R_G} \approx 2 \tag{3.35}$$

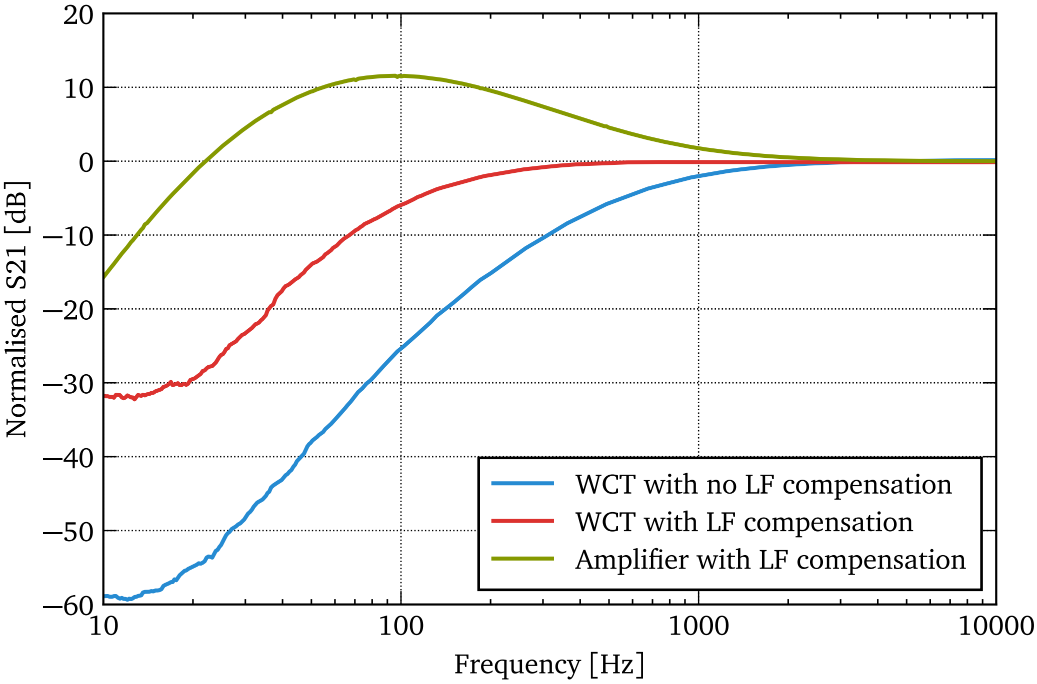

Figure 3.24: Compensation network improving the WCT low cut-off frequency.

Compensating the 3 dB signal drop at a low cut-off frequency f_l is possible by setting R_C and C such, that $G = 2 + (3\,\mathrm{dB}) = 2.83$ at f_l. Without any compensation, the low cut-off frequency of the WCT with its front-end electronics was measured at 780 Hz. The chosen compensation components values were $R_C = 11\,\mathrm{k\Omega}$ and $C = 133\,\mathrm{nF}$, maintaining the manufacturer's recommended $R_F = R_G = 820\,\Omega$ for the high frequency operation.

Figure 3.24 demonstrates the performance of the low-frequency compensation circuit. The blue curve shows frequency-domain measurements of the WCT and its front-end electronics in a channel with no additional modifications. The achieved low-cut off frequency is 780 Hz. The red curve, measured in a channel with the last stage of the distribution amplifier modified as in Fig. 3.23, decreases the low cut-off frequency to 140 Hz. The low-frequency boosting effect is apparent from the green curve taken with just the distribution amplifier's modified channel.

3.4.4 Common-mode suppression

The most prominent sources of electromagnetic interference in the proximity of the LHC WCT radiate power at frequencies below 1 kHz predominantly at multiples of the 50 Hz mains frequency. Interference signals picked up by long coaxial cables are typically of common-mode nature, i.e. the induced currents flow in the same direction in both the central conductor and in the outer shield. A convenient scheme to significantly suppress common-mode currents, especially at low and moderate frequencies, is winding the coaxial cable around a high-permeability magnetic core to form a common-mode choke [29, pp. 584–585].

Although soft ferrite cores are a typical candidate to build common-mode chokes, other magnetic materials can also be considered especially if the electromagnetic interference occurs pre-

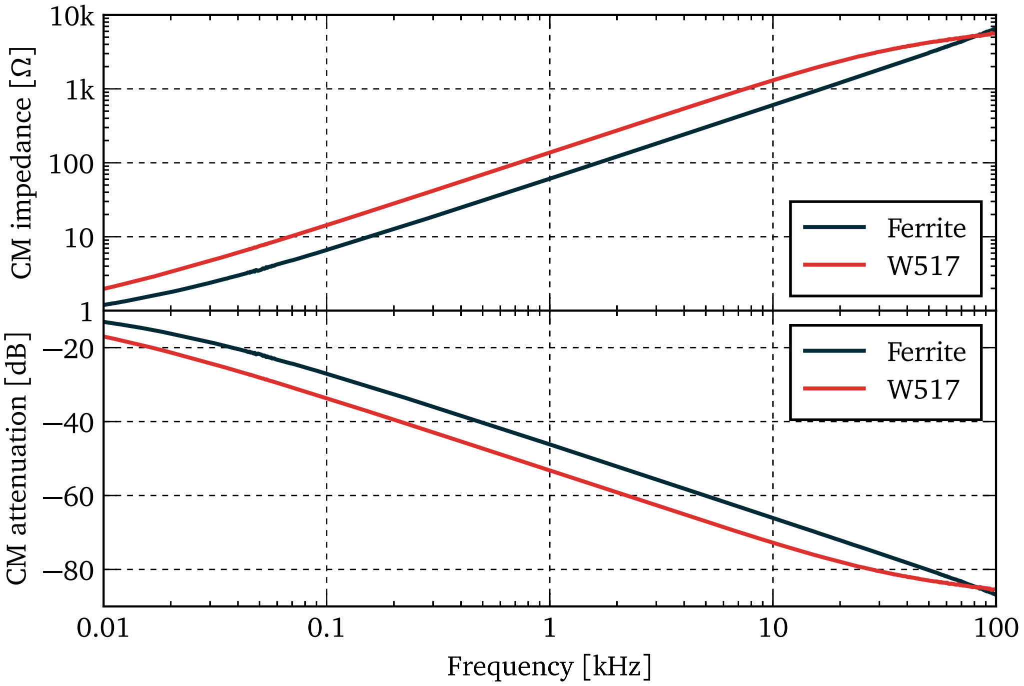

Figure 3.25: Common-mode suppression efficiency of the ferrite-based and nanocrystalline-based common-mode chokes.

Figure 3.26: Sixteen electrically-insulated common-mode chokes installed in a common enclosure to serve two WCTs.

dominantly at low frequencies. The LHC WCT common-mode chokes feature Vacuumschmelze T60006-L2063-W517 cores made of a nanocrystalline iron-based VITROPERM 500 F material with a nominal single-turn inductance of 59 µH at 10 kHz [64]. A 16-turn winding around the core results in a common-mode inductance of 15.1 mH which translates into over 4.7 Ω of impedance at 50 Hz.

The chosen core was compared to a common-mode choke made of a B64290L0040x830 core made by TDK out of N30 ferrite material [65], used at CERN for other beam instrumentation projects. With a single-turn inductance of 5.4 µH, less than 10 % of the nanocrystaline core's, the ferrite was wound with 40 turns of a thinner cable. As shown in Fig. 3.25, the choke developed for the WCT by the author attenuates common-mode signals about twice as much.

To minimise the number of components in the LHC tunnel, all chokes are located in the service gallery at each input and each output of the distribution amplifier resulting in 10 chokes needed per WCT. The two input chokes are installed just at the end of the long cables at the top of the rack, whereas the eight output chokes are installed in an electrically-insulated rack-mountable box which can fit up to 16 chokes serving two distribution amplifiers, as shown in Fig. 3.26.

3.4.5 Estimation of signal levels

With the WCT and its front-end electronics designed, one can estimate the signal levels reached with some typical LHC bunches. Table 2.1 served as a source for the investigated cases, however, with the information available in the previous sections it is possible estimate the signal for any arbitrary bunch intensity.

The peak current of a relativistic bunch with a gaussian longitudinal charge distribution is:

$$I_{\mathrm{peak}} = \frac{N_{\mathrm{b}}\, e}{\sigma_{\mathrm{b}}\, \sqrt{2\pi}} \tag{3.36}$$

where N_{b} is the number of particles forming the bunch, e is the elementary charge, and σ_{b} is the standard deviation of the gaussian distribution (quadruple of which is the bunch length).

Assuming sufficiently wide bandwidth of the WCT, the sensor's output amplitude is a product of the peak bunch current and the transimpedance:

$$V_{\mathrm{WCT,peak}} = Z_{\mathrm{WCT}}\, I_{\mathrm{peak}} \tag{3.37}$$

As all the existing and foreseen LHC bunch intensity acquisition systems provide measurements integrated over 25 ns, the WCT output bandwidth can be safely limited at 400 MHz with a discrete non-reflective low-pass filter. This processes stretches the signal in time and decreases its amplitude. Likewise, both amplifiers stretch the signal due to their limited bandwidth. Therefore, the front-end electronics signal levels cannot be easily computed using just the amplifiers' gains. Since analytical calculations of the signal shape after filtering is impractical, the author simulated the WCT front-end electronics chain using SPICE-based circuit solver.

Table 3.2 summarises the obtained results. It is worth to note that the system bandwidth decreases at each stage as the low cut-off frequencies of each system component accumulate. The total bandwidth of 70 MHz is nevertheless above the minimum limit of 59 MHz defined in eq. 3.2. Although the amplifiers' outputs saturate at around 3.8 V, the output signals are linearly proportional to the input only up to around 2.7 V. Beyond this value the gain suffers from compression and the signals becomes virtually unusable for precise measurements. The proposed solution is not immediately compatible with the high-intensity bunches foreseen for the future LHC physics programmes. This issue can be readily solved by adding a discrete attenuator before the distribution amplifier input while optimising the WCT performance for the beams used presently. Should the bunch intensity increase, the system will be adjusted through a quick manual intervention.

Table 3.2: Signal levels of the WCT and its front-end electronics with typical LHC bunches.

	Pilot	Nominal	Future	Ion
Bunch Intensity [charges]	5×10^9	1.2×10^{11}	2.2×10^{11}	5×10^9
Bunch Charge [nC]	0.8	19.23	35.25	0.8
Peak bunch current [A]	1.28	30.68	56.25	1.28
WCT output amplitude [mV]				
in 1.1 GHz BW	35	835	1531	35
in 400 MHz BW	23	553	1014	23
Head amplifier amplitude [mV]				
Low gain (in 220 MHz BW)	59	1423	2609	59
High gain (in 220 MHz BW)	594	saturated	saturated	594
Distribution amplifier amplitude [mV]				
Low gain (in 70 MHz BW)	81	1948	3572	81
High gain (in 70 MHz BW)	813	saturated	saturated	813

Chapter 4

Achieved results

The chapter presents the steps taken to demonstrate that the Wall Current Transformer described in the preceding chapter fulfils the requirements to become a bunch intensity monitor for the LHC. First, the laboratory measurements taken before any hardware was put in the accelerator tunnel are discussed. Next, an overview of the system installed in the LHC together with the installation timeline is given. Finally, the data taken with a particle beam during commissioning, dedicated study periods, and regular operation are analysed in detail.

4.1 Laboratory measurements

4.1.1 Laboratory coaxial setup

The author carried out the laboratory measurements described in the following sections using mostly a spare LHC vacuum chamber, including the ceramic insert, which had been adapted beforehand to serve as a laboratory 50 Ω coaxial line up to a few gigahertz [66]. The chamber was fitted with an inner conductor of an appropriate diameter and its end-flanges were coupled to N-type coaxial connectors with smooth conical transitions filled with Teflon [67]. Figure 4.1 shows an outline cross-section of the setup with the WCT (in green), the ceramic insert brazed to the vacuum chamber (in orange), the inner conductor (in blue), the and conical transition (in grey) filled with Teflon (in red).

Even though a large coaxial line excited by a voltage source is not exactly equivalent to a particle beam travelling in a vacuum chamber, the setup proved to be invaluable for laboratory evaluation and troubleshooting of the WCT. The problems related to impedance mismatch due to the varying geometry and connectors were relatively straight-forward to understand and correct for. Nevertheless, the measurements taken with the coaxial setup could be considered as only preliminary until repeated with a particle beam.

The coaxial setup served to characterise the WCT (and in part also the FBCT and ICT) in both the frequency and time domains. For the former, the key instrument was a broadband

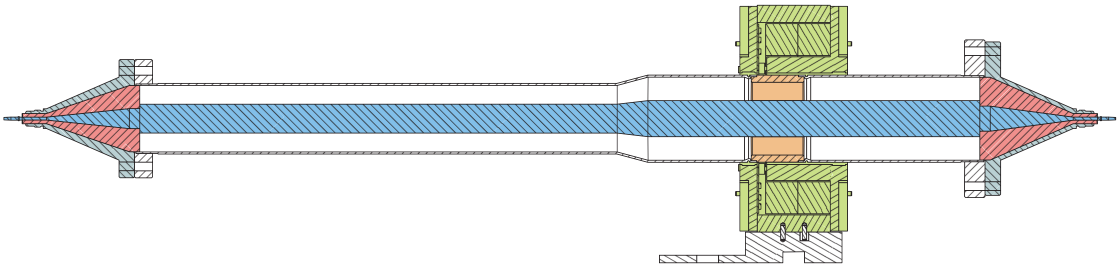

Figure 4.1: Cross-section of the coaxial setup used for WCT laboratory tests.

vector network analyzer. In the time domain, some measurements called for using a rather long step-like signals, whereas some other measurements required custom-built avalanche generators generating short impulses imitating the beam [68]. These generators provided the most beam-like pulses and were fundamental for characterizing the sensor.

4.1.2 Fast impulse response

One of the most important laboratory tests for any sensor is measuring its response to an excitation signal which is as close as possible to the real-life observable. In case of beam instrumentation, this is very often complicated, if not impossible, as realistically looking beam-like signals are extremely difficult to produce without using an actual accelerator. However, typically some approximations and engineering assumptions can be made during laboratory measurements.

A nominal LHC bunch has a peak current of some 30 A and FWHM of about 1 ns. An accurate representation of this pulse in a 50 Ω system would require generation of a 1.5 kV impulse with a sub-nanosecond rise time. This would be of course impractical. Instead, for the following measurements the beam was substituted with a 2 ns 20 V impulse sent into the coaxial setup and used as an excitation signal for the WCT, FBCT and ICT.

A 12-bit oscilloscope with 1 GHz analogue bandwidth acquired the signals of interest. Although its nominal sampling rate is limited to 2.5 GSa/s, for periodic signals it can be increased up to 125 GSa/s using the Random Interleaved Sampling (RIS) technique [69].

For the sake of readability, the author normalised the data shown in this section's plots such that for each signal its baseline is equal to 0 and its positive maximum is equal to 1.

Figure 4.2 presents the measurements of the fast impulse response of the WCT in two configurations. The curve referred to as "Full BW" shows the sensor's output digitised directly by the oscilloscope. The other curve demonstrates the effect of a 400 MHz non-reflective third-order low-pass filter (LPF) applied to the WCT output.

The full bandwidth response of the WCT closely follows the excitation pulse for approximately 2 ns. After that, the WCT signals shows a 10 % reflection followed by a 5 % undershoot. At the time of these measurements, the author could not determine if these artefacts are due to the coaxial setup imperfections or the WCT itself. Nevertheless, their cause was not investigated in great detail as the monitor's intended bandwidth was much smaller. The LHC bunches exist within 2.5 ns RF buckets which hold all the related bunch intensity information. Therefore, the highest frequency limit foreseeable for the LHC would not exceed 400 MHz.

Figure 4.3 shows the fast impulse response of the FBCT and ICT with the horizontal scale covering a period 3 time longer than that of Fig. 4.2. The outputs of both sensors arrived directly to the oscilloscope using short cables as the corresponding filters installed in the LHC were not available for laboratory measurements.

Comparably to the WCT, the FBCT's response closely follows the excitation pulse for about 2 ns. However, unlike for the new monitor, there are around 25 ns of subsequent oscillations with the main resonant frequency in the order of 400 MHz. This effect is caused mostly by the electromagnetic field trapped inside the FBCT housing due to its significant longitudinal impedance around this frequency. Section 4.1.8 will present further data supporting this claim.

The fast pulse response of the ICT shows different characteristics than the measurements

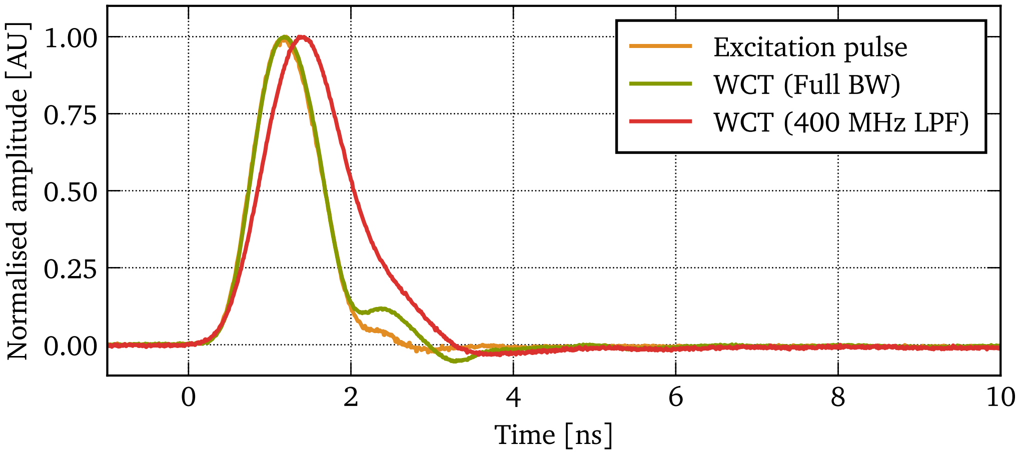

Figure 4.2: Time response of the WCT measured on the coaxial setup.

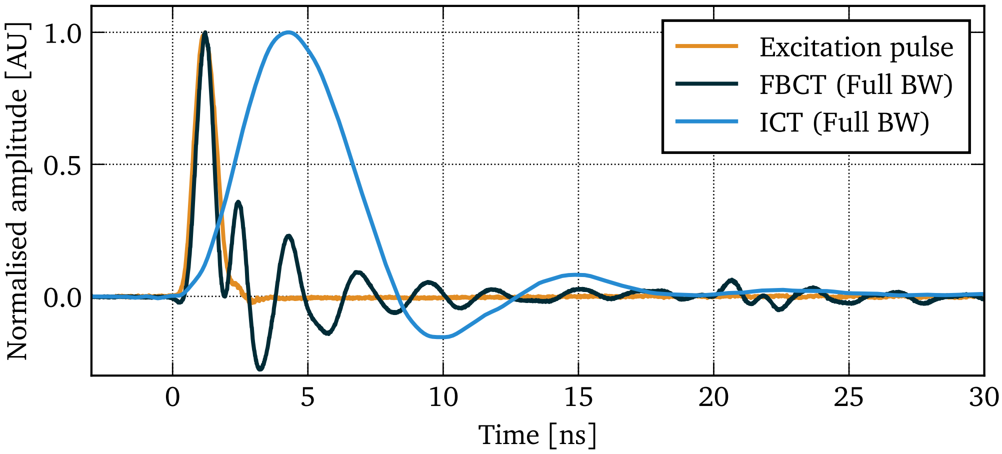

Figure 4.3: Time response of the FBCT and the ICT measured on the coaxial setup.

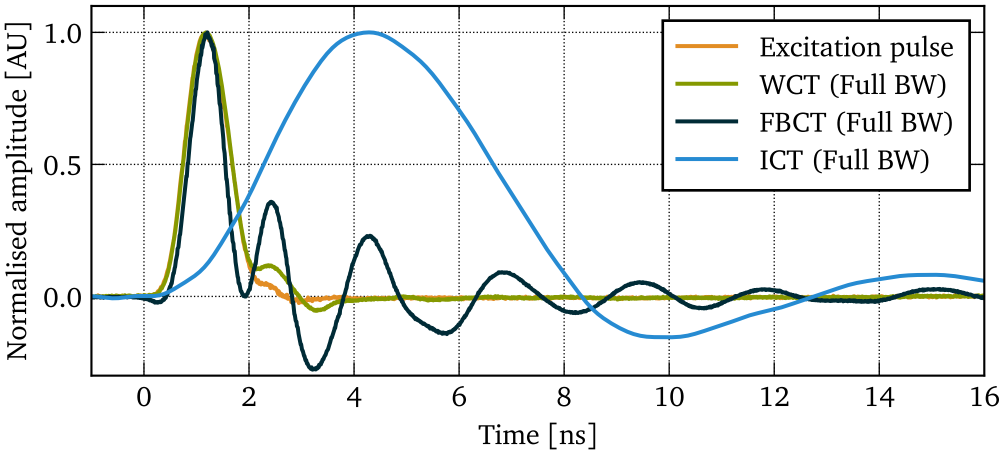

Figure 4.4: Time response of the WCT, FBCT, and ICT in their full bandwidth configurations.

obtained with the other two sensors. The main output pulse is much longer, spanning over some 8 ns. It is then followed by a 10 ns 15 % single-period oscillation and finally by a several-nanosecond-long reflection at a few percent level.

Since 25 ns separate two consecutive LHC bunches, the end parts of the long FBCT and ICT output could interfere with the sensor's response to the following bunch. In principle, one could correct such an artefact by deconvolution of the output signal with a reference single-bunch response. Such a process, however, would assume that the shape of the FBCT and ICT output pulse is independent of other beam parameters such as the transverse beam position or spectral power density. At the time of writing this thesis, the author could not prove such an assumption to be true. The presented measurements indicate that due to the output pulse shape both the FBCT and ICT can introduce an error to any LHC bunch intensity measurement system.

4.1.3 Slow pulse response

The WCT, as well as the FBCT and ICT, is a current transformer with no DC response. For excitations containing a DC component (such as a particle beam current), the sensor's output experiences a baseline drift. A straight-forward way to demonstrate and quantify this behaviour is recording the sensor's response to a long rectangular excitation, as shown in Fig. 4.5.

The WCT's output signal exponentially decays by 75 % over 500 µs. Assuming a first-order exponent, the sensor's time constant τ is $\tau_{\mathrm{WCT}} = 360\,\mu\mathrm{s}$. From this, one can calculate the low cut-off frequency f_{L} of the WCT:

$$f_{\mathrm{L}} = \frac{1}{2\pi\tau_{\mathrm{WCT}}} \approx 440\,\mathrm{Hz} \tag{4.1}$$

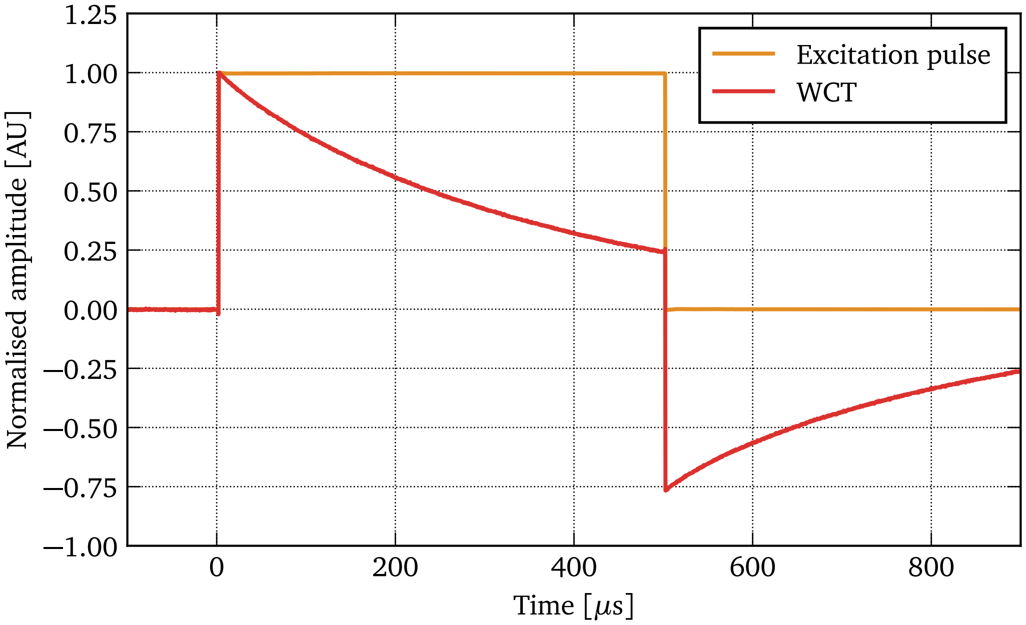

Figure 4.5: Time response of the WCT to a long pulse.

4.1.4 Output symmetry

A major design difference distinguishing the WCT from the other typical BCTs are its multiple intermediate outputs which externally combine to provide a single bunch current signal. This imposes and additional requirement on the WCT that all its outputs are symmetric, i.e. they provide equal signals for a perfectly centred beam. However, what is indeed important, is the signal integral symmetry regardless of the signal shape symmetry.

This measurement was particularly challenging to perform in the laboratory for two reasons. Firstly, it is difficult to establish the exact electrical centre of the WCT without a dedicated test bench featuring actuators. Secondly, assuring a perfect symmetry of four somewhat independent acquisition channels takes a significant calibration effort. The results presented below should be regarded as only qualitative.

The outputs of the WCT installed on the coaxial setup were labelled A–D anti-clockwise starting at the monitor's bottom left quarter facing its connectorised side. A 12-bit 1 GHz oscilloscope and recorded at 125 GSa/s using the RIS technique [69] recorded the relevant signals. Figure 4.6 shows the measurements obtained with a 2 ns 20 V excitation signal.

The measurements did not reveal any major asymmetries among the outputs. The apparent difference between the A/C and D/B outputs can be attributed to the oscilloscope [70] and possible deformations of the coaxial line. Due to the limited development time, the author made no further efforts to cross-calibrate the oscilloscope channels.

As previously stated, the WCT requires the intermediate outputs' integrals to be equal when excited by a centred beam. Table 4.1 lists the results of numerical integration of the signals presented in Fig. 4.6. The four WCT outputs acquired with a non-calibrated oscilloscope are within ±1 % which the author deemed to be the precision level of this measurement method.

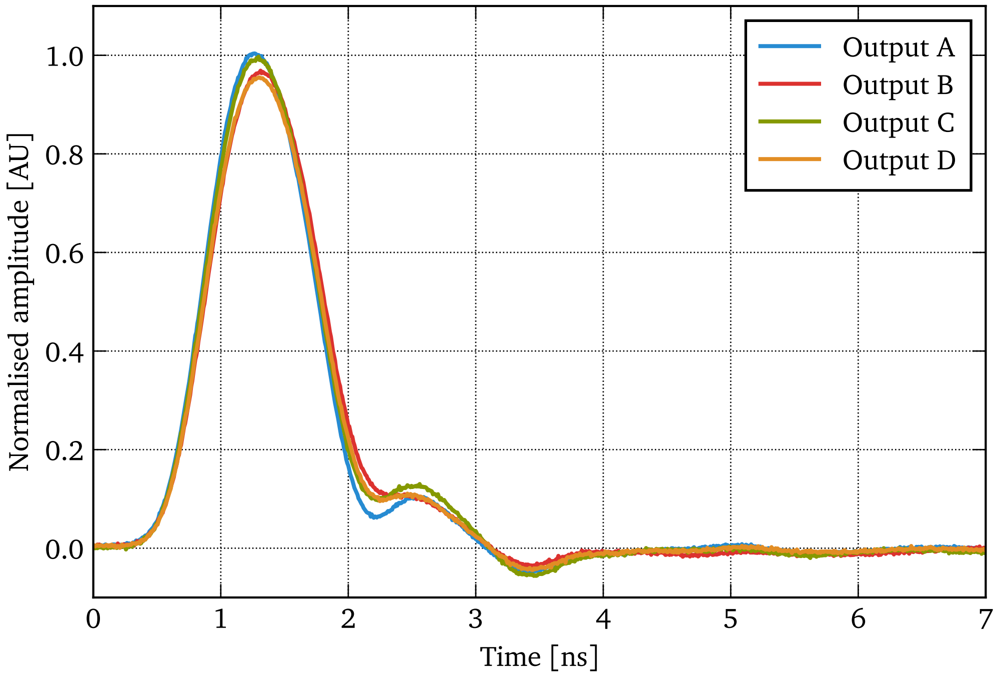

Figure 4.6: Symmetry of the four WCT outputs.

Table 4.1: Integrals of individual WCT outputs measured on the coaxial setup.

Output	Integral [AU]
A	1.0000
B	1.0036
C	1.0096
D	0.9912

4.1.5 Wire position sensitivity

In order to estimate the approximate WCT's sensitivity to the transverse beam position, the author assembled a simple measurement test bench in the laboratory. For the sake of convenience, a copper wire loop driven by a 30 MHz signal generator substituted the particle beam. One segment of the loop passed through the WCT, as shown in Fig. 4.7. Additionally, the loop was terminated with a series 50 Ω resistance for minimalistic matching with the generator's output.

The excitation signal sent to the loop for most of the tests was a 10 V peak-peak 16 ns long rectangular wave with a modest repetition rate of 1 kHz. Small transverse displacements of the wire loop within the WCT mimicked the "beam" offset. A fast oscilloscope recorded the four intermediate WCT outputs. Figure 4.8 demonstrates the signal labelling convention using letters A - D anti-clockwise starting at the bottom left quarter facing the connectorised side of the sensor. The same figure indicates the seven locations of simulated beam offset (P0 through P6) chosen arbitrarily to cover around 30 % of the sensor's aperture. The beam at the WCT location does not typically deviate by more than ±5 mm from the vacuum chamber axis. The wire's position within the WCT was fixed manually with the precision of about ±0.1 mm.

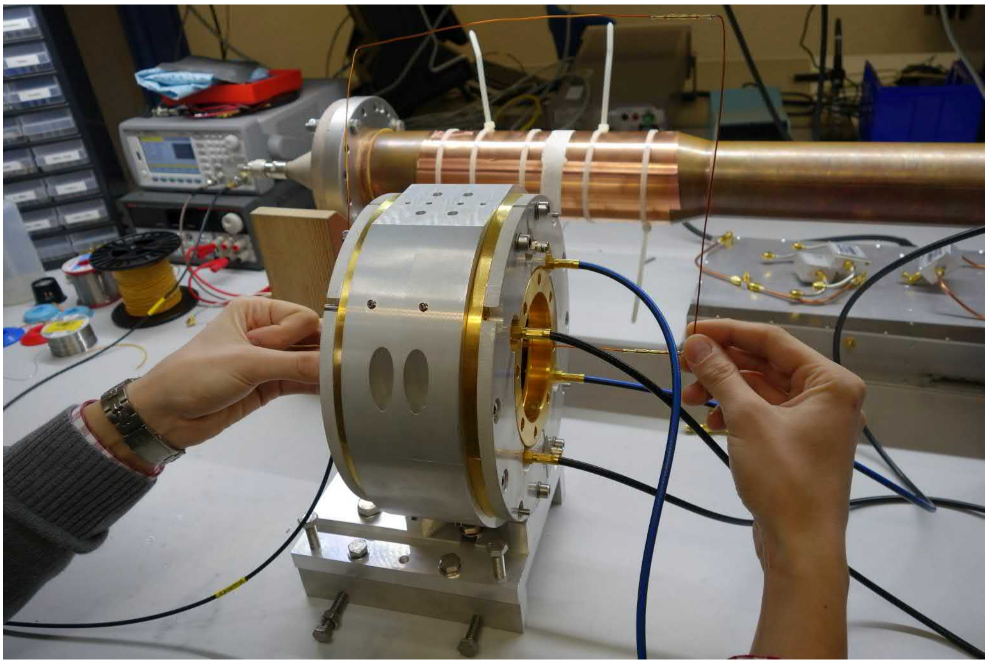

Figure 4.7: Setup for WCT wire position sensitivity measurements.

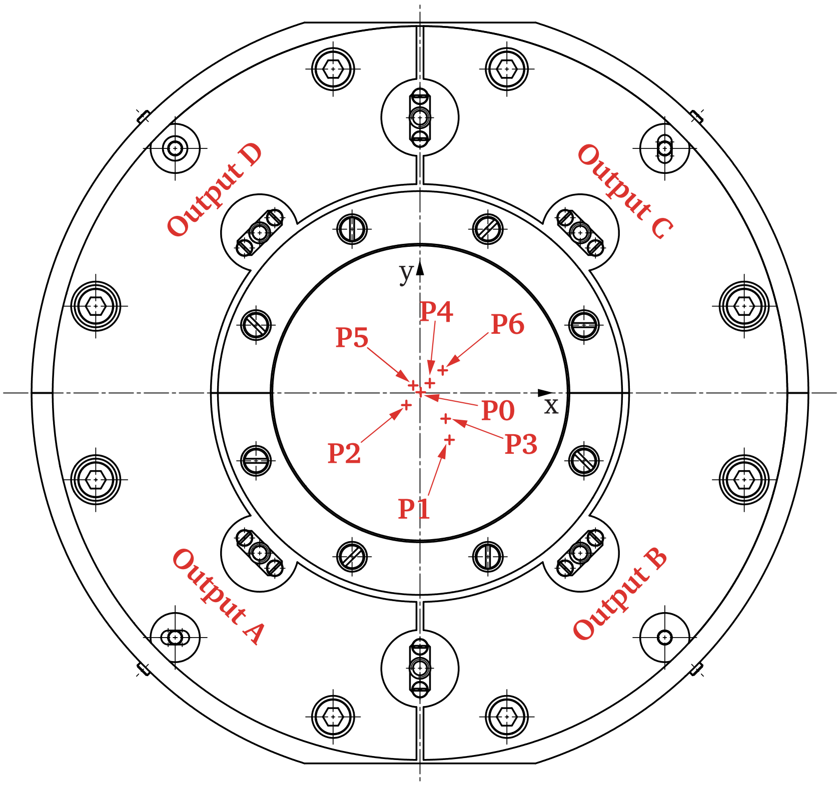

Figure 4.8: Locations of the wire for WCT position sensitivity estimation.

Whilst one can anticipate that the integrals of the individual WCT outputs would vary for different positions of the excitation loop, their sum should remain constant regardless of the loop's displacement. This would be equivalent to the WCT being insensitive to the beam displacement.

Fig. 4.9 presents the measurements obtained for the first 6 "beam" offsets (P0 through P5) with Σ depicting a numerical sum of the four recorded signals. The plots clearly demonstrate that each WCT output is visibly sensitive to the loop's transverse position. The summed signal, however, looks remarkably similar in all cases.

Table 4.2 provides a further numerical analysis and summarises the amplitudes of each output, the amplitude of the sum and its integral for each measurement point. Noticeably, in the most extreme case the amplitude of an output changed by a factor of 5 whereas the integral of the summed signal stays within ±1 %. The author deemed this as the obtainable precision of such a measurement method and, due to the limited development time, made no further efforts to analyse the potential WCT sensitivity to a beam position at a sub-percent level.

The P6 position served to measure the low cut-off frequency of the beam-position-sensitive component of the WCT signal. Due to the azimuthal inductance between the WCT's conductive screws, below a certain frequency the image current flowing through the screws tends to equalise. This, in turn, leads to a loss of the beam position sensitivity as demonstrated in Fig. 4.10. The excitation signal injected into the wire loop was a 100 µs long rectangular pulse with a sharp 16 ns edge. The loop was at the position P6 ($x = 8\,\mathrm{mm}, y = 8\,\mathrm{mm}$), i.e. far from the output A, close to the output C, and equidistant from the outputs B and D.

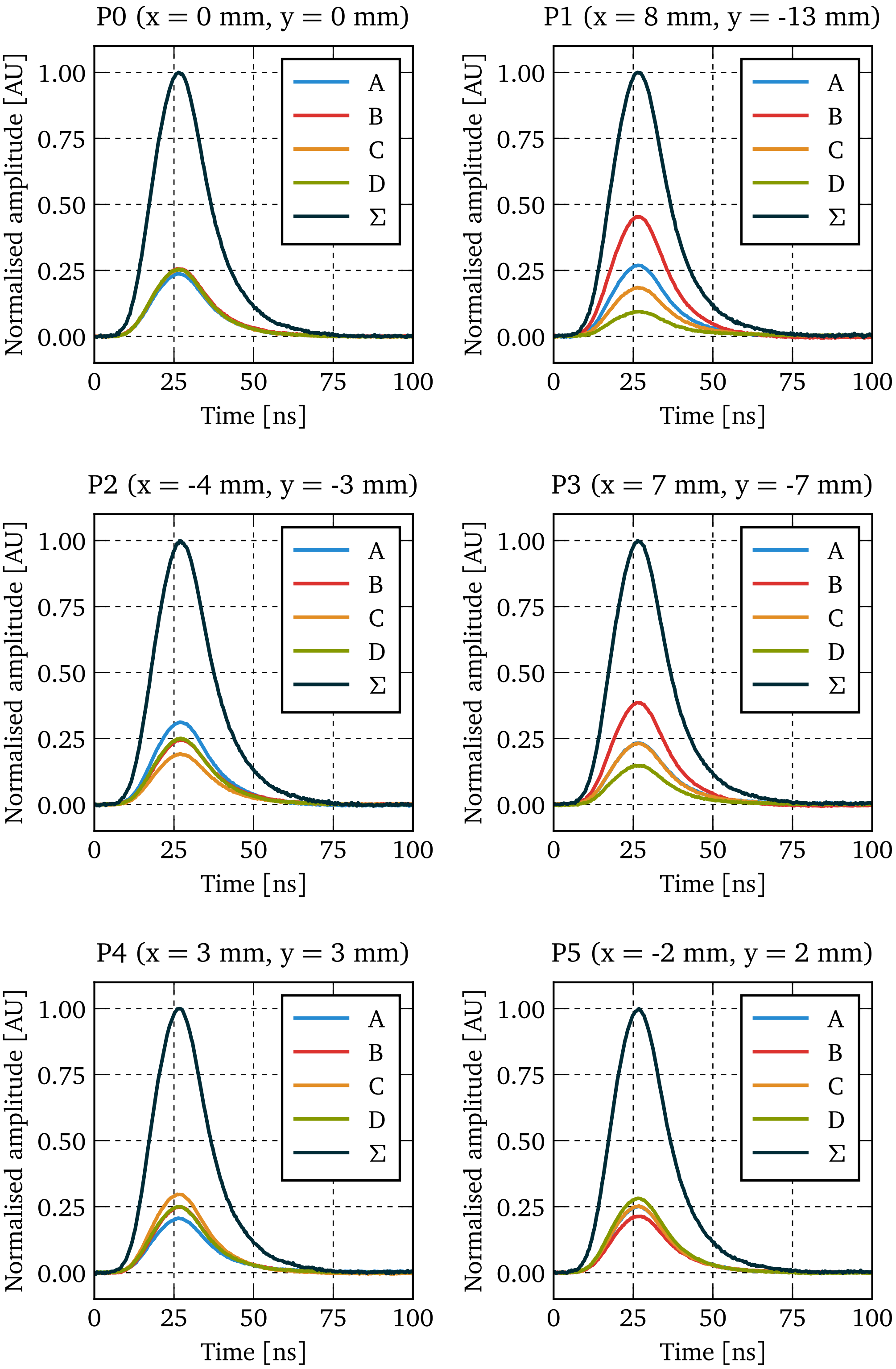

Figure 4.9: Fast impulse response of the individual WCT outputs for different wire position.

Table 4.2: Results of the wire-based WCT position sensitivity measurements.

	Wire offset [mm]		Signal amplitude [AU]					Integral
	x	y	A	B	C	D	Sum	[AU]
P0	0	0	0.237	0.255	0.253	0.254	1.000	21.986
P1	8	−13	0.270	0.452	0.185	0.094	1.001	22.272
P2	−4	−3	0.315	0.246	0.193	0.249	0.999	22.056
P3	7	−7	0.233	0.386	0.232	0.148	1.000	22.426
P4	3	3	0.205	0.250	0.295	0.251	1.001	22.041
P5	−2	2	0.252	0.213	0.253	0.282	1.000	22.159
P6	8	8	0.092	0.214	0.460	0.214	1.000	-

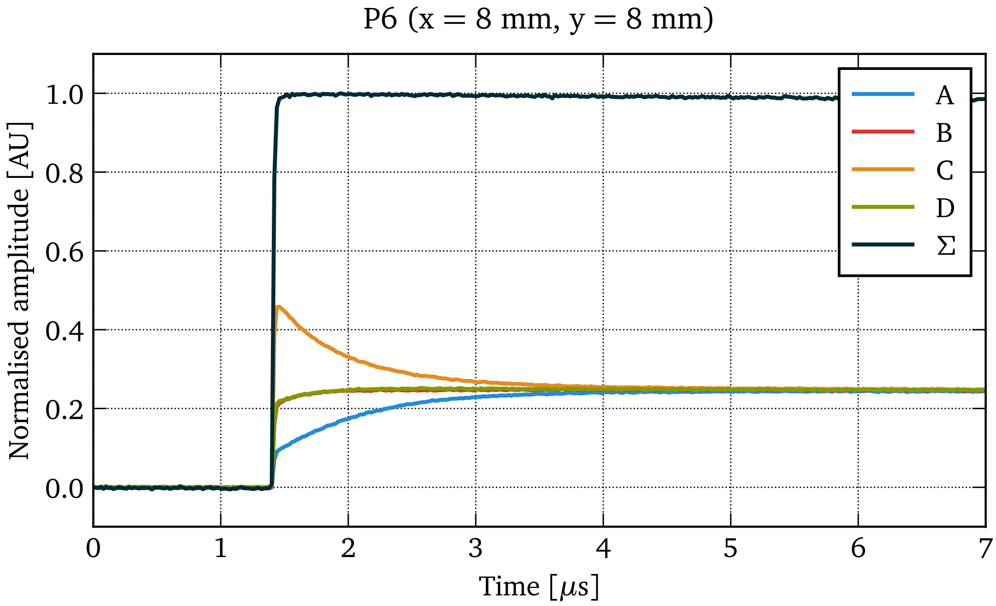

Figure 4.10: Long pulse response of the individual WCT outputs for the P6 wire position.

During the first few microseconds, the highest signal is present at the output C (closest to the wire loop), with outputs B and D having the same amount of signal, and the smallest amplitude at output A (farthest from the loop). After around 5 µs, all the outputs are at virtually the same level even though the wire loop remained at its original displacement.

The signals approach their steady state in an exponential manner. The time constant of this process, derived from the measurements, is $\tau_{\text{BPM}} = 550\,\text{ns}$. From this, the low cut-off frequency of the beam position sensitive component of the WCT outputs is:

$$f_{\text{L,BPM}} = \frac{1}{2\pi\tau_{\text{BPM}}} \approx 290\,\text{kHz} \tag{4.2}$$

The above exercise reveals that for slow signals (e.g. long bunches), the WCT would be insensitive to the transverse beam position. This is only a theoretical limit as typical signals which the sensor operates with are several orders of magnitude faster.

To quantify the WCT's beam position sensitivity for fast signals, let's label the signals at outputs A through D as V_{A} through V_{D}. Let's also define the following relations:

$$\begin{aligned} V_{\Sigma} &= V_{\mathrm{A}} + V_{\mathrm{B}} + V_{\mathrm{C}} + V_{\mathrm{D}} \\ V_{\Delta\mathrm{CA}} &= V_{\mathrm{C}} - V_{\mathrm{A}} \\ V_{\Delta\mathrm{BD}} &= V_{\mathrm{B}} - V_{\mathrm{D}} \end{aligned} \tag{4.3}$$

In order to translate the WCT output signals to a transverse beam position let's define a two-dimensional Cartesian coordinate system $(x_{\mathrm{WCT}}, y_{\mathrm{WCT}})$ with the following properties:

- axis X_{WCT} runs from the output A to C;
- axis Y_{WCT} runs from the output D to B;
- the origin $(0,0)$ is in the geometric centre of the sensor.

In such a coordinate system, and for relatively small beam displacements, one can consider the WCT as a simple linear BPM for which the beam position measured along the X_{WCT} axis is proportional to V_{CA} and, likewise, the beam position measured along the Y_{WCT} axis is proportional to V_{BD} [28]. With a proportionality factor k_{WCT}, the above becomes:

$$\begin{bmatrix} x_{\mathrm{WCT}} \\ y_{\mathrm{WCT}} \end{bmatrix} = k_{\mathrm{WCT}} \begin{bmatrix} V_{\Delta\mathrm{CA}} \\ V_{\Delta\mathrm{BD}} \end{bmatrix} \tag{4.4}$$

For any practical BPM, it would be more convenient to use a traditional (x, y) coordinate system with one axis parallel to the plane on which the accelerator is built. One can achieve this by translating the $(x_{\mathrm{WCT}}, y_{\mathrm{WCT}})$ using a rotation matrix:

$$\begin{bmatrix} x \\ y \end{bmatrix} = R_{\mathrm{WCT}} \begin{bmatrix} x_{\mathrm{WCT}} \\ y_{\mathrm{WCT}} \end{bmatrix} \tag{4.5}$$

For a given anticlockwise rotation angle θ this matrix has a form [71]:

$$R = \begin{bmatrix} \cos\theta & -\sin\theta \\ \sin\theta & \cos\theta \end{bmatrix} \tag{4.6}$$

Since the WCT's outputs are located at 45° of the typical (x, y) coordinate system, one gets that $\theta_{\mathrm{WCT}} = 45° = \frac{\pi}{4}$. From that the rotation matrix of the WCT is:

$$R_{\mathrm{WCT}} = \begin{bmatrix} \frac{\sqrt{2}}{2} & -\frac{\sqrt{2}}{2} \\ \frac{\sqrt{2}}{2} & \frac{\sqrt{2}}{2} \end{bmatrix} \approx \begin{bmatrix} 0.71 & -0.71 \\ 0.71 & 0.71 \end{bmatrix} \tag{4.7}$$

Let's introduce the rotation matrix to eq. 4.4 to translate the measurements into the (x, y) coordinate system:

$$\begin{bmatrix} x \\ y \end{bmatrix} = k_{\mathrm{wct}} R_{\mathrm{wct}} \begin{bmatrix} V_{\Delta\mathrm{CA}} \\ V_{\Delta\mathrm{BD}} \end{bmatrix} \tag{4.8}$$

To establish the proportionality factor k_{WCT}, let's consider the WCT as an ideal BPM for which the electrodes (i.e. outputs) measure the image current induced by the beam on the vacuum chamber walls. The proportionality factor k of such a BPM with an aperture d and an angular coverage ϕ of a single electrode is [28]:

$$k = \frac{\phi}{4\sin\frac{\phi}{2}}\frac{d}{V_{\Sigma}} \tag{4.9}$$

The four WCT outputs provide a total coverage of the image current. With their symmetrical arrangement, each output covers a quarter of the vacuum chamber circumference:

$$\phi_{\mathrm{WCT}} = 90^{\circ} = \frac{\pi}{2} \tag{4.10}$$

A combination of the two above equations leads to the estimation of the WCT's beam position sensitivity proportionality factor:

$$k_{\mathrm{WCT}} = \frac{\pi}{4\sqrt{2}}\frac{d}{V_{\Sigma}} \approx 0.56\frac{d}{V_{\Sigma}} \tag{4.11}$$

Finally, by incorporating the numerical values of k_{WCT} and R_{WCT} into eq. 4.8, one achieves the formula to convert the signals measured by the individual WCT outputs into transverse beam position information:

$$\begin{bmatrix} x \\ y \end{bmatrix} \approx \frac{31.81\,\mathrm{mm}}{V_{\Sigma}}\begin{bmatrix} 1 & -1 \\ 1 & 1 \end{bmatrix}\begin{bmatrix} V_{\Delta\mathrm{CA}} \\ V_{\Delta\mathrm{BD}} \end{bmatrix} \tag{4.12}$$

To validate the above, let's consider the signals measured at the location P4 (3 mm, 3 mm):

$$\begin{aligned} V_{\Sigma} &= 1.001 \\ V_{\mathrm{CA}} &= 0.090 \\ V_{\mathrm{BD}} &= -0.001 \end{aligned} \tag{4.13}$$

Introduction of these values into eq. 4.12 yields:

$$\frac{31.81\,\mathrm{mm}}{1.001}\begin{bmatrix} 1 & -1 \\ 1 & 1 \end{bmatrix}\begin{bmatrix} 0.090 \\ -0.001 \end{bmatrix} = \begin{bmatrix} 2.89 \\ 2.83 \end{bmatrix}\mathrm{mm} \tag{4.14}$$

The results are remarkably close to the assumed position of (3 mm, 3 mm), especially given that the loop's position was neither calibrated not precisely controlled during the measurement.

All the analysis carried out so far considered only relative changes between the outputs. The WCT, as any other sensor, provides signals of measurable amplitude. In order to assess the WCT's beam position sensitivity in absolute terms, one has to establish the monitor's sensitivity to the beam charge. As demonstrated in section 3.4.5, for the LHC sensor's output voltage sensitivity to the beam charge is:

$$S_{\mathrm{WCT}} \approx 43.5\,\mathrm{mV\,nC^{-1}} \tag{4.15}$$

For clarity of the following analysis let's define the WCT geometric factor from eq. 4.12:

$$\alpha_{\mathrm{WCT}} = 38.81\,\mathrm{mm} \tag{4.16}$$

Rearranging eq. 4.12 by multiplying it by the inverse of the rotation matrix R_{WCT} yields:

$$\frac{1}{V_\Sigma}\begin{bmatrix} V_{\Delta \mathrm{CA}} \\ V_{\Delta \mathrm{BD}} \end{bmatrix} = \frac{1}{\alpha_{\mathrm{WCT}}}\begin{bmatrix} 0.5 & 0.5 \\ -0.5 & 0.5 \end{bmatrix}\begin{bmatrix} x \\ y \end{bmatrix} \tag{4.17}$$

Let's now introduce a diagonal beam displacement r such that:

$$x = y = r \tag{4.18}$$

This is equivalent to an in-axis offset of r in the original coordinate system $(x_{\mathrm{WCT}}, y_{\mathrm{WCT}})$ and simplifies analysis by decoupling both axes:

$$\frac{1}{V_\Sigma}\begin{bmatrix} V_{\Delta \mathrm{CA}} \\ V_{\Delta \mathrm{BD}} \end{bmatrix} = \frac{1}{\alpha_{\mathrm{WCT}}}\begin{bmatrix} r \\ 0 \end{bmatrix} \tag{4.19}$$

As no displacement is present in Y_{WCT}, the problem reduces to a single dimension:

$$V_\Delta = V_\Sigma \frac{r}{\alpha_{\mathrm{WCT}}} \tag{4.20}$$

The sum signal V_Σ is a combination of the four WCT's intermediate outputs, each of which has a sensitivity S_{WCT}. For a beam charge Q, the sum becomes:

$$V_\Sigma = 4\,S_{\mathrm{WCT}}\,Q \tag{4.21}$$

Combining the two above equations results in the value of the difference signal for an in-axis displacement r of a beam with charge Q:

$$V_\Delta = 4\,S_{\mathrm{WCT}}\,Q \frac{r}{\alpha_{\mathrm{WCT}}} \tag{4.22}$$

Finally, one can define the WCT's beam position sensitivity normalised to the transverse beam displacement and the beam charge as:

$$S_{\Delta \mathrm{WCT}} \equiv \frac{V_\Delta}{Q\,r} = 4\frac{S_{\mathrm{WCT}}}{\alpha_{\mathrm{WCT}}} \approx 4.5\,\mathrm{mV\,mm^{-1}\,nC^{-1}} \tag{4.23}$$

To conclude the analysis, one can consider a realistic LHC beam charge to evaluate possible application of the WCT as a BPM. For a nominal LHC bunch of 20 nC (1.25×10^{11} protons) displaced by 1 mm from the sensor's centre the difference between the opposite outputs' amplitudes would be in the order of 90 mV.

4.1.6 Bandwidth

A classic way of characterising high-frequency sensors is to measure their response in frequency domain with a Vector Network Analyser (VNA) through scattering (S) parameters [72].

The author installed the WCT, FBCT and ICT on the laboratory coaxial setup and measured their frequency response using three ports of a 4-port VNA as shown in Fig. 4.11. The first port was connected to the coaxial setup input, the second to the output of each sensor's output, and finally the third to the coaxial setup output. In such a configuration, the S21 parameter characterises the coupling between the coaxial setup and the installed monitor, whereas the S22 parameters characterises the sensor's output voltage reflection coefficient.

Before discussing the VNA measurements it is important to emphasise that the laboratory coaxial setup can only approximate the real electromagnetic field generated by an ultrarelativistic beam, especially at very high frequencies. A particle beam moving close to the speed of light in a continuous vacuum chamber generates only transverse electromagnetic (TEM) field, as explained previously in section 2.1.3. On the other hand, the coaxial setup's geometry and some unavoidable discontinuities will lead to the appearance of additional field modes which might affect the measurement quality.

Figure 4.12 shows the frequency response of the FBCT, WCT and ICT in the range of 1 MHz to 2000 MHz. The FBCT and WCT were measured in two configurations: without any external filtering (labelled as "Full BW") and with an external low-pass filter which each sensor features as installed in the LHC (labelled as "LPF"). Moreover, the measurements were normalised such that the response of each monitor at 1 MHz is equal to 0 dB.

The FBCT in its unfiltered configuration exhibited a 3 dB high cut-off frequency of approximately 1 GHz. Nonetheless, deviations at the level of ±1 dB begin appearing above 30 MHz and a very strong resonance is present around 450 MHz. Both of these irregularities deteriorate the quality of the FBCT time-domain response, especially the latter which manifests itself as a relatively slowly decaying oscillation following the main beam-induced pulse. For the FBCT installed in the LHC, a 80 MHz low-pass strongly attenuates the 450 MHz resonance, as shown in Fig. 4.12. Despite that, the less pronounced magnitude deviations in the range 30 MHz to 100 MHz remain visible as they are within the filter's bandwidth. Due to these deviations, the 3 dB bandwidth of the monitor after filtering is slightly higher than the cut-off frequency of the filter itself and reaches approximately 100 MHz.

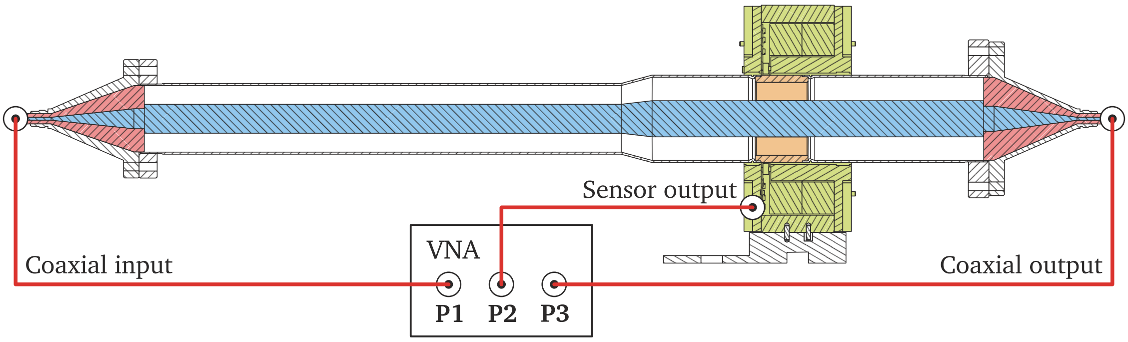

Figure 4.11: Connections for laboratory bandwidth measurements.

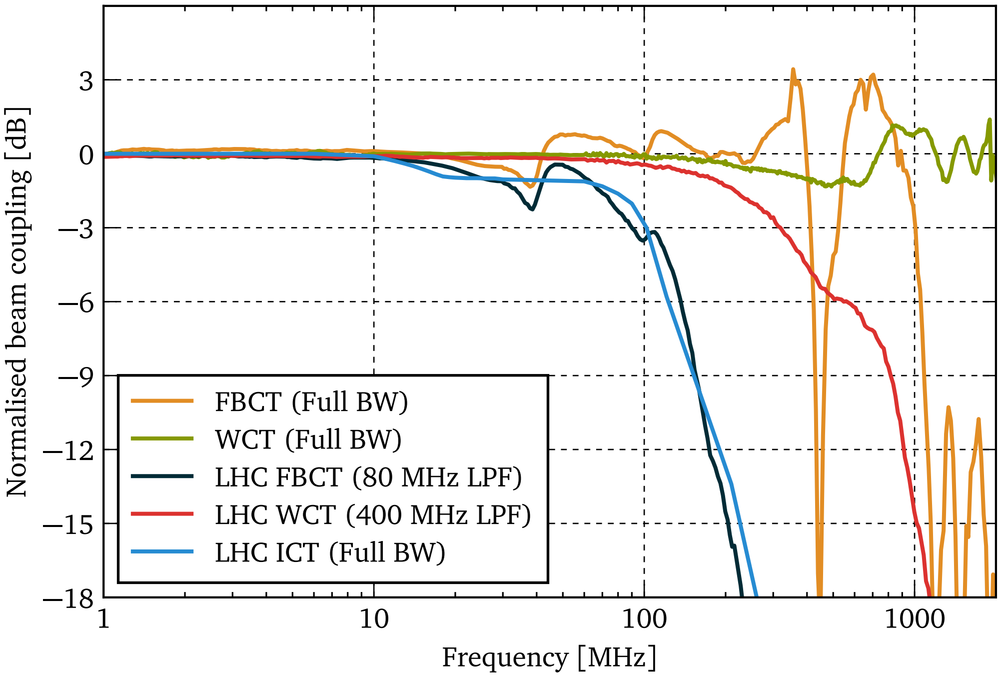

Figure 4.12: Frequency response of the FBCT, WCT and ICT measured with a coaxial setup.

The full bandwidth measurements of the WCT further validate its excellent time-domain response discussed at the beginning of the chapter. The sensor's coupling to the input signal remains constant within ±1 dB up to 2 GHz, which the author deemed as the maximum frequency for reliable measurements with the coaxial setup. Moreover, the first abnormal behaviour of the WCT appears only above 700 MHz, where limited power of the input signal is still available. A 400 MHz filter, chosen for the final LHC installation, provided a good compromise between removing any high-frequency unpredictability and maintaining a fast time-domain response.

Finally, frequency response of the ICT is strikingly similar to the one of the FBCT with a low-pass filter with a 3 dB bandwidth of around 100 MHz. The ICT response is smoother without any significant deviations, however, at around 18 MHz it drops by 1 dB. Due to the ICT's commercial non-disclosed design, the cause of this drop remains not understood by the author.

4.1.7 Impedance matching

As the output signal duration of the three discussed sensors is in the nanosecond range, good impedance matching becomes an important design objective. To assure optimal signal transmission, the sensor's output impedance Z_{OUT} should be matched to the characteristic impedance Z_0 of the used cables as well as to the input impedance Z_{IN} of the following electronics. The value almost universally used for high-frequency measurements is $Z_{\mathrm{OUT}} = Z_0 = Z_{\mathrm{IN}} = 50\,\Omega$.

Using the measurement setup described in section 4.1.6, the S22 parameter, commonly referred to as the output voltage reflection coefficient, can serve to asses the output impedance matching of each monitor:

$$S_{22} = 20 \log_{10} \frac{Z_{\mathrm{DUT}} - Z_0}{Z_{\mathrm{DUT}} + Z_0} \tag{4.24}$$

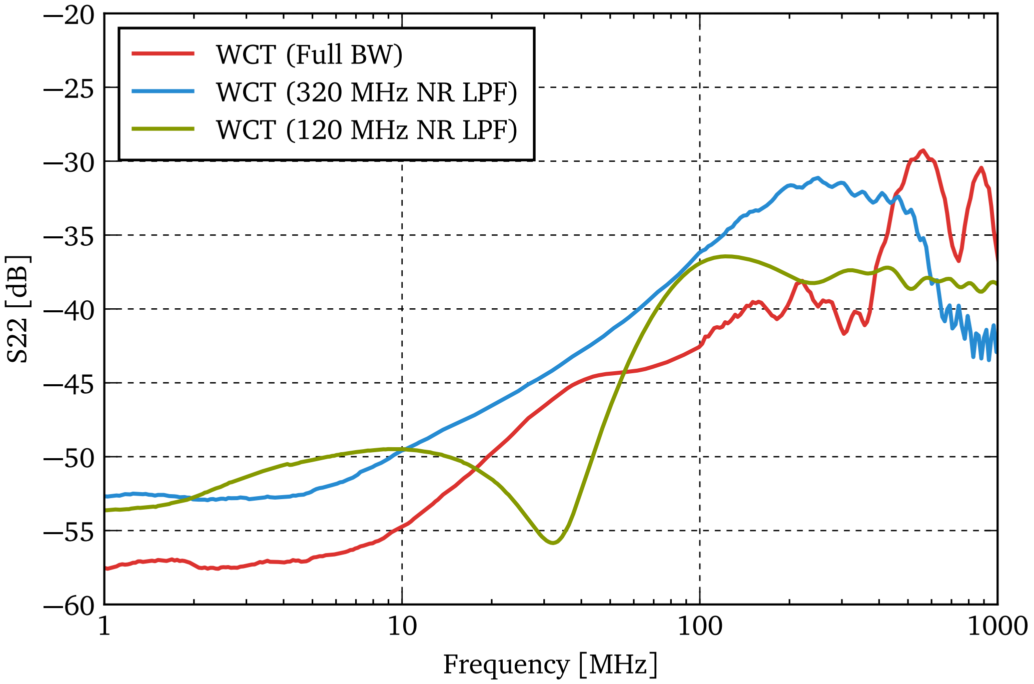

Figure 4.13: Reflection coefficient of the WCT output.

where Z_{DUT} is the unknown output impedance and Z_0 is the reference impedance. Low values of S22 correspond to good impedance matching.

Figure 4.13 shows the WCT S22 measurements. To demonstrate the influence of an external filter on the output impedance, the author measured the WCT in three different configurations: without any added filter (labelled as “Full BW”) and with two absorptive low-pass filters with cut-off frequencies at 320 MHz and 120 MHz. In all three cases, the sensor demonstrated a very good impedance matching up to 1 GHz. Even for very high frequencies, the S22 parameter remains below −30 dB which translates to the maximum impedance variation of ±6.5 %. For comparison, good-quality commercial low-power 50 Ω loads reach S22 values of −32 dB for the same connector type and frequency range.

4.1.8 Longitudinal impedance

The electromagnetic field of a charged particle beam interacts with any structure through which the beam travels. Depending on the materials and geometries used in components seen by the field, the beam might lose a non-negligible amount of energy leading to heat generation and other detrimental effects. The property typically used to quantify this behaviour is called the longitudinal beam-coupling impedance [73] and is a frequency domain representation of the component’s electromagnetic response to an impulse excitation.

Reducing the longitudinal impedance is particularly important in accelerators using high-power beams, such as the LHC, in which even a very small fraction of the beam power could constitute a significant source of heat. One must take appropriate precautions at the design stage for any accelerator component. The two primary factors responsible for an increase in the longitudinal impedance are hollow cavities exposed to the beam's electromagnetic field and discontinuities in the conductive vacuum chamber.

Although electromagnetic simulations can compute the longitudinal beam-coupling impedance of a given component, it is a common practice to carry out laboratory measurements to characterise newly designed components. In the traditional method, a wire which is coaxial to the component under study substitutes the particle beam [74]. To calculate the component's longitudinal impedance, one measures the transmission through the wire and compares it to a reference measurement for which a perfectly conductive surface replaces the component. For $S_{21,\mathrm{DUT}}$ being the transmission through the wire with the component in-place, $S_{21,\mathrm{REF}}$ being the reference transmission measurement, and Z_0 being the characteristic impedance of the coaxial arrangement, the longitudinal beam-coupling impedance Z_{DUT} of the studied component is:

$$Z_{\mathrm{DUT}} = -2Z_0 \ln \frac{S_{21,\mathrm{DUT}}}{S_{21,\mathrm{REF}}} \tag{4.25}$$

Since both $S_{21,\mathrm{DUT}}$ and $S_{21,\mathrm{REF}}$ are complex, so is the resulting longitudinal beam-coupling impedance Z_{DUT}. The real part of Z_{DUT} corresponds to the loss of beam energy due to electromagnetic interactions with the structure whilst the imaginary part of Z_{DUT} is correlated to the change particles experience in their motion along the accelerator.

Using the above described method, the author measured the beam coupling impedance of the FBCT and WCT. As the ICT was not available during the measurement campaign, the thesis presents no results for that sensor. Nevertheless, its mechanical assembly and used materials are from the electromagnetic point of view similar to the the ones of FBCT and the author expects the two sensors to exhibit a comparable behaviour.

During measurements, the central conductor of the laboratory coaxial setup played the role of a wire. For reference transmission measurements, a copper sheet surrounded the ceramic insert and firmly attached to a cleaned conductive surface on either side. Then, transmission measurements were conducted with each of the sensors installed on the setup. Figure 4.14 presents the obtained results. Figure 4.15 shows the magnitude as well as the real and imaginary parts of the longitudinal beam-coupling impedance, calculated using eq. 4.25, for both sensors.

The measurements fully validated the WCT low-impedance design with minimised volume of unfilled cavities. The carefully selected ferrite material for the large cores is opaque for electromagnetic fields at high frequencies. Moreover, a clear path for the image current, defined for a wide frequency range, mitigates any discontinuities in the conductive vacuum chamber. As a result, the longitudinal beam-coupling impedance of the WCT remains below 6 Ω up to 2 GHz which was the maximum measurement frequency.

In contrast, the FBCT design does not exhibit low beam-coupling impedance. The large unfilled volumes and significant discontinuities in the image current path lead to two resonant frequencies observed at 380 MHz and just above 1 GHz. In the LHC, there is significant beam power present up to approximately 1.5 GHz and both of the measured resonance contribute to energy loss of the beam.

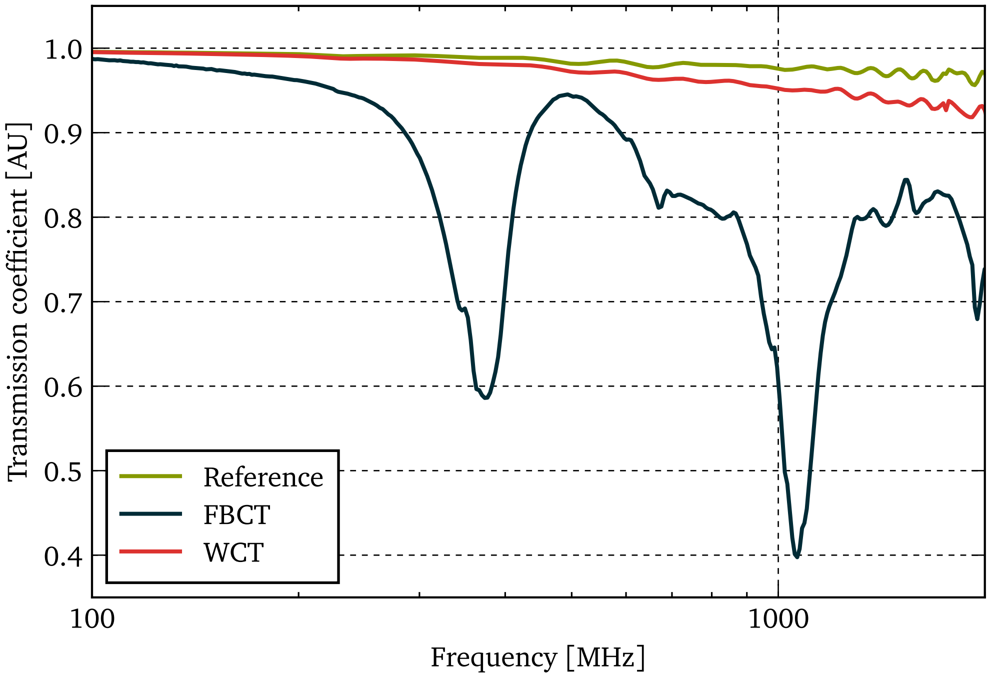

Figure 4.14: Magnitude of the transmission coefficient through the coaxial setup with the FBCT and the WCT installed over the ceramic insert.

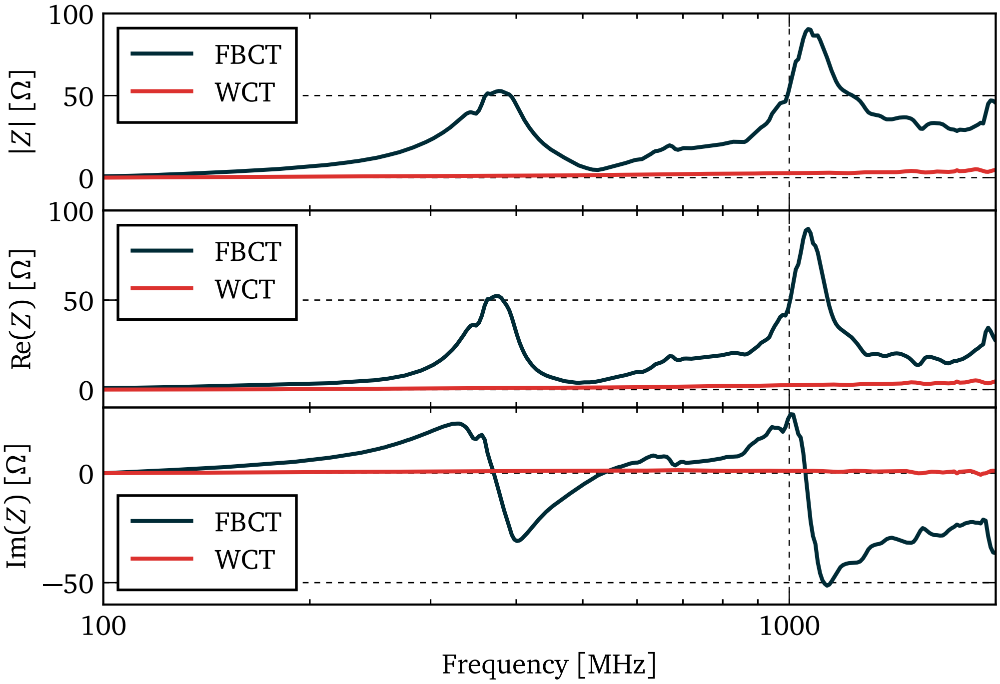

Figure 4.15: Longitudinal beam-coupling impedance of the FBCT and the WCT measured with the coaxial setup.

4.2 LHC installation

Regardless of the thorough laboratory measurements giving very promising results of the potential WCT performance, it was deemed necessary that all three sensors – the already installed FBCT, and the newly designed ICT and WCT – are compared with a real particle beam at the same time. Therefore, deployment of the WCT came in stages as outlined in Fig. 4.16.

Up until the beginning of 2015, there were four FBCTs installed in the LHC. Each LHC ring was equipped with two sensors referred to as an operational "System A" and a redundant "System B". Moreover, since the FBCT's magnetic cores can suffer permanent damage after exposure to excessive heat, each sensor can be fixed in one of two positions: "measurement" used during the accelerator operation, and "parking" over water-cooled tubes used whenever high-temperature treatment of the vacuum chamber is required. Figure 4.16 follows a naming convention whereby the System A monitor installed on the LHC Ring 1 is labelled as "R1A".

In 2015, at the end of a two-year-long LHC maintenance period Long Shutdown 1 (LS1), the ICT became the System B sensor on Ring 1 (see Fig. 4.17), and the author replaced the System B Ring 2 FBCT with the WCT (see Figs. 4.18 and 4.19). Complete removal of one FBCT enable moving the ICT to the parking position. Since the WCT disassembly does not require opening the vacuum chamber, removal of the other FBCT was not necessary and it was displaced to its parking position making space for the new instrument. With the remaining System A FBCTs (see Fig. 4.20), it was possible to compare the three monitors in various accelerator conditions.

Following a successful 2015 beam measurement campaign reported in the proceeding section, the WCT became the new operational sensor for bunch intensity measurements in the LHC. Hence, in February 2016 both System A FBCTs were displaced to their parking positions and the author installed two new WCTs in the freed slots (see Fig. 4.21).

A total migration to the WCT in the LHC was completed at the beginning of 2017, when another team moved the remaining ICT to its parking position and installed a fourth WCT (see Fig. 4.22). At the same time, another WCT of the same design, was also installed in the second largest accelerator at CERN, the SPS (see Fig. 4.23).

As explained in section 3.4, each WCT installation consisted of the sensor and its front-end electronics installed partially in the LHC tunnel, and partially in an underground technical gallery 10 m away. Figure 4.24 shows an overview diagram of the front-end electronics installation.

A ladder of resistive combiners (labelled as Σ in Fig. 4.24) sums the four WCT intermediate outputs into a single signal. A 400 MHz non-reflective low-pass filter stretches the pulse in time. A coaxial cable brings the signal to the head amplifier fixed to one of the posts supporting the beam line. Two 20 m coaxial cables connect the amplifier's low and high gain outputs to a rack in a nearby underground technical gallery. Each WCT signal passes through a common mode choke, shown in Fig 4.25, breaking any potential ground loops between the tunnel and the technical galleries which could lead to an unwanted low-frequency interference, typically at 100 Hz. Next, non-reflective filters further limit the bandwidth to 200 MHz. The distribution amplifier, shown in Fig. 4.26, produces four copies of each signal. As the amplifier serves four various acquisition system hosted across several racks, as shown in Fig. 4.27, the final low-pass filters and attenuators were selected per application and adapted as needed.

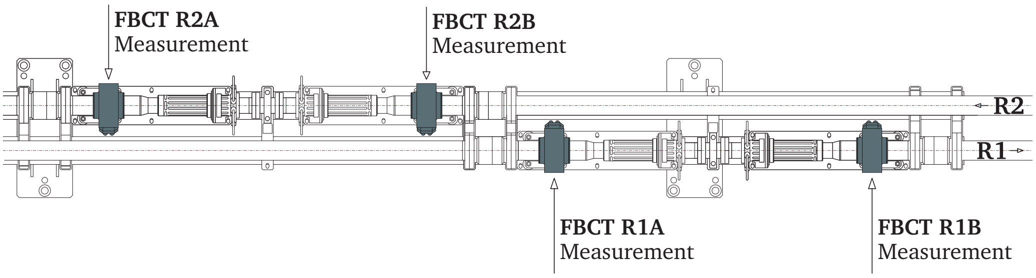

(a) LHC installation status before 2015.

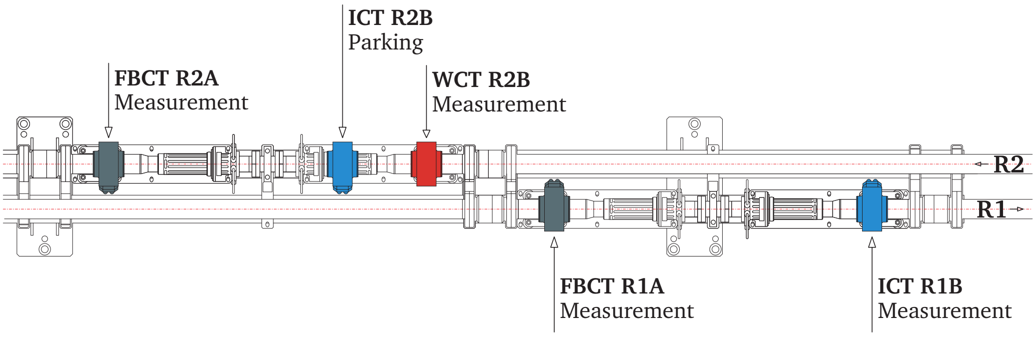

(b) LHC installation status in 2015.

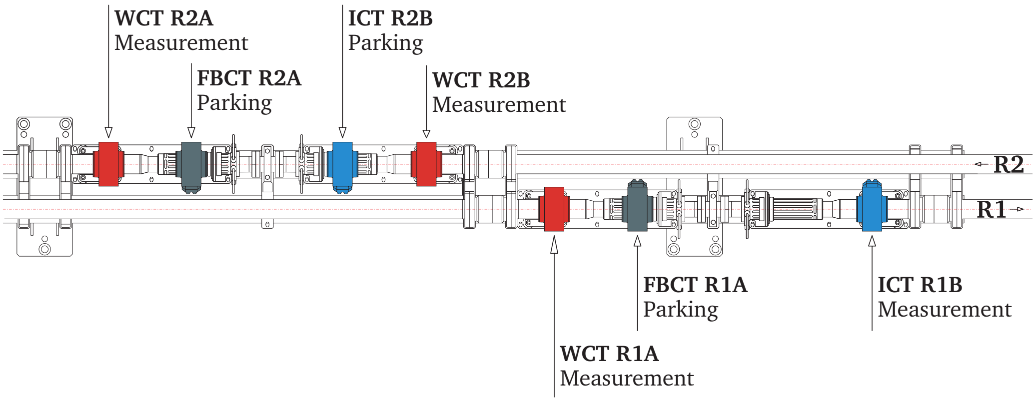

(c) LHC installation status in 2016.

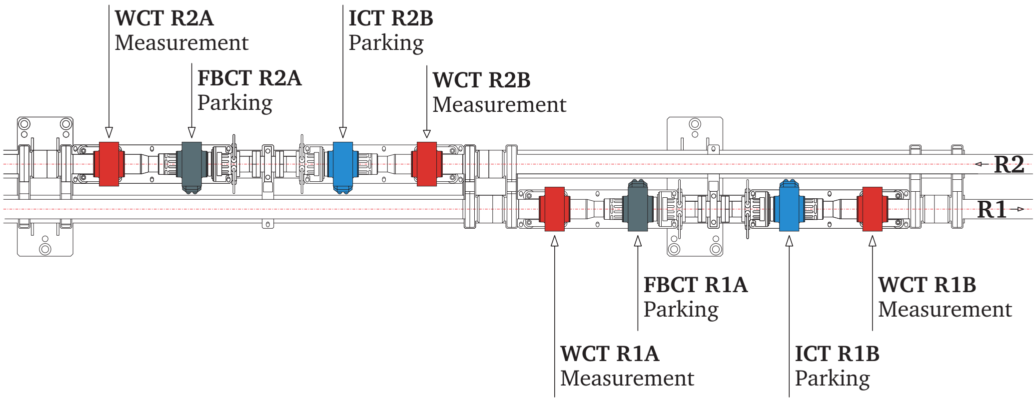

(d) LHC installation status in 2017.

Figure 4.16: Timeline of migration from the FBCT to the WCT in the LHC.

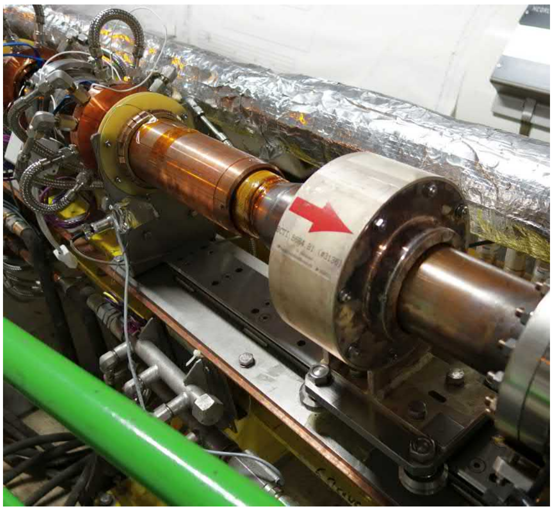

Figure 4.17: ICT R1B installed in the measurement position with the water-cooling circuit visible in the background.

Figure 4.18: WCT R2B installed in the measurement position.

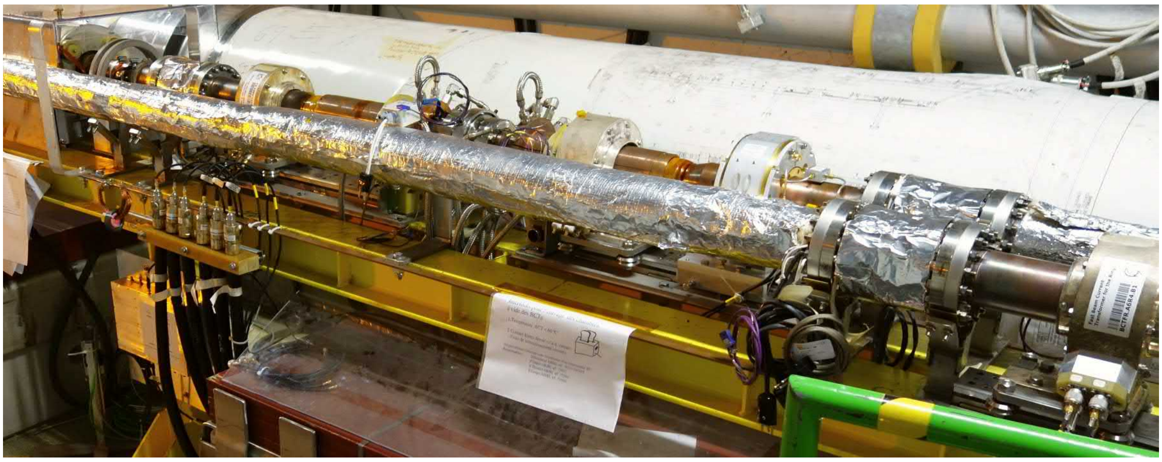

Figure 4.19: WCT R2B with its head amplifier fixed to a yellow vertical support next to FBCT R2A. One of the DCCTs can be seen under the transparent plastic cover.

Figure 4.20: FBCT R1A installed in the measurement position.

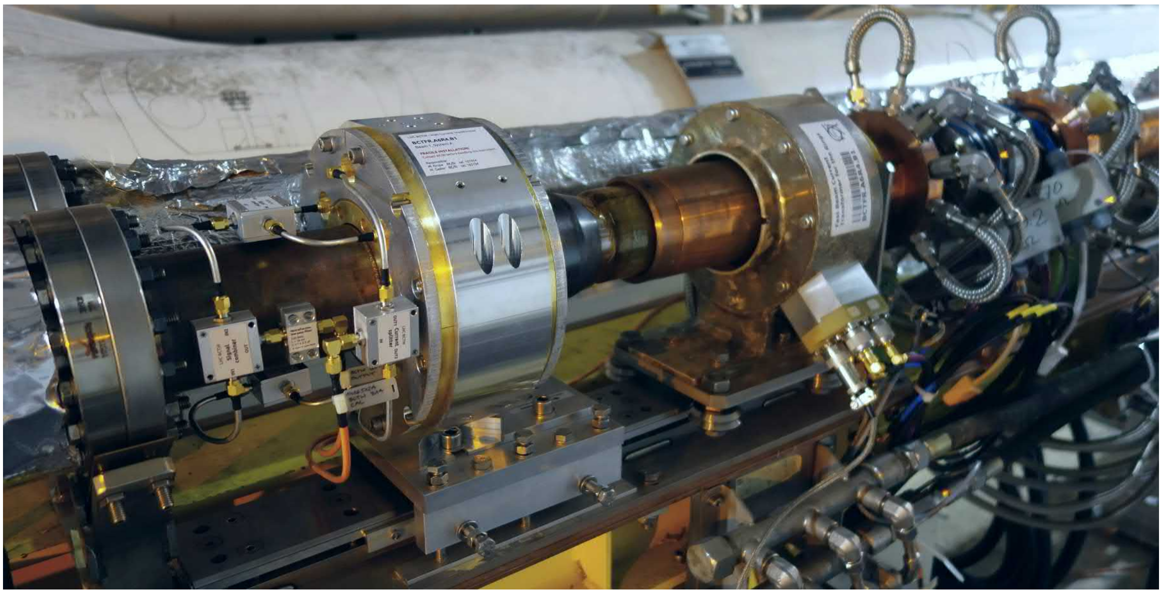

Figure 4.21: WCT R1A installed in the measurement position with the FBCT R1A displaced to the parking position. The intricate water-cooling circuit for protecting the FBCT and ICT during high-temperature treatment of the vacuum chamber can be seen behind the FBCT.

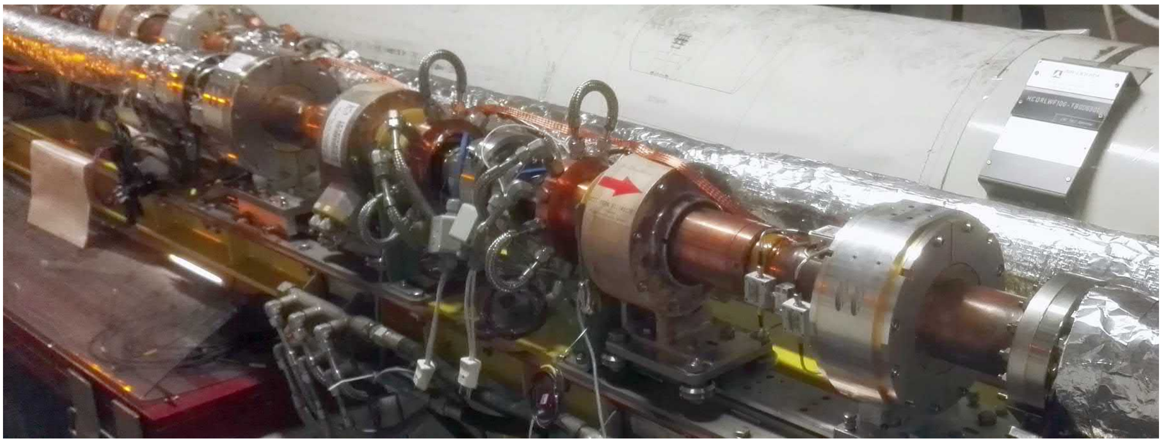

Figure 4.22: WCT R1B installed in the measurement position with the ICT R1B displaced.

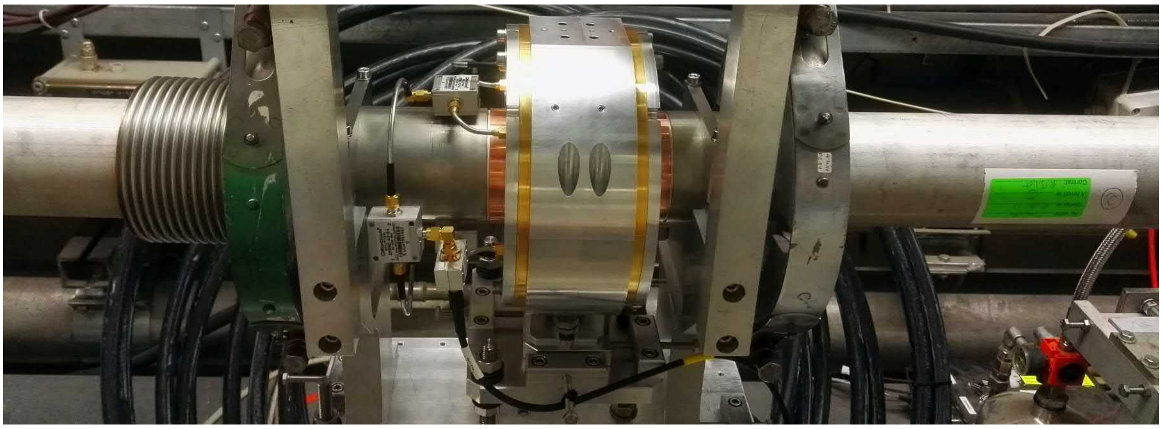

Figure 4.23: WCT installed in the SPS accelerator.

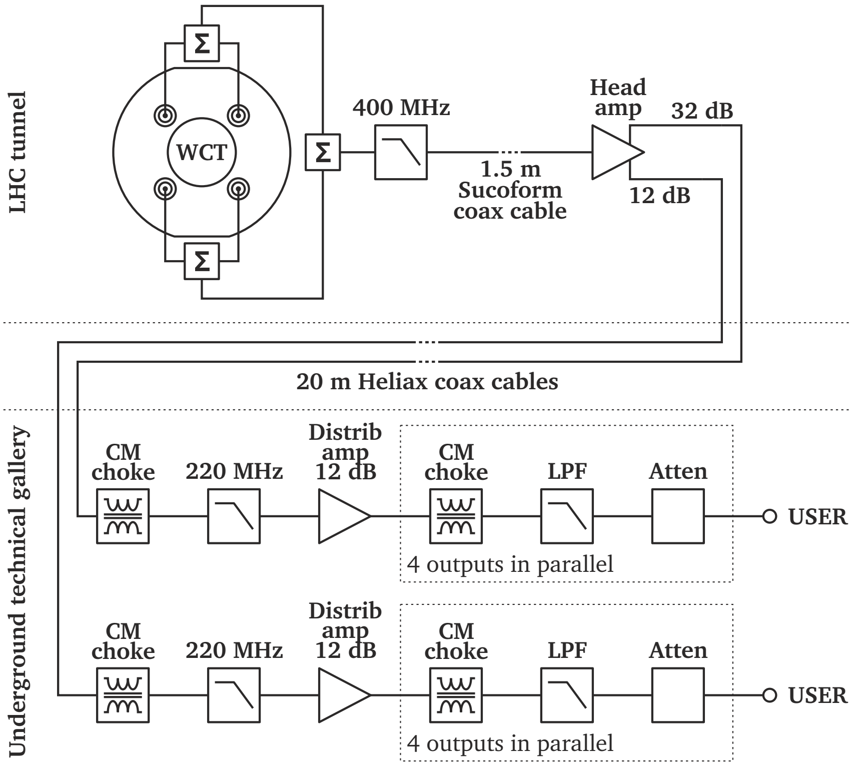

Figure 4.24: The front-end electronics connections for each installed LHC WCT.

Figure 4.25: Common-mode chokes and 200 MHz low-pass filters installed at the end of the Heliax coaxial cables before the distribution amplifier.

Figure 4.26: Distribution amplifier and a box common-mode chokes installed in a 19-inch rack.

Figure 4.27: 19-inch racks hosting the WCT, FBCT and ICT acquisition electronics.

4.3 Beam intensity measurements

With the three bunch intensity monitors installed in the LHC simultaneously, it became possible to evaluate the WCT, FBCT, and ICT performance with a real particle beam. All sensors sent their signals to acquisition systems which continuously recorded the computed bunch intensities into the CERN Accelerator Logging Service. To avoid storing an excessive amount of data, the bunch intensities are averaged over one second before logging. For the same reasons, the central database does not routinely store raw digitised waveforms of the signals generated by bunch intensity monitors. However, an oscilloscope installed in the technical gallery could conveniently record the time-domain signals. A nearby rack hosted the same 12-bit instrument with 1 GHz analogue bandwidth as used for laboratory measurements. It allowed single-shot sampling of the monitors' outputs at 2.5 GSa/s and multi-shot acquisition up to 125 GSa/s using the RIS technique [69].

4.3.1 Time response to a single bunch

The most fundamental yet critical measurement to evaluate performance of any bunch intensity monitor is the time-domain signal it generates with a single particle bunch circulating in the accelerator. The signal's amplitude and shape must be well adapted for the foreseen acquisition electronics and the signal duration should not exceed a given integration window. To reduce the noise level, an oscilloscope averaging 100 consecutive acquisition recorded the WCT, FBCT and ICT outputs.

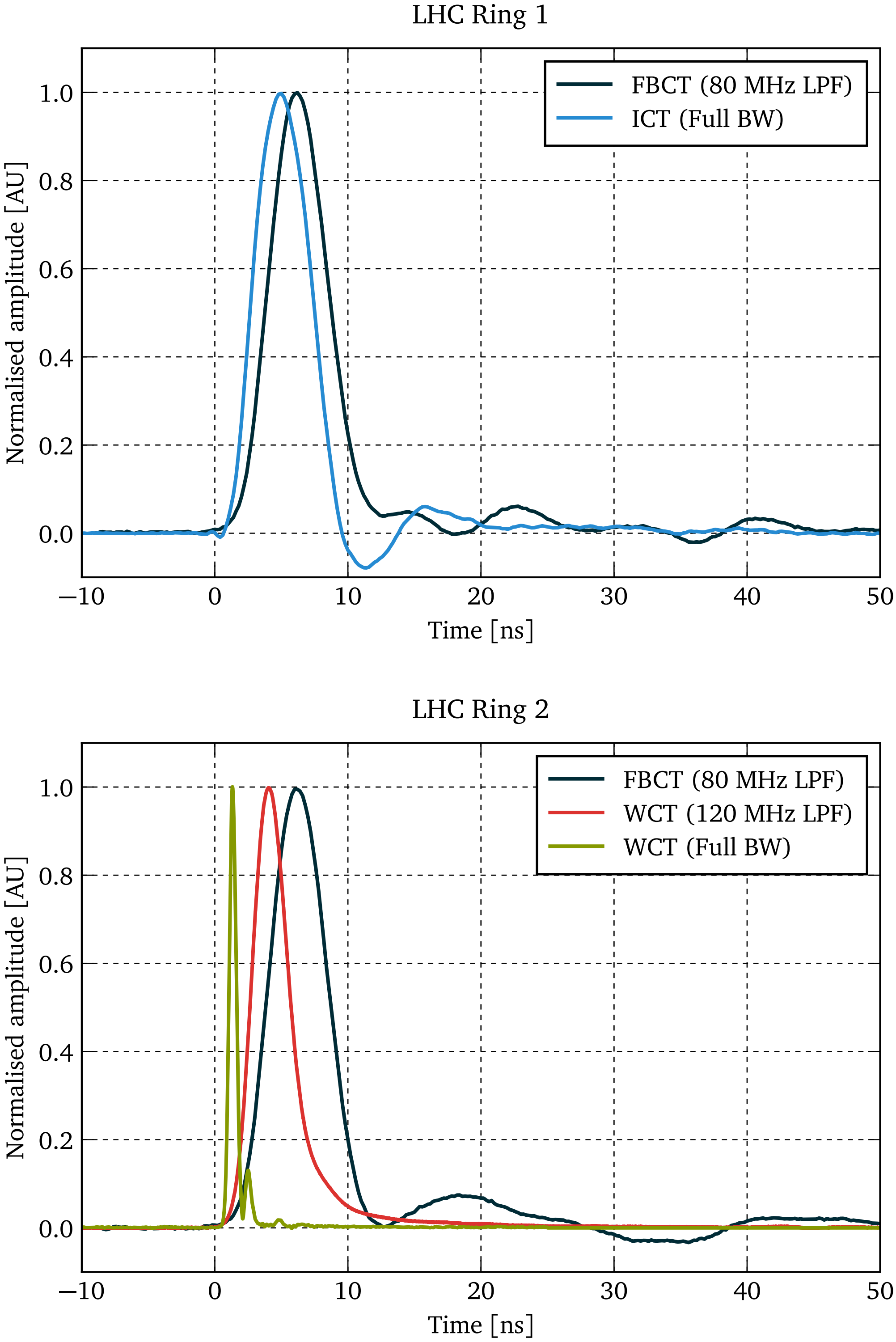

Figure 4.28: Amplitude-normalised time response of the FBCTs, the ICT, and the WCT to a nominal LHC bunch, measured with beam.

Figure 4.28 shows the amplitude-normalised time response of the FBCTs, the ICT, and the WCT to a nominal LHC bunch measured with beam during the 2015 commissioning period. Both FBCTs were equipped with analogue 70 MHz low-pass filters which had been installed since July 2011 to limit the beam-position and bunch-length sensitivity of the monitors [46]. No external filters altered the ICT signal. The WCT response was measured in two configurations: unfiltered full bandwidth and through a 120 MHz non-reflective low-pass filter. For technical reasons, the curves shown in Fig. 4.28 were not recorded at the same time but with different beams in virtually identical conditions: beam energy of 450 GeV, bunch intensity of 1.1×10^{11} protons, and bunch length of 1.2 ns.

The responses of the FBCTs installed on the two LHC rings are plotted in black. Both instruments generated a main pulse of about 12 ns followed by a tail extending over some 40 ns. Interestingly, even though the two FBCTs are the exact same model, the tails in each case look drastically different making them somewhat difficult to correct.

Similarly to the FBCT, the ICT's response, plotted in blue, consists of a main pulse followed by a tail. However, in this case the duration of both signal components is shorter – the main pulse is about 10 ns long with the tail lasting some additional 20 ns.

The low-pass filtered variant of the WCT, shown in red, produced a single pulse filling almost the entirety of the available 25 ns bunch window, leaving about 2 ns of baseline following the pulse. On the other hand, the unfiltered WCT response, represented in green, is a pulse mirroring the longitudinal structure of the bunch followed by a 1 ns reflection at a 10 % level. The author believes that the reflected pulse originates within the internal PCBs and is a result of an imperfect way the individual RF transformer signals are summed. As the WCT initial specification did not call for operating the monitor in a full-bandwidth configuration, the author performed no optimisation to mitigate this reflection due to the limited development time available.

Among the three kinds of tested instruments, only the WCT's response fulfils the maximum output pulse length requirement of the LHC bunch intensity measurement system. The responses of the FBCTs and the ICT extend over 25 ns after which time another bunch could be present. In such a case there would be a non-negligible "leakage" of the signal which, in turn, would compromise accuracy of the intensity measurements of the following bunch.

The unfiltered WCT response is short enough to be easily shaped with external low-pass filters. Typically, this is a desirable feature for bunch intensity monitors as it makes the output pulse shape easily adjustable for the particular front-end electronics and acquisition system used.

With some very encouraging measurements of the unfiltered WCT, the author decided to compare its performance with the monitors designed for diagnostics of the longitudinal bunch parameters. In the LHC this functionality is provided by a Wall Current Monitor (WCM)[1] [30]. Figure 4.29 shows the results of this comparison. The data were obtained during the 2015 LHC beam commissioning period with a nominal LHC bunch with intensity of 1.1×10^{11} protons, bunch length of 1.2 ns, and energy of 450 GeV.

The WCM response was measured in two configurations: the operational "summed outputs" mode, as well as the improved "single output" mode highly optimised for special longitudinal diagnostics at the expense of increased beam position sensitivity of the monitor. For this meas-

---

[1] In the LHC the WCM is often referred to by its internally attributed equipment code - APWL.

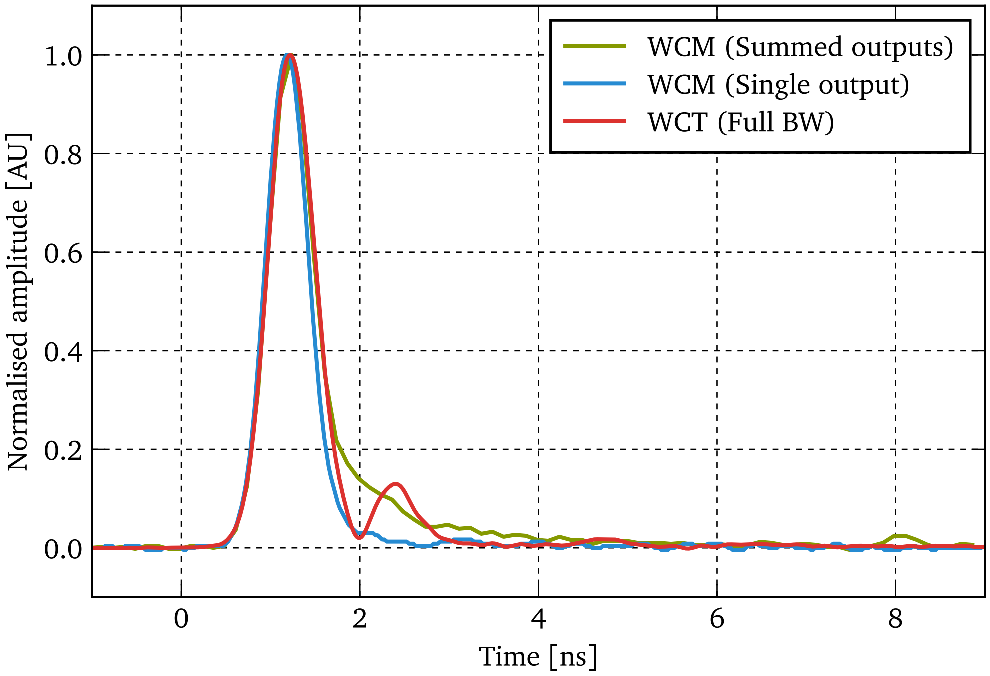

Figure 4.29: Normalised time response of the WCM and the WCT to a nominal LHC bunch.

urement, the author removed the WCT's front-end electronics, including all low-pass filters, and reduced the cabling to the necessary minimum.

All three curves are similar, with notable differences only at the pulses' falling edges. All instruments exhibited virtually identical rise time with the optimised "single output" WCM, plotted in blue, having slightly shorter Full Width at Half Maximum (FWHM) and showing practically no perturbation at the pulse's tail. The output pulse of the more conventional "summed outputs" WCM, shown in green, has a rather long tail stretching over some additional 2 ns. The WCT response, plotted in red, accurately follows the "summed outputs" WCM response without the latter's tail. However, a 10 % 1 ns reflection impairs the WCT output pulse quality.

Regarding longitudinal bunch diagnostics, the above test clearly proves that the WCT has potential to become a viable alternative to more commonly used WCMs for LHC-like bunches. Clearly, additional work would be required to match the performance of the optimised "single output" variant of the WCM. Nevertheless, one can assess the first longitudinal measurements performed with the WCT as promising.

4.3.2 Signal levels

Nominal bunches colliding in the LHC consist of around 1.2×10^{11} protons each. For safety reasons, the very first bunch injected into the accelerator, often referred to as a pilot bunch, contains many fewer particles, in the order of 5×10^9 protons. The WCT must efficiently measure a wide range of image current levels. To improve the measurement accuracy for small signals, the analogue front-end electronics splits the sensor's output between two parallel channels amplifying the signal with either high or low gain.

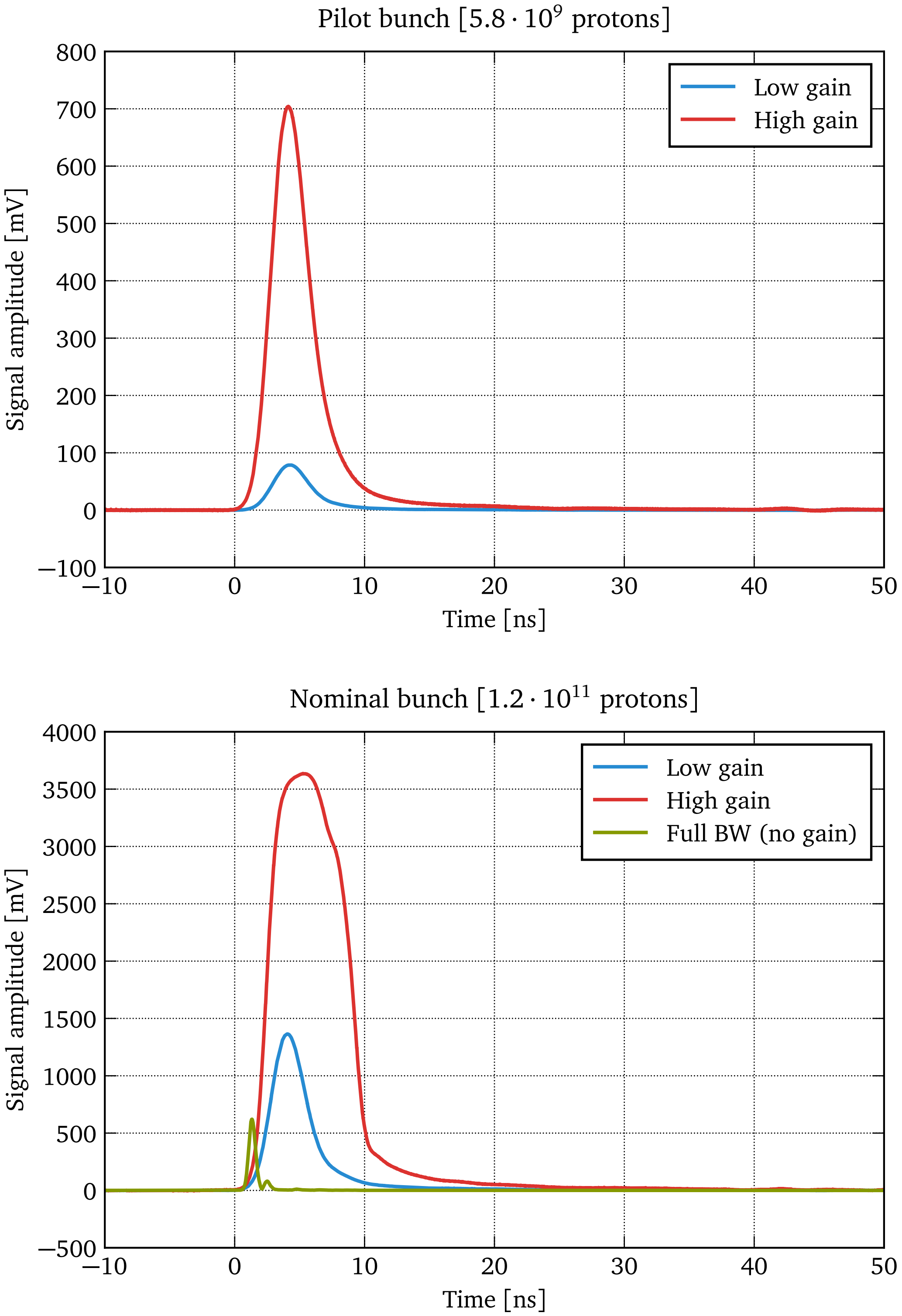

Figure 4.30: Time response of the WCT with its front-end electronics to a pilot and a nominal LHC bunch measured with beam during the 2015 commissioning period.

In the high gain channel, a low-intensity bunch (5×10^9 protons) produces a signal filling approximately 25 % of the front-end electronics linear dynamic range of 2.7 V. On the other hand, the low gain channel is around ten times less sensitive, i.e. it produces signals covering approximately 50 % dynamic range for a high intensity bunch (1×10^{11} protons).

Figure 4.30 shows the WCT's analogue front-end electronics outputs with typical pilot and nominal bunches circulating in the LHC. For comparison, the signal the WCT generates without any amplifications nor filtering is shown in the bottom plot in green (labelled as "Full BW").

To obtain some intuitive feeling about the WCT's sensitivity, it might be convenient to establish scaling factors translating the peak output voltage into an approximate number of particles seen by the sensor. The high-gain channel produced the peak voltage of 702 mV for a bunch of 5.8×10^9 protons. Thus, this channel's peak output voltage sensitivity is 8.3×10^6 protons/mV. The same exercise for the low gain channel yields a sensitivity of 8.8×10^7 protons/mV. Due to the front-end electronics' limited dynamic range, for high-intensity bunches, the high gain channel saturates at just over 3.5 V making it unreliable for measuring bunches containing more than approximately 3×10^{10} protons.

The measured peak voltage values are around 30 % lower than what would be expected based on the estimations presented in Tab. 3.2. These additional losses, not taken into account when calculating the signal levels, are due to the long cables connecting the WCT head amplifier installed in the LHC tunnel with the distribution amplifier located some 10 m away.

The peak output voltage discussed above is important primarily to essure that the front-end electronics output signal matches the acquisition electronics' dynamic range. To obtain the bunch intensity, the signals must be integrated as described in section 2.1.4. The analogue front-end electronics besides amplifying signals also "stretches" it with appropriate low-pass filters to maximally use the available acquisition time window.

4.3.3 Beam position sensitivity

One of the main motivations for the WCT's development was the FBCT's sensitivity to the transverse beam position. In summer of 2015, the author benefited from a dedicated beam time to quantify performance of all LHC bunch intensity monitors [75]. The beam position sensitivity evaluation, conducted in parallel for the FBCTs, ICT, and WCT, used five nominal bunches of about 1.1×10^{11} protons each, with 1.3 ns average bunch length circulating in each LHC ring at an energy of 450 GeV. Hundreds of empty bunch slots separated the bunches to minimise the possible bunch-to-bunch signal leakage for the monitors with a response longer than 25 ns.

Once the beams were circulating in the LHC, a cross-calibration equalised the initial intensity reading of all the instruments. An additional magnetic field applied to the beam through a process called a 3-corrector orbit bump changed the beam position at the instruments' locations in eight consecutive steps:

1. Positive horizontal (H)[2]
2. Negative horizontal
3. Positive vertical (V)

---

[2] Per the LHC convention, the horizontal plane's positive direction points outside of the ring, regardless of the beam movement direction. For the vertical plane, the positive direction is always towards the top of the beam pipe.

4. Negative vertical
5. Positive horizontal with positive vertical (diagonal)
6. Negative horizontal with positive vertical (diagonal)
7. Positive horizontal with negative vertical (diagonal)
8. Negative horizontal with negative vertical (diagonal)

The beam remained for approximately 60 s at each programmed step after which it returned to its reference orbit for additional 60 s to allow measurements of the natural beam intensity decay. Due to the physical location of the tested monitors and limitations of the LHC magnets, it was not possible to provoke bumps of the same amplitude for both planes in both LHC rings. The beams moved by 1.5 mm to 3 mm. Linear interpolation was applied to calculate the exact beam offset at the location of each intensity monitor using the closest BPMs located 22 m to 25 m (anticlockwise) and 7 m to 10 m (clockwise) away.

Table 4.3 summarises the observed sensitivity of the beam intensity measurement to the transverse beam position. The table reports the ratio of the beam intensity measured with an orbit bump applied to the beam intensity measured during the previous zero-offset period and normalised to the unit of mm^{-1}.

Figure 4.31 demonstrates the evident correlation between the FBCT reading and the transverse beam position. During the measurements the FBCTs were equipped with 70 MHz low-pass filters used since 2011 to reduce the monitor's sensitivity to the beam position [46]. The measured beam position sensitivity of $1.4 \times 10^{-3}\,\text{mm}^{-1}$ to $8.2 \times 10^{-3}\,\text{mm}^{-1}$ is in fact already about 10 times lower than what had been originally observed during the 2010 LHC commissioning campaign [17]. The relatively large difference in both planes, especially in Ring 1, has been speculated to originate from the inherently asymmetrical winding featuring only a single connector. This, however, has not been formally proven as of writing this thesis.

With its limited bandwidth, the ICT performed much better than the FBCT. Nevertheless, it exhibited some residual beam position sensitivity at the level of up to $0.2 \times 10^{-3}\,\text{mm}^{-1}$. As for the FBCT, the intrinsic monitor's asymmetry has been hypothesized as the root cause. It must be noted that the ICT was below the limit of $1 \times 10^{-3}\,\text{mm}^{-1}$ specified for LHC bunch intensity monitor's beam position sensitivity. The measurements presented in this section are reported for the reader's curiosity.

With a detection limit of $0.05 \times 10^{-3}\,\text{mm}^{-1}$, the WCT was the only LHC bunch intensity monitor which did not exhibit any beam position sensitivity. This proves that regardless of splitting the image current into eight components measured by independent RF transformers, recombination of the intermediate signals does not introduce any unwanted asymmetries.

Table 4.3: Estimated beam position sensitivity of the LHC bunch intensity monitors

	Position sensitivity (upper bound) $[\text{mm}^{-1}]$			
Plane	FBCT Ring 1	FBCT Ring 2	ICT	WCT
Horizontal	6.5×10^{-3}	5.1×10^{-3}	0.2×10^{-3}	$< 0.05 \times 10^{-3}$
Vertical	1.4×10^{-3}	8.2×10^{-3}	0.1×10^{-3}	$< 0.05 \times 10^{-3}$

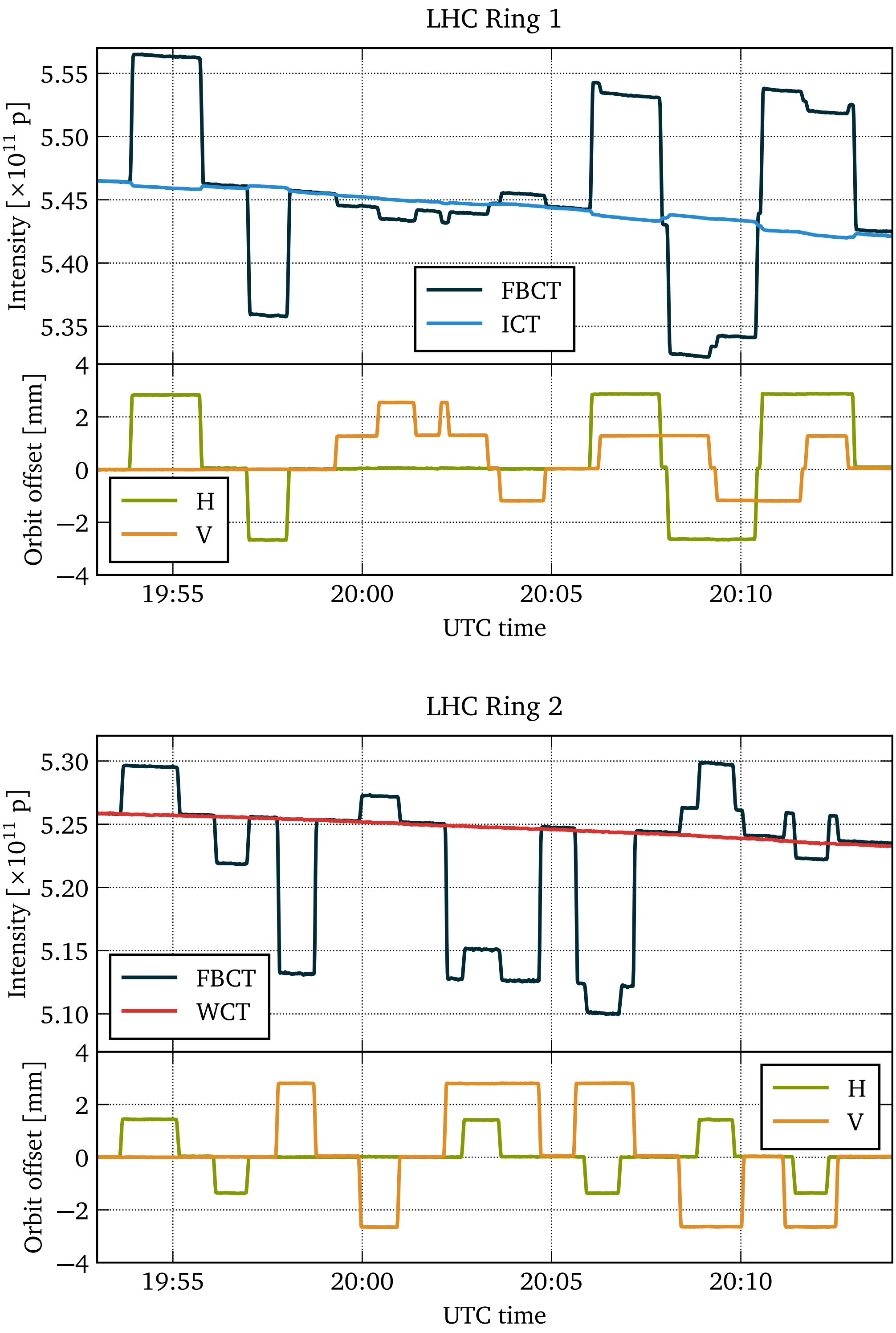

Figure 4.31: Beam position sensitivity measured for the FBCTs, the ICT and the WCT during a dedicated beam time (LHC fill 4022).

4.3.4 Bunch length sensitivity

The WCT addresses not only the FBCT's beam position sensitivity but also its bunch length sensitivity observed during 2010 LHC commissioning [17]. As a bunch gets shorter, its spectrum contains more power at high frequencies. For monitors exhibiting resonances, such as the FBCT as shown in section 4.1.6, the extra power amplifies the oscillation trailing the output pulse which affects the signal integration process. A deliberate reduction of the monitor's bandwidth, as done for the FBCTs in 2011 [46], can mitigate this detrimental effect.

The author quantified the FBCT, ICT, and WCT bunch lenght sensitivity using the same beams which served for the beam position sensitivity studies, i.e. five nominal bunches of about 1.1×10^{11} protons each at an energy of 450 GeV. The bunch length was controlled through adjusting the voltage applied to the accelerating RF cavities over the range of 3 MV to 14 MV starting at 6 MV corresponding to a bunch length of 1.32 ns. A step of 1 MV shortens the bunch by approximately 50 ps when the voltage increases or elongates it by the same amount when the voltage decreases. The studied bunch lengths spanned from 1.05 ns up to 1.5 ns covering the entire range used in regular LHC operation.

For the sake of clarity, a cross-calibration of all monitors resulted in coherent readings at the beginning of the procedure. The LHC Beam Quality Monitor (BQM), regularly used for this purpose, measured the bunch lengths. Table 4.4 summarises the measured bunch length sensitivity of the tested sensors, computed as the ratio of the beam intensity measured with the given bunch length, to the initial beam intensity measured before adjusting the RF cavities. The calculated values are in the unit of ns^{-1}. With the very small bunch length sensitivity observed for all tested instruments, the reported values should be considered only as indicative.

Figure 4.32 shows that with the detection limit of $2 \times 10^{-3}\,\mathrm{mm}^{-1}$ neither the FBCT nor the ICT displayed any sensitivity to the bunch length. The WCT readings, on the other hand, were unexpectedly correlated with the bunch length at the level of $5 \times 10^{-3}\,\mathrm{mm}^{-1}$. The author studied the source of this dependency in the laboratory and proved that it originated not from the sensors itself but rather from non-linearities in the front-end electronics caused by a limited slew-rate. The author solved this issue by redistributing the gain among the head-amplifier stages. Three months after the original tests, another WCT bunch length sensitivity measurements with beam took place. Figure 4.33 demonstrates that the unwanted sensitivity completely vanished and the WCT is as insensitive to the bunch length as the other two monitors.

During a regular LHC collision cycle, the bunch length naturally decreases by approximately 300 ps. A bunch length sensitivity of below $2 \times 10^{-3}\,\mathrm{ns}^{-1}$, observed for all three monitors, translates to a negligible measurement error of under 0.06 %.

Table 4.4: Estimated bunch length sensitivity of the LHC bunch intensity monitors

Bunch length sensitivity (upper bound) [ns^{-1}]				
FBCT Ring 1	FBCT Ring 2	ICT	WCT	WCT (MD2)
$< 2 \times 10^{-3}$	$< 2 \times 10^{-3}$	$< 2 \times 10^{-3}$	5×10^{-3}	$< 2 \times 10^{-3}$

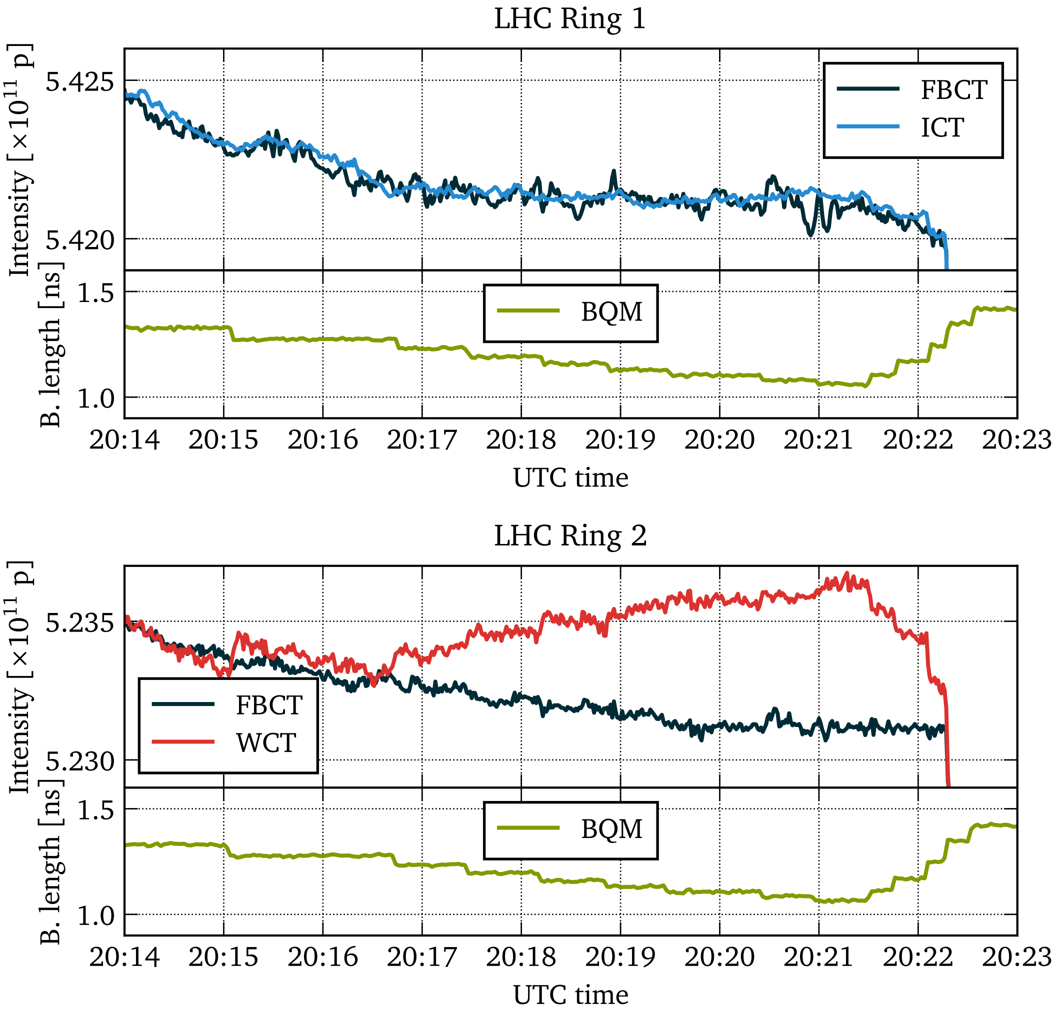

Figure 4.32: Bunch length sensitivity measured for the FBCTs, the ICT, and the WCT during dedicated beam time (LHC fill 4022).

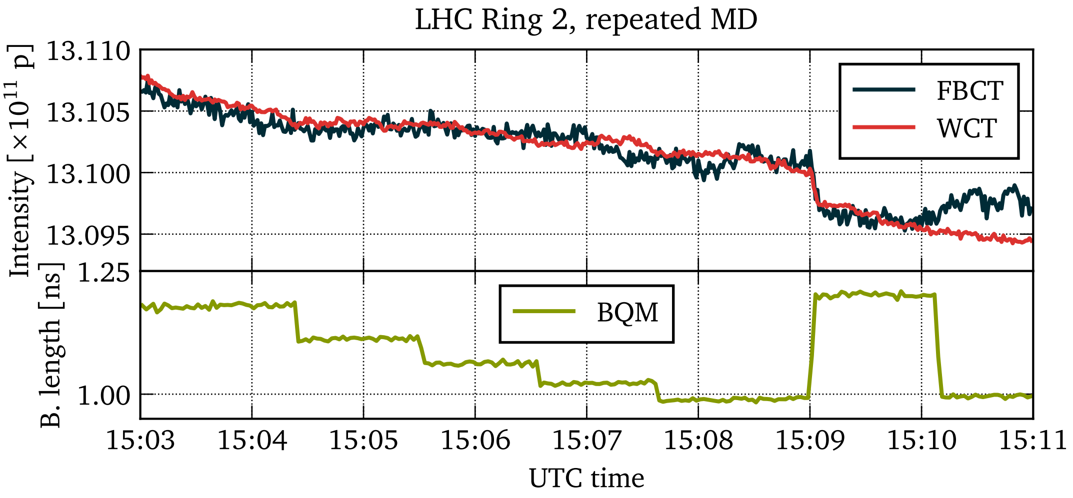

Figure 4.33: Bunch length sensitivity measured for the FBCT, and the WCT during dedicated beam time (LHC fill 4547).

4.3.5 Special cases

This section discusses measurements obtained with the WCT and, where appropriate, other sensors during special accelerator conditions. Although the author did not explicitly optimise the WCT for each of the discussed scenarios, physicists generally expect reliable bunch intensity measurements to be available under any circumstances. Those special cases served to quantify any potential performance limitations of the WCT.

Satellite bunches

Very low intensity satellite bunches occur due to the acceleration system imperfections. They can occupy any RF bucket not taken up by one of the main bunches and in the LHC their intensity typically does not exceed 0.5 % of the nominal bunch population. Above a certain intensity threshold the satellite bunches compromise the safety of some accelerator components, and in LHC dedicated instrumentation continuously monitors their population and can autonomously request an emergency beam ejection before the unsafe threshold is exceeded.

The LHC features the Longitudinal Density Monitor (LDM), a single-photon counting sensor of synchrotron radiation [43]. With a temporal resolution of 50 ps and a high dynamic range exceeding 1×10^5 (achieved due to minutes-long integration time), the LDM surpasses satellite bunch measurement capabilities of any monitor based on current transformers. Nevertheless, the authored deemed it interesting to verify if the WCT is sensitive enough to observe the satellite bunches even if it could not match the LDM performance.

A 12-bit oscilloscope with 1 GHz analogue bandwidth sampling at 2.5 GSa/s, with a 120 MHz low-pass filter installed at its input, recorded the WCT front-end electronics "high gain" channel described previously in section 3.4. To improve the signal-to-noise ratio, each waveform is an average of 500 consecutive acquisitions. The LDM data come from the CERN Accelerator Logging System. For the sake of readability, the signals of both monitors were rescaled such that the highest intensity bunch has an amplitude of 1.

Figures 4.34 and 4.35 compare satellite bunch measurements obtained with the LDM and the WCT. There exists an explicit correlation between the signals provided by both instruments. However, the outstanding temporal resolution of the LDM is evident with each individual satellite bunch being easily distinguishable. Due to the insufficient bandwidth, the WCT signal corrupts measurements of the subsequent satellite bunches spaced by 5 ns. The WCT high-gain channel typically measures only low intensity bunches and the front-end electronics saturate in presence of nominal bunches. As a consequence, the amplifiers require a certain recovery time to provide reliable measurements after being saturated. Figure 4.35 demonstrates that the four satellite bunches preceding the high-intensity train are clearly recognisable whilst the four succeeding ones are overshadowed by a long tail.

Qualitatively, the WCT can coarsely observe the satellite bunches in certain situations but deriving their intensity from the waveforms does not seem feasible. The dynamic range and temporal resolution required for such measurements are orders of magnitude greater than what the WCT can achieve. Nevertheless, the monitor can serve to cross-verify the LDM measurements in case the latter presents any issues.

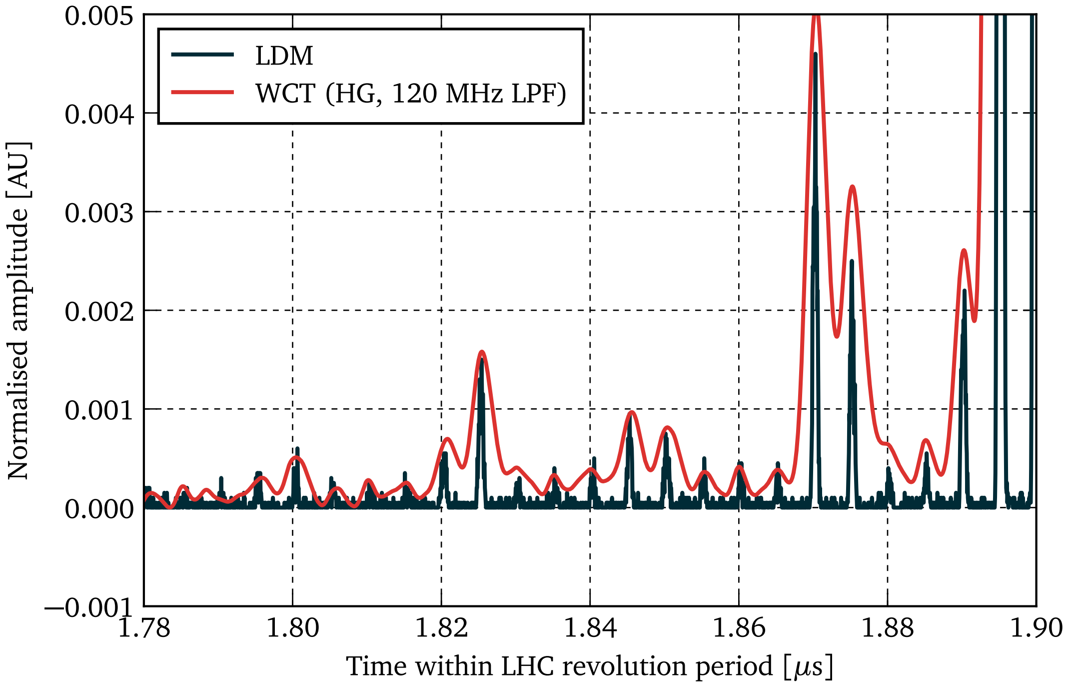

Figure 4.34: Comparison of satellite bunch measurements with the LDM and the WCT during the LHC fill 4569.

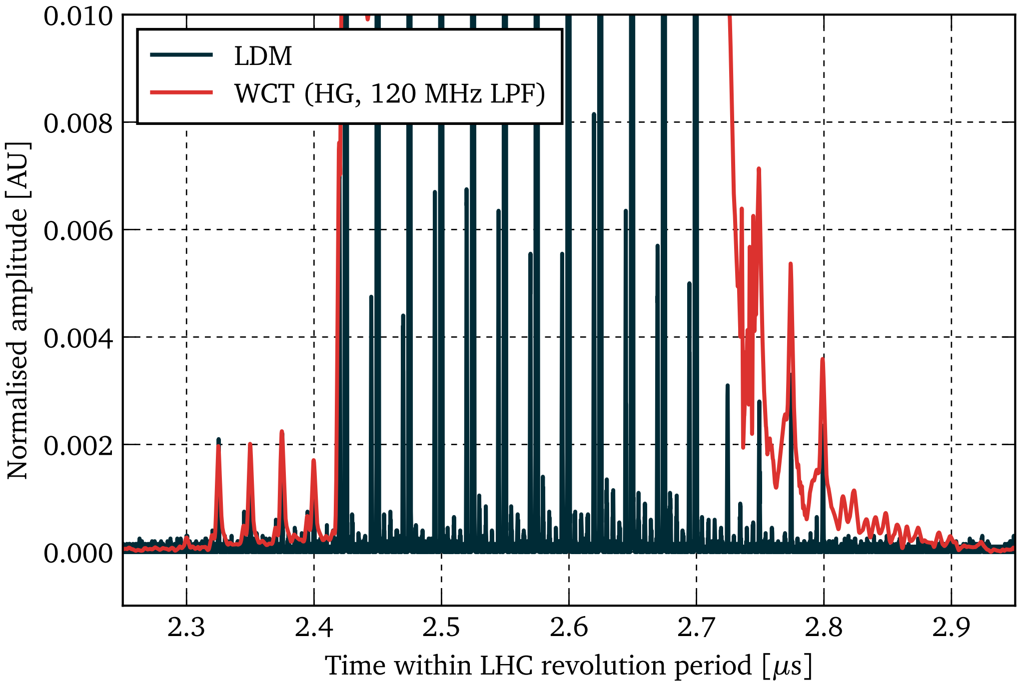

Figure 4.35: Comparison of high-intensity beam recovery time between the LDM and the WCT during the LHC fill 4640.

Doublet bunches

The so-called doublet bunches proved to be extremely effective at conditioning the inner surfaces of the LHC vacuum chambers preparing the accelerator for a smooth operation with high-intensity beams [76]. They consist of a pair of bunches (often called bunchlets) 5 ns apart, with each pair spaced by the regular 25 ns LHC bunch repetition period.

The usage of doublet bunches is very rare and never for high energy collisions. Their intensity measurement accuracy requirements are less demanding than for the nominal conditions and in principle no dedicated instrumentation is required to monitor the doublet bunches. However, coarse measurements are important for safety and operational reasons under any accelerator conditions and the author tested the WCT performance with doublets as their observation with limited accuracy is one of the functionalities provided by the old FBCTs.

Figure 4.36 shows a train of nine doublet bunches measured using the WCT's "low gain" channel, in the standard configuration, connected to a 12-bit oscilloscope with 1 GHz analogue bandwidth sampling at 2.5 GSa/s.

Each of the two bunchlets making up a doublet pair is clearly distinguishable. However, signal leakage from the first to the second bunchlet is evident as the waveform does not reach the baseline between the two bunchlets. Due to the lack of other instrumentation configured for intensity measurements of the individual bunchlets at the time, it is not possible to precisely quantify the WCT measurement error. Based on the waveform shape obtained with individual bunches and on the signal level between the two bunchlets, the author estimates that approximately 5 % of the first bunchlet integral leaks into the subsequent bunchlet.

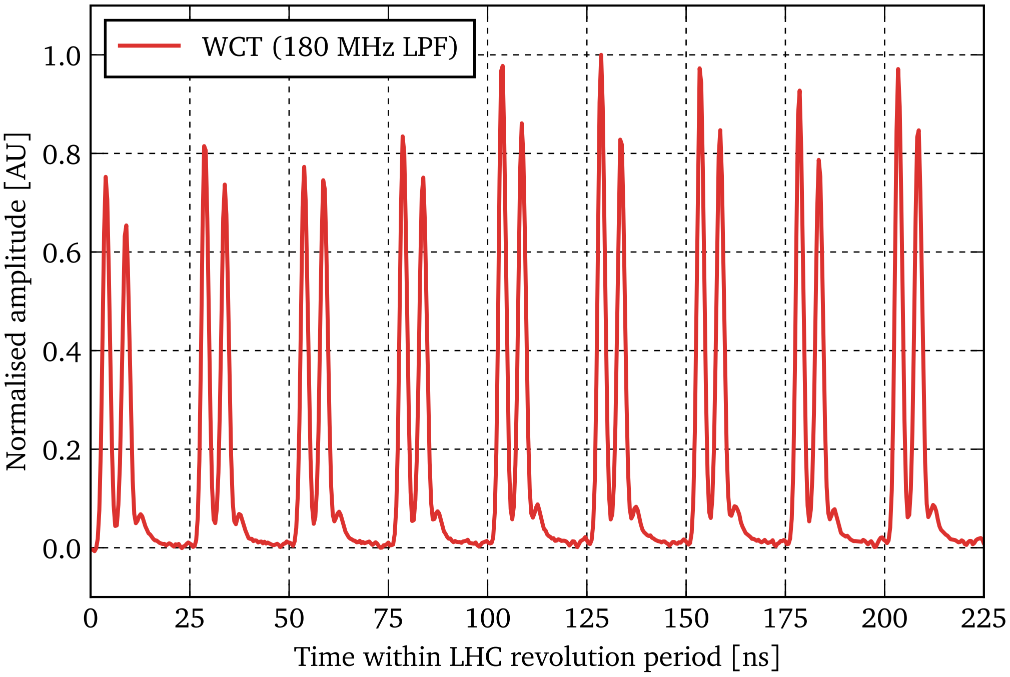

Figure 4.36: Time domain response of the WCT with a low-pass filter to doublet bunches.

Energy ramp

The process of accelerating the LHC beam from the injection energy of 450 GeV up to 6.5 TeV in collisions takes about 20 min. As the beam energy ramps up, some bunch parameters change and can potentially influence the accuracy of bunch intensity measurements. Due to the sophisticated nature of the LHC acceleration process [77], bunches change their longitudinal shapes, transverse positions, and profiles. Moreover, the bunch spacing also decreases by around 0.7 ps leading to the revolution period shortening by some 2.5 ns.

During the beam injection into the LHC, not all particles are captured into RF buckets to form bunches. These unbunched charges contribute to the DC beam current but are invisible to bunch intensity monitors such as the FBCT and WCT. The DCCT, sensitive also to unbunched particles, often reports the total beam intensity higher than the sum of individual bunches. As the acceleration starts, the LHC beam collimation system removes all unbunched particles from the machine and only the bunched charges remain circulating.

Since the LHC beams are routinely accelerated, it was not necessary to request a dedicated beam time to compare the FBCT and WCT measurements to those of the DCCT providing the absolute reference value of the beam current. A cross-calibration of the three instruments to report the same reading one second after the beginning of the acceleration process accounted for the unbunched beam seen by the DCCT prior to the energy ramp.

Figure 4.37 demonstrates an excellent agreement between the DCCT and WCT measurements through the entire acceleration process. Conversely, the FBCT readings quickly deviate and the monitor underestimates the beam current by approximately 0.25 %. This error originates most likely in an improper phasing of the analogue integrators, as explained in section 2.3.3.

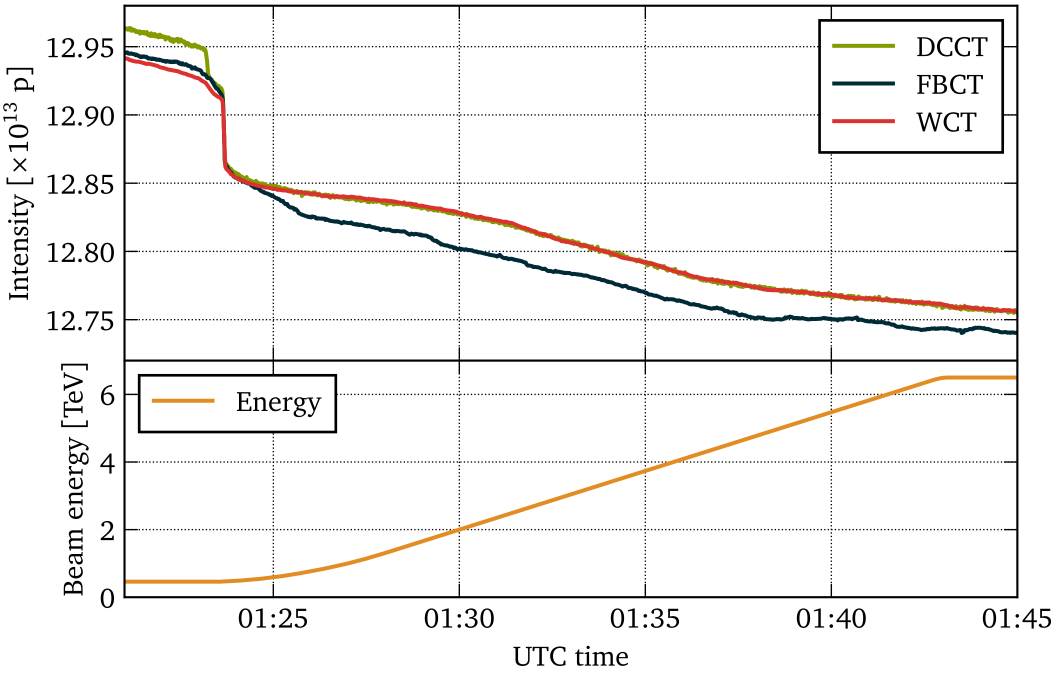

Figure 4.37: Beam intensity measured by the DCCT, the FBCT, and the WCT during the energy ramp-up procedure (LHC fill 4410).

Chromaticity measurements

In synchrotron particle accelerators, chromaticity links the beam's transverse oscillation frequency and its momentum. It must be precisely controlled not to amplify any instabilities which could lead to excessive particle motion and beam loss [78].

In many accelerator facilities, chromaticity is calculated by varying the beam's energy and measuring the resulting change in the transverse oscillation frequency. The usually applied method is a modulation of the RF frequency whilst maintaining constant fields in all magnets. As a side-effect, the modulation also affects the beam position in the horizontal plane.

In the LHC, chromaticity measurements by RF modulations are routinely performed before the beam is accelerated. For bunch intensity monitors which are sensitive to the beam position, one can expect a reduction of accuracy while the RF frequency is being modulated. Therefore, the author investigated the WCT performance during chromaticity measurements.

Figure 4.38 compares the pilot bunch intensity measurements obtained with the FBCT and WCT as the 400 MHz RF frequency undergoes a sinusoidal modulation. It's worth noting for the bottom subplot that the modulation depth was in the order of 1×10^{-7}.

The FBCT measurements are clearly correlated with the RF frequency change, which is at least partially caused by the varying horizontal beam position as explained earlier. On the other hand, the WCT exhibits no such behaviour, once again demonstrating that the monitor does not suffer from unwanted sensitivity to the beam position as discussed previously in section 4.3.3.

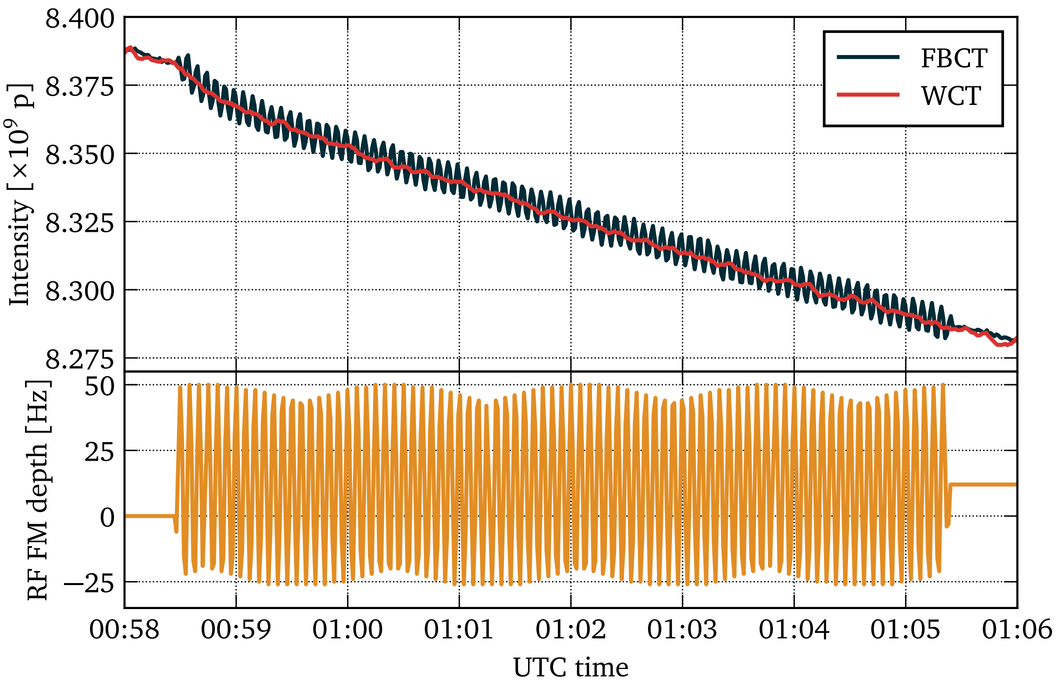

Figure 4.38: Beam intensity measured by the FBCT and the WCT during measurements of the beam chromaticity by modulation of the RF frequency (LHC fill 4038).

Orbit corrections

Minimising beam position sensitivity of the LHC bunch intensity monitors is important to improve the measurement quality, not only in special accelerator conditions, but also during its regular operation. Albeit the beam position at the FBCT and WCT typically remains rather constant throughout the entire accelerator cycle, in some situations it can change. The LHC is equipped with a sophisticated orbit feedback system, which can autonomously steer the beam to protect the accelerator from undesired particle losses or preserve luminosity in collisions [79].

Beam position changes induced by the LHC orbit feedback cannot be easily predicted due to the vast complexity of the system. However, one can later identify them through analysis of the Beam Position Monitors readings. Figure 4.39 shows a 30 min-long period during which the beam moved horizontally (H) and vertically (V) by a few hundreds of micrometres. The author interpolated the beam position at the FBCT and WCT location from measurements of the nearby BPMs and and offset it to initially equal 0. The correlation between the FBCT measurements and the transverse beam position is evident and coherent with the values reported earlier in section 4.3.3. The WCT shows no such dependence, reaffirming the monitor's insensitivity to the beam position.

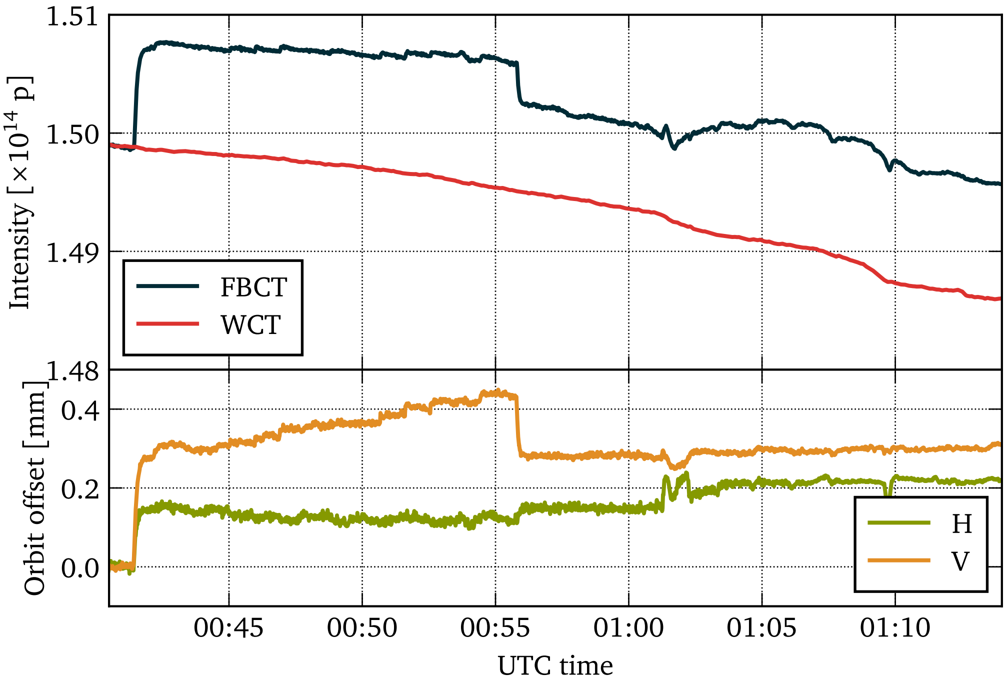

Figure 4.39: Beam intensity measured by the FBCT and the WCT during the beam orbit correction procedure (LHC fill 4640).

BSRT calibration

The LHC is equipped with an array of instruments measuring the transverse distribution of particles, typically called simply the beam profile. Its continuous monitoring is critical to ensure the required number of particle collisions as well as for the accelerator's safety. One of the LHC beam profile monitors is the Beam Synchrotron Radiation Telescope (BSRT) which intercepts the synchrotron light emitted when superconducting magnets bend the beam's trajectory. The BSRT calibration procedure, done a few times per year, requires transversely displacing the beam to measure the imaging system's magnification to convert camera pixel size into physical size at the object (beam) plane [80]. Since the BSRT is in the vicinity of the FBCT and WCT, the bunch intensity monitors also see the orbit bumps introduced to calibrate the BSRT.

As demonstrated throughout the chapter, the FBCT is sensitive to variation of the transverse beam position. This shortcoming manifests itself also during the BSRT calibration procedure when the beam moves by up to 3 mm at the location of the intensity monitors. The bottom part of Figure 4.40 shows the horizontal (H) and vertical (V) beam position at the location of the FBCT and WCT during BSRT calibration while the top part shows the intensity of a single nominal bunch as reported by both monitors. Once again the FBCT measurement is clearly correlated with the beam position while the WCT shows no such dependence. The observed beam position sensitivity of the FBCT is in line with the values reported earlier in section 4.3.3.

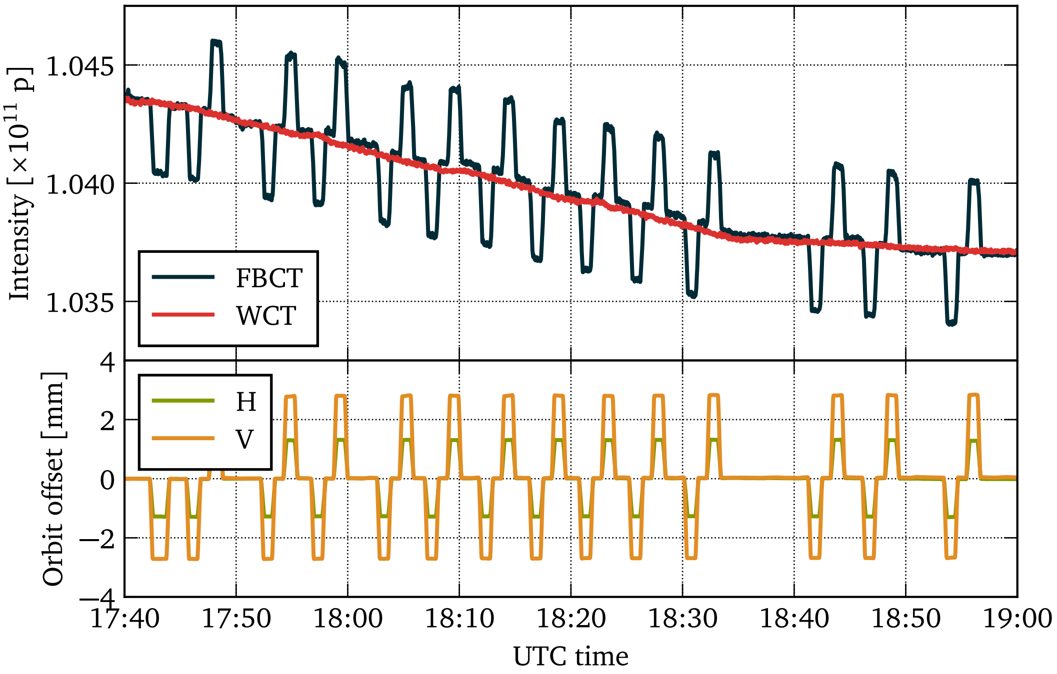

Figure 4.40: Beam intensity measured by the FBCT and the WCT during the BSRT calibration procedure (LHC fill 4513).

Chapter 5

Conclusions and outlook

5.1 Final conclusions

The WCT development took place to address the FBCT performance limitations discovered during the LHC Run 1 between 2010 and 2013. The original LHC bunch intensity monitor displayed an unwanted sensitivity to the transverse beam position and bunch length. Moreover, its output pulse was too long to fit into a 25 ns integration window required for bunch-by-bunch acquisition, leading to a non-negligible signal leakage into the subsequent bunch slots.

The WCT relies on a non-intercepting observation of a particle beam which does not disturb it in any considerable way. Rather than directly coupling to the beam's electromagnetic field, the developed WCT uses the image current induced on conductive walls of the LHC vacuum chamber to monitor bunch intensity. Eight small RF transformers, distributed azimuthally around the vacuum chamber with a dielectric insert, pick up the image current split into eight branches. The combination of the transformers' output signals is proportional to the instantaneous bunch current while being independent of the transverse beam position. Large ferrite cores and an RF bypass adjust the sensor's bandwidth to minimise the error after the signal is integrated to compute bunch intensity. Before integration, the WCT's output signal is shaped by custom designed non-reflective low-pass filters, and a set of amplifiers. The pulse shape and amplitude are well suited for precise integration over a 25 ns window using either analogue integrators or modern digitizers. The sensor's mechanical design allowed it to be installed in the location previously occupied by the FBCT without the need of opening the LHC vacuum chamber.

In parallel to the WCT designed fully at CERN, the industrial supplier who provided the original FBCTs worked on a new ICT with a low beam position sensitivity and a sufficiently short output pulse. The author extensively evaluated all three sensors first in laboratory and subsequently with a particle beam after their installation in the LHC accelerator tunnel.

The conducted tests clearly demonstrated WCT's superior performance over the other two devices. The WCT the only tested sensor generating an output signal not exceeding 25 ns in response to a bunch-like excitation. Moreover, unlike the other LHC bunch intensity monitors, it exhibited no measurable sensitivity to the transverse beam position. The WCT outperformed the FBCT and ICT also in terms of bandwidth and longitudinal beam-coupling impedance.

Following the successful beam measurement campaign, the WCT quickly superseded the other two sensors and it became the operational LHC bunch intensity monitor. Devices based on the same design have since been installed also in the second-largest CERN accelerator, the SPS. In the future, it is foreseen to replace the remaining LHC extraction lines FBCTs with WCTs based on the design described in this thesis.

Hence, the WCT described in detail throughout this dissertation fully satisfies the thesis statement formulated at the end of Chapter 2:

It is possible to design an electromagnetic sensor based on observation of the image current induced on the vacuum chamber wall for continuous, precise, and non-intercepting measurements of the LHC bunch intensity within a 25 ns window. The developed sensor can be compatible with the mechanical and operational constraints imposed by the LHC environment. It can also generate adequate signals for front-end electronics based on analogue integrators as well as an upgraded digital sampling acquisition system.

5.2 Applicability to other accelerators

Although the WCT has been optimised for relatively high-intensity proton bunches circulating in the LHC, one can adapt it to also serve other kinds of accelerators. The step-by-step design process introduced in Chapter 3 discusses in detail the electrical parameters interdependencies while Tab. 3.1 summarises the equation required to calculate the values of all components.

Given its small longitudinal beam-coupling impedance, i.e. a low amount of the passing beam's energy dissipated as heat, a WCT-like sensor could be potentially interesting for accelerator facilities dealing with high-power beams, such as spallation sources in which high-energy particles collide with stationary targets to produce a stream of neutrons. Section 4.1.8 demonstrated that the WCT's large ferrite cores successfully dampen electromagnetic resonances which would otherwise build up in the sensor's electromagnetically transparent body.

Another possible WCT application would be measurements of low-intensity bunches in compact medical accelerators where space is often extremely limited. A significant improvement of the sensor's sensitivity, defined in eq. 3.28, requires either reducing the number of RF transformers' secondary winding turns, or increasing the secondary-side resistance. Unfortunately, both of these actions deteriorate the monitor's low cut-off frequency, as shown by eq. 3.21, which must be taken into account when considering the WCT for low-intensity beams.

5.3 Further study potential

The work presented in this dissertation focused on a sensor optimised for precise bunch intensity measurements in the LHC. Despite that, the WCT signals are suitable to observe also other beam parameters, but additional work would be required to quantify the sensor's performance reach.

Sections 4.1.6 and 4.3.1 demonstrated that the WCT's output signal is not only short enough to comfortably fit within a 25 ns window, but it also closely resembles pulses generated by instruments optimised for monitoring of the longitudinal bunch profile. Nevertheless, the 10 % reflection following the WCT output pulse reduces the signal quality. An investigation into its origin with a particular focus on the internal PCB design is necessary before the WCT could be considered for longitudinal bunch diagnostics.

The WCT output signal exhibits no sensitivity over the transverse beam position, as demonstrated multiple times throughout section 4.3. The sensor's four intermediate outputs, on the other hand, are strongly correlated with the beam offset which was coarsely quantified in section 4.1.5. The WCT could thus serve as an integrated solution for bunch position and intensity monitoring whenever splitting these two functions between dedicated instruments is not practical. This would, however, require a significant front-end electronics modification to process the four intermediate outputs independently.

The small RF transformers of the WCT are equipped with an additional single-turn winding to calibrate the monitor with an external current pulse. The thesis author developed a proof-of-principle precise pulsed current source [81] but additional work is needed before the circuit can be used in regular LHC operation.

Bibliography

[1] R. W. Hamm and M. E. Hamm, “Introduction to the Beam Business,” in *Industrial Accelerators and Their Applications*, R. W. Hamm and M. E. Hamm, Eds. World Scientific, Jun. 2012, p. 2.

[2] R. Feynman, R. Leighton, and M. Sands, *The Feynman Lectures on Physics: Mainly Electromagnetism and Matter, Volume 2*. Addison-Wesley, Feb. 1977.

[3] S. Baird, “Accelerators for pedestrians,” CERN, Tech. Rep. AB-Note-2007-014, Feb. 2007.

[4] E. Todesco, “Magnetic Design of Superconducting Magnets,” in *CAS - CERN Accelerator School: Course on Superconductivity for Accelerators*, R. Bailey, Ed. CERN, May 2014, pp. 269–292.

[5] M. Vretenar, “Radio frequency for particle accelerators: evolution and anatomy of a technology,” in *CAS - CERN Accelerator School: RF for Accelerators*, R. Bailey, Ed. CERN, Jun. 2010, pp. 3–5.

[6] W. Herr and B. Muratori, “Concept of luminosity,” in *CAS - CERN Accelerator School: Intermediate Course on Accelerator Physics*, D. Brandt, Ed. CERN, Sep. 2003, p. 364.

[7] D. Möhl, “Sources of emittance growth,” in *CAS - CERN Accelerator School and KVI: Specialised CAS Course on Small Accelerators*, D. Brandt, Ed. CERN, Jun. 2005, p. 45.

[8] M. Gasior, R. Jones, T. Lefevre, H. Schmickler, and K. Wittenburg, “Introduction to Beam Instrumentation and Diagnostics,” in *CAS - CERN Accelerator School: Advanced Accelerator Physics Course*, W. Herr, Ed. CERN, Dec. 2014, pp. 23–60.

[9] About CERN. Accessed: 01 April 2020. [Online]. Available: http://home.cern/about

[10] E. Mobs. The CERN accelerator complex - August 2018. General Photo. [Online]. Available: https://cds.cern.ch/record/2636343

[11] L. Evans, *The Large Hadron Collider: a Marvel of Technology*. EPFL Press, Aug. 2009.

[12] J.-L. Caron. LHC Layout. General Photo. [Online]. Available: http://cds.cern.ch/record/841573

[13] R. Jones, “First years experience of LHC Beam Instrumentation,” in *Proceedings of 2nd International Particle Accelerator Conference (IPAC 11)*, Sep. 2011, pp. 3779–3783.

[14] E. Calvo Giraldo, J. L. Gonzalez, L. K. Jensen, O. R. Jones, T. Lefevre, J. J. Savioz, R. Steinhagen, and J. Wenninger, “The LHC Beam Position System: Performance during 2010 and Outlook for 2011,” in *Proceedings of 10th European Workshop on Beam Diagnostics and Instrumentation for Particle Accelerators (DIPAC 11)*, May 2011, pp. 323–325.

[15] B. Dehning, E. Effinger, J. Emery, G. Ferioli, G. Guaglio, E. B. Holzer, D. Kramer, L. Ponce, V. Prieto, M. Stockner, and C. Zamantzas, “The LHC Beam Loss Measurement System,” in *Proceedings of 22nd Particle Accelerator Conference (PAC 07)*, Jun. 2007, pp. 4192–4194.

[16] S. Bart Pedersen, A. Boccardi, E. Bravin, G. Burtin, S. Burger, B. Dehning, J. Emery, A. Fisher, A. Guerrero, A. Jeff, J. Koopman, T. Lefevre, A. Rabiller, and F. Roncarolo, “Profile monitors, injection matching monitor and synchrotron light monitor,” in *Proceedings of Workshop on LHC Commissioning (Evian 2010)*, Jan. 2010, pp. 67–70.

[17] P. Odier, D. Belohrad, J. J. Gras, and M. Ludwig, “Operational Experience and Improvements of the LHC Beam Current Transformers,” in *Proceedings of 10th European Workshop on Beam Diagnostics and Instrumentation for Particle Accelerators (DIPAC 11)*, May 2011, pp. 467–469.

[18] CERN. LHC sets world record beam intensity. Press release. [Online]. Available: https://home.cern/news/press-release/cern/lhc-sets-world-record-beam-intensity

[19] J.-C. Denard, “Beam current monitors,” in *CAS - CERN Accelerator School: Beam Instrumentation*, D. Brandt, Ed. CERN, Jun. 2008, pp. 141–155.

[20] G. Norton and J. Duggan, “Industrial Applications of Electro-static Accelerators,” in *Handbook of Accelerator Physics and Engineering 3rd Ed.*, A. W. Chao and M. Tigner, Eds. World Scientific, Mar. 1999, p. 30.

[21] K. Kershaw, J.-L. Grenard, M. Calviani, C. Ahdida, M. Casolino, S. Delavalle, D. Hounsome, R. Jacobsson, M. Lamont, E. L. Sola, R. Scott, V. Vlachoudis, and H. Vincke, “Design Development for the Beam Dump Facility Target Complex at CERN,” *Journal of Instrumentation*, vol. 13, no. 10, Oct. 2018.

[22] S. Papadopoulou, F. Antoniou, T. Argyropoulos, M. Fitterer, M. Hostettler, and Y. Papaphilippou, “Modelling and measurements of bunch profiles at the LHC,” in *Proceedings of 8th International Particle Accelerator Conference (IPAC 17)*, May 2017, pp. 2167–2170.

[23] H. Timko, P. Baudrenghien, J. Esteban Muller, and E. Shaposhnikova, “LHC MD 1279: Bunch Flattening in Physics,” CERN, Tech. Rep. CERN-ACC-NOTE-2017-0019, Mar. 2017.

[24] G. Papotti, T. Bohl, F. Follin, and U. Wehrle, “Longitudinal Beam measurements at the LHC: The LHC Beam Quality Monitor,” in *Proceedings of 2nd International Particle Accelerator Conference (IPAC 11)*, Sep. 2011, pp. 1852–1854.

[25] O. D. Jefimenko, “Direct calculation of the electric and magnetic fields of an electric point charge moving with constant velocity,” *American Journal of Physics*, vol. 62, no. 1, p. 79, Jan. 1994.

[26] A. Hofmann, “Dynamics of beam diagnostics,” in *CAS - CERN Accelerator School: Beam Instrumentation*, D. Brandt, Ed. CERN, Jun. 2008, pp. 66–67.

[27] C. J. Bouwkamp and N. G. De Bruijn, “The electrostatic field of a point charge inside a cylinder, in connection with wave guide theory,” *Journal of Applied Physics*, vol. 18, no. 6, pp. 562–577, Feb. 1947.

[28] R. E. Shafer, “Beam Position Monitoring,” in *AIP Conference Proceedings*, vol. 212, 1990, pp. 33–37.

[29] T. C. Hayes and P. Horowitz, *Learning the Art of Electronics: A Hands-On Lab Course*, 1st ed. Cambridge University Press, Mar. 2016.

[30] T. Bohl and J.-F. Malo, “The APWL Wideband Wall Current Monitor,” CERN, Tech. Rep. CERN-BE-2009-006, Feb. 2009.

[31] P. Odier, “DCCT Technology Review,” in *Proceedings of Workshop on DC Current Transformers and Beam-Lifetime Evaluations*, Dec. 2004, pp. 3–5.

[32] D. Belohrad, J. Bergoz, M. Krupa, P. Odier, L. Soby, and F. Stulle, “A New Integrating Current Transformer for the LHC,” in *Proceedings of 3rd International Beam Instrumentation Conference (IBIC 2014)*, Sep. 2014, pp. 540–543.

[33] B. Keil, R. Baldinger, R. Ditter, D. Engeler, W. Koprek, R. Kramert, A. Malatesta, F. Marcellini, G. Marinkovic, M. Roggli, M. Rohrer, and M. Stadler, “Status of The SwissFEL BPM System,” in *Proceedings of 4th International Beam Instrumentation Conference (IBIC 2015)*, Sep. 2015, pp. 497–501.

[34] M. Wendt, “BPM Systems: A brief Introduction to Beam Position Monitoring,” in *CAS - CERN Accelerator School: Course on Beam Instrumentation for Particle Accelerators*, H. Schmickler, Ed. CERN, Jun. 2020, pp. 340–342.

[35] O. S. Brüning, P. Collier, P. Lebrun, S. Myers, R. Ostojic, J. Poole, and P. Proudlock, *LHC Design Report*. Geneva: CERN, 2004, pp. 3–13.

[36] P. Odier, M. Ludwig, and S. Thoulet, “The DCCT for the LHC Beam Intensity Measurement,” in *Proceedings of 9th European Workshop on Beam Diagnostics and Instrumentation for Particle Accelerators (DIPAC 09)*, May 2009, pp. 143–145.

[37] D. Belohrad, L. Jensen, O. Jones, M. Ludwig, and J. Savioz, “The LHC Fast BCT System: A Comparison of Design Parameters with Initial Performance,” in *Proceedings of 14th Beam Instrumentation Workshop (BIW 10)*, May 2010, pp. 269–273.

[38] G. Böhner, A. Falvard, J. Lecoq, P. Perret, and C. Trouilleau, “Very front-end electronics for the LHCb preshower,” CERN, Geneva, Tech. Rep. LHCb-2000-047, CERN-LHCb-2000-047, Oct. 2000, pp. 8–10.

[39] D. Belohrad, O. R. Jones, M. Ludwig, J. J. Savioz, and S. Thoulet, “Implementation of the Electronics Chain for the Bunch by Bunch Intensity Measurement Devices for the LHC,” in *Proceedings of 9th European Workshop on Beam Diagnostics and Instrumentation for Particle Accelerators (DIPAC 09)*, May 2009, pp. 137–139.

[40] V. Balagura, "Overview of LHCb luminosity determination methodology in Run 2," in *Contributions to LHC Lumi Days 2019*, Jun. 2019, p. 12.

[41] D. Belohrad, D. Esperante Pereira, J. Kral, and S. Pedersen, "Upgrade of the LHC Bunch by Bunch Intensity Measurement Acquisition System," in *Proceedings of 5th International Beam Instrumentation Conference (IBIC 2016)*, Sep. 2016, pp. 135–138.

[42] C. Ohm and T. Pauly, "The ATLAS beam pick-up based timing system," *Nucl. Instrum. Methods Phys. Res., A*, vol. 623, pp. 558–560, May 2009.

[43] A. Jeff, M. Andersen, A. Boccardi, S. Bozyigit, E. Bravin, T. Lefevre, A. Rabiller, F. Roncarolo, C. P. Welsch, and A. S. Fisher, "Longitudinal density monitor for the LHC," *Phys. Rev. ST Accel. Beams*, vol. 15, p. 032803, Mar. 2012.

[44] C. Barschel, M. Ferro-Luzzi, J.-J. Gras, M. Ludwig, P. Odier, and S. Thoulet, "Results of the LHC DCCT Calibration Studies," CERN, Geneva, Tech. Rep. CERN-ATS-Note-2012-026 PERF, Feb. 2012, p. 9.

[45] C. Fischer and R. Schmidt, "On the Measurements of the Beam Current, Lifetime and Decay Rate in the LHC Rings," CERN, Geneva, Tech. Rep. LHC-BCT-ES-0001, Jan. 2005, p. 7.

[46] G. Anders, N. Bacchetta, V. Balagura, C. Barschel, D. Belohrad, H. Burkhardt, M. Ferro-Luzzi, C. Gabaldon, M. Gagliardi, J. J. Gras, P. Hopchev, A. Jeff, W. Kozanecki, M. Ludwig, D. Marlow, K. Oyama, J. Panman, S. White, and A. Zuranski, "Study of the relative LHC bunch populations for luminosity calibartion," CERN, Tech. Rep. CERN-ATS-NOTE-2012-028, Feb. 2012, p. 5.

[47] J. J. Gras, D. Belohrad, M. Ludwig, P. Odier, and C. Barschel, "Optimization of the LHC beam current transformers for accurate luminosity determination," in *Proceedings of 2nd International Particle Accelerator Conference (IPAC 2011)*, Sep. 2011, pp. 1395–1397.

[48] K. Satoh, "New Wall Current Beam Position Monitor," in *Proceedings of 8th Particle Accelerator Conference (PAC 79)*, Jun. 1979, pp. 3364–3366.

[49] V. Cherepanov, "Image Current Monitor for Bunched Beam Parameters Measurements," in *Proceedings of 2nd European Workshop on Beam Diagnostics and Instrumentation for Particle Accelerators (DIPAC 95)*, May 1995, pp. 142–144.

[50] M. Gasior, "An Inductive Pick-Up for Beam Position and Current Measurements," in *Proceedings of 6th European Workshop on Beam Diagnostics and Instrumentation for Particle Accelerators (DIPAC 03)*, May 2003, pp. 53–55.

[51] P. Horowitz and W. Hill, *The Art of Electronics*, 3rd ed. Cambridge University Press, Mar. 2015.

[52] J. Hagen, *Radio-Frequency Electronics: Circuits and Applications*. Cambridge University Press, 2009, p. 103.

[53] W. Hurley and W. Wolfle, *Transformers and Inductors for Power Electronics: Theory, Design and Applications*. John Wiley & Sons, Apr. 2013, p. 63.

[54] R. Schaumann and M. E. Van Valkenburg, *Design of Analog Filters*. Oxford University Press, 2001, p. 72.

[55] Texas Instruments, Inc. THS3201 1.8-GHz, Low Distortion, Current-Feedback Amplifier. Datasheet. [Online]. Available: https://www.ti.com/lit/ds/symlink/ths3201.pdf

[56] Ceramic Magnetics, Inc. CMD5005 General Purpose, High Frequency Ni-Zn Ferrite. Datasheet. [Online]. Available: https://www.magneticsgroup.com/wp-content/uploads/2019/09/CMD5005-ISO-WEB-DATA.pdf

[57] VACUUMSCHMELZE GmbH & Co. KG. Specification for Soft Magnetic Cores. T60006-L2009-W914-03. Datasheet. [Online]. Available: https://vacuumschmelze.de/Assets-Web/914-03-(1).pdf

[58] M. Krupa. WCT Internal PCB. PCB layout. [Online]. Available: https://edms.cern.ch/item/EDA-03030-V2-0/0

[59] E. Rosa, *The Self and Mutual Inductances of Linear Conductors*, ser. Bulletin of the Bureau of Standards. U.S. Department of Commerce and Labor, Bureau of Standards, 1908, no. 80, pp. 302-305.

[60] A. Demougeot. New WCT for the LHC. Technical drawings. [Online]. Available: https://edms.cern.ch/document/1391735/1

[61] M. A. Morgan and T. A. Boyd, “Synthesis of a new class of reflectionless filter prototypes,” 2010, arXiv:1008.3502.

[62] M. Krupa. LHC BCTW Head Amplifier. PCB layout. [Online]. Available: https://edms.cern.ch/item/AED-00233/0

[63] ——. LHC BCTW Distribution Amplifier. PCB layout. [Online]. Available: https://edms.cern.ch/item/AED-00236/0

[64] VACUUMSCHMELZE GmbH & Co. KG. Specification for Soft Magnetic Cores. T60006-L2063-W517-02. Datasheet. [Online]. Available: https://vacuumschmelze.com/Assets-Web/517-02-(1).pdf

[65] EPCOS AG, TDK Group Company. Ferrites and accessories. Datasheet. [Online]. Available: https://www.tdk-electronics.tdk.com/inf/80/db/fer/r_58_3_40_8_17_6.pdf

[66] Acrotecna. LHC Beam Current Transformer - DCCT and FBCT Chamber Assembly. Technical Drawing. [Online]. Available: https://edms.cern.ch/document/687858/0

[67] C. Menot. LHC Beam Current Transformer - Antenne de Calibration Plan d’Ensemble. Technical Drawing. [Online]. Available: https://edms.cern.ch/document/693605/0

[68] M. Krupa and M. Gasior, "Application of Avalanche Generators in Laboratory Measurements," in *Proceedings of 21st International Conference Mixed Design of Integrated Circuits and Systems (MIXDES 2014)*, Jun. 2014, pp. 529–532.

[69] P. J. Pupalaikis. Random Interleaved Sampling (RIS). Whitepaper. [Online]. Available: http://cdn.teledynelecroy.com/files/whitepapers/wp_ris_102203.pdf

[70] M. Krupa and M. Gasior, "Precise Digital Integration of Fast Analogue Signals using a 12-bit Oscilloscope," in *Proceedings of 3rd International Beam Instrumentation Conference (IBIC 2014)*, Sep. 2014, pp. 584–586.

[71] D. C. Lay, *Linear algebra and its applications*, 5th ed. Pearson, Jan. 2015, p. 73.

[72] F. Caspers, "RF Engineering Basic Concepts: S-parameters," in *CAS - CERN Accelerator School: RF for Accelerators*, R. Bailey, Ed. CERN, Nov. 2011, pp. 67–94.

[73] G. Rumolo, "Beam Instabilities," in *CAS - CERN Accelerator School: Advanced Accelerator Physics Course*, W. Herr, Ed. CERN, Dec. 2014, p. 202.

[74] F. Caspers, "Impedance Determination from Bench Measurements," in *Handbook of Accelerator Physics and Engineering 3rd Ed.*, A. W. Chao and M. Tigner, Eds. World Scientific, Mar. 1999, pp. 622–626.

[75] M. Krupa, D. Belohrad, M. Gasior, T. Lefevre, and L. Soby, "Summary of LHC MD 398: Verification of the dependence of the BCTF measurements on beam position and bunch length," CERN, Tech. Rep. CERN-ACC-NOTE-2015-0031, Sep. 2015.

[76] Y. Papaphilippou, H. Bartosik, G. Rumolo, and D. Manglunki, "Operational Beams for the LHC," in *Proceedings of Chamonix 2014 Workshop on LHC Performance*, Dec. 2014, p. 82.

[77] M. Solfaroli Camillocci, S. Redaelli, R. Tomás, and J. Wenninger, "Combined Ramp and Squeeze to 6.5 TeV in the LHC," in *Proceedings of 7th International Particle Accelerator Conference (IPAC 2016)*, May 2016, pp. 1509–1512.

[78] R. J. Steinhagen, "Feedbacks on Tune and Chromaticity," in *Proceedings of 8th European Workshop on Beam Diagnostics and Instrumentation for Particle Accelerators (DIPAC 07)*, 2007, p. 43.

[79] C. Bocchetta, "Review of Orbit Control," in *Proceedings of 6th European Particle Accelerator Conference (EPAC 98)*, Jun. 1998, pp. 28–32.

[80] G. Trad, "Development and Optimisation of the SPS and LHC beam diagnostics based on Synchrotron Radiation monitors," Ph.D. dissertation, University of Grenoble, France, Oct. 2014, pp. 118–120, presented 22 Jan 2015.

[81] M. Krupa and M. Gasior, "A Precise Pulsed Current Source for Absolute Calibration of Current Measurement Systems With No DC Response," in *Proceedings of 5th International Beam Instrumentation Conference (IBIC 2016)*, Sep. 2016, pp. 165–168.